Evolution of solar wind electrons in the inner heliosphere

Joel Baby Abraham

A dissertation submitted in partial fulfillment

of the requirements for the degree of

Doctor of Philosophy

of

University College London.

Department of Space and Climate Physics

University College London

December 17, 2023

I, Joel Baby Abraham, confirm that the work presented in this thesis is my own. Where information has been derived from other sources, I confirm that this has been indicated in the work.

Abstract

In the first study, we develop and apply a novel and bespoke fitting routine to a large volume of solar wind electron distribution data collected by Parker Solar Probe (PSP) over its first five orbits, covering radial distances from 0.13 to 0.5 au. We use this database to characterize the radial evolution of the electron core, halo and strahl populations in the slow solar wind during these orbits. For the first time, we provide evidence for the growth of the combined suprathermal halo and strahl populations over the heliospheric distance range from 0.13 to 0.2 au. We find that in the inner heliosphere the formation of the halo is not solely due to the transfer of strahl electrons into the halo, which has also been previously suggested as a source mechanism for the halo at greater heliospheric distances. We find that the strahl preserves the thermal signature of the coronal origins. We discover the *halo strahl cross over* point. In the second study of this thesis, we develop for the first time a framework which is based on the second moment of the Boltzmann equation to evaluate the complete electron thermal energy budget. In this study, we find that there is an irreversible thermal energy source for electrons in the inner heliosphere, but the magnitude of the thermal energy source decreases with radial distance. The divergence of heat flux changes sign from positive to negative at 0.33 au. This finding indicates that there is a fundamental change in processes that define the shape of the electron distribution function at around 0.33 au. In this third study, we undertake a case study to examine the structure of the deficit signature which arises due to the ambipolar electric potential field and find that the signature is heavily processes. We find whistler driven instability is insufficient to erase the deficit signature.

Impact Statement

The work on solar wind electrons presented in this thesis will provide benefits to both inside and outside of academia. With regard to academic impact, each of the three studies addressed in this document makes a critical contribution to answering a key open question in heliosphysics: What drives the outflow of the solar wind from the Sun? The work presented in this thesis has achieved notable recognition, locally at UCL/MSSL winning the Alan Johnstone award and internationally an Asian Golden Shawl Award for outstanding scientific contribution to the field of heliosphysics by a research student. The work presented in this thesis has to date produced two publications in an academic journal, contributing significantly to the body of knowledge in the field.

For example, the framework developed in Chapter 5 addresses for the first time the thermal energy budget of the solar wind from in situ observations. This framework is a vital contribution to understanding the thermodynamic balance of the solar wind outflow and benefits a large group of researchers who can apply this framework to other solar wind particle populations. Further academic impact stems from the development, in Chapter 6, of a model that provides critical insight into the structure of the electrostatic potential around the Sun. This is also a key ingredient in understanding the acceleration mechanisms that drive the solar wind.

The research on solar wind electrons in this thesis is relevant to the understanding of the science behind space weather and has relevance for future space exploration. Space weather is a phenomenon that impacts technological infrastructure and systems both on Earth and in orbit due to variations on the Sun transmitted via the solar wind. Space weather is listed on the UK government's National

Risk Register (NRR) (https://www.gov.uk/government/publications/national-risk-register-2020). According to a recent economic impact assessment, a Carrington-level space weather event could risk an annual economic loss of a trillion pounds. The solar wind is the primary driver in influencing space weather. Understanding the evolution of the solar wind, which is the main objective of this thesis, is crucial in developing forecasting tools and strategies to mitigate the impacts of space weather on our technological infrastructure. This will enable more reliable and resilient satellite communications, GPS systems, spacecraft navigation and power grids to the effects of space weather.

Finally, 99.9 % of the visible universe is in the plasma state, but is inaccessible to in-situ study. This makes the solar wind an ideal natural source to study the most abundant material in the visible universe. It is hoped that the research presented in this document will foster a sense of wonder and curiosity about our universe, inspire future generations of scientists and engineers to push the boundaries of knowledge, and will drive transformative breakthroughs in both academic and non-academic fields.

UCL Research Paper Declaration Form: Referencing the doctoral candidate's own published work(s)

1. **1. For a research manuscript that has already been published** (if not yet published, please skip to section 2)**:**

   (a) **What is the title of the manuscript?** Radial evolution of thermal and suprathermal electron populations in the slow solar wind from 0.13 to 0.5 au : Parker Solar Probe Observations

   (b) **Please include a link to or doi for the work:** DOI 10.3847/1538-4357/ac6605

   (c) **Where was the work published?** The Astrophysical Journal

   (d) **Who published the work?** American Astronomical Society

   (e) **When was the work published?** 1st June 2022

   (f) **List the manuscript's authors in the order they appear on the publication:** Joel B. Abraham; Christopher J. Owen; Daniel Verscharen; Mayur Bakrania; David Stansby; Robert T. Wicks; Georgios Nicolaou; Phyllis L.Whittlesey; Jefferson A.Agudelo Rueda and Seong-Yeop Jeong

   (g) **Was the work peer reviewd?** Yes

   (h) **Have you retained the copyright?** Yes

   (i) **Was an earlier form of the manuscript uploaded to a preprint**

server (e.g. medRxiv)? If 'Yes', please give a link or doi https://arxiv.org/abs/2204.05001

If 'No', please seek permission from the relevant publisher and check the box next to the below statement:

☒ *I acknowledge permission of the publisher named under 1d to include in this thesis portions of the publication named as included in 1c.*

2. **For a research manuscript prepared for publication but that has not yet been published** (if already published, please skip to section 3)**:**

   (a) **What is the current title of the manuscript?**

   (b) **Has the manuscript been uploaded to a preprint server 'e.g. medRxiv'?**

   If 'Yes', please please give a link or doi:

   (c) **Where is the work intended to be published?**

   (d) **List the manuscript's authors in the intended authorship order:**

   (e) **Stage of publication:**

3. **For multi-authored work, please give a statement of contribution covering all authors** (if single-author, please skip to section 4)**:** Joel B. Abraham developed the fitting routine, led the analysis and performed the bulk of the work and prepared the article. Mayur Bakrania provided tools which were used for the machine learning part. David Stansby provided data related to the solar wind speed. Phyllis L. Whittlesey is the representative of the prime instrument team and specifically provided key information to establish erros related to the uncertainty in the geometric factor. Christopher J. Owen and Daniel Verscharen, provided the motivation for the project and contributed through scientific advice and discussion, together with significant reviews during the writing of the manuscript. Robert T. Wicks, Georgios Nicolaou, Jefferson A. Agudelo Rueda and Seong-Yeop Jeong contributed through scientific advice and discussion.

4. **In which chapter(s) of your thesis can this material be found?** Chapter 4

e-Signatures confirming that the information above is accurate (this form should be co-signed by the supervisor/ senior author unless this is not appropriate, e.g. if the paper was a single-author work)**:**

Candidate:

Joel Baby Abraham

Date:

3rd August 2023

Supervisor/Senior Author signature (where appropriate)**:**

Professor Christopher J Owen

Date:

3rd August 2023

UCL Research Paper Declaration Form: Referencing the doctoral candidate's own published work(s)

1. **1. For a research manuscript that has already been published** (if not yet published, please skip to section 2)**:**

   (a) **What is the title of the manuscript?** Thermal Energy Budget of Electrons in the Inner Heliosphere: Parker Solar Probe Observations

   (b) **Please include a link to or doi for the work:** DOI 10.3847/1538-4357/ac9fd8

   (c) **Where was the work published?** The Astrophysical Journal

   (d) **Who published the work?** American Astronomical Society

   (e) **When was the work published?** 19^{th} December 2022

   (f) **List the manuscript's authors in the order they appear on the publication:** Joel B. Abraham; Daniel Verscharen; Robert T. Wicks; Jefferson A. Agudelo Rueda; Christopher J. Owen; Georgios Nicolaou and Seong-Yeop Jeong

   (g) **Was the work peer reviewd?** Yes

   (h) **Have you retained the copyright?** Yes

   (i) **Was an earlier form of the manuscript uploaded to a preprint server (e.g. medRxiv)? If 'Yes', please give a link or doi** https://arxiv.org/abs/2211.02186

If 'No', please seek permission from the relevant publisher and check the box next to the below statement:

☒ *I acknowledge permission of the publisher named under 1d to include in this thesis portions of the publication named as included in 1c.*

2. **For a research manuscript prepared for publication but that has not yet been published** (if already published, please skip to section 3)**:**

   (a) **What is the current title of the manuscript?**

   (b) **Has the manuscript been uploaded to a preprint server 'e.g. medRxiv'?**
   If 'Yes', please please give a link or doi:

   (c) **Where is the work intended to be published?**

   (d) **List the manuscript's authors in the intended authorship order:**

   (e) **Stage of publication:**

3. **For multi-authored work, please give a statement of contribution covering all authors** (if single-author, please skip to section 4)**:** Joel B. Abraham developed the framework for the application of the thermal energy budget, led the analysis and performed the bulk of the work, including the polytropic index analysis, and prepared the article. Jefferson A. Agudelo Rueda, Daniel Verscharen and Seong-Yeop Jeong contributed through theoretical support which developed the analysis of the second moment of the Boltzmann equation. Christopher J. Owen; Robert T. Wicks; Georgios Nicolaou contributed through scientific advice and discussion, together with significant reviews during the writing of the manuscript.

4. **In which chapter(s) of your thesis can this material be found?** Chapter 5

e-Signatures confirming that the information above is accurate (this form should be co-signed by the supervisor/ senior author unless this is not appropriate, e.g. if the paper was a single-author work)**:**

Candidate:

Joel Baby Abraham

Date:

3rd August 2023

Supervisor/Senior Author signature (where appropriate)**:**

Professor Christopher J Owen

Date:

3rd August 2023

Acknowledgements

First and foremost, I want to express my sincere gratitude and appreciation to my supervisors, Prof. Christopher Owen and Dr. Daniel Verscahren, for their excellent guidance, insight, and support throughout my PhD journey. I consider myself fortunate to have two supervisors whose willingness to invest their time and expertise in helping me navigate this transition from engineering to science has made a remarkable difference in my professional growth and development as a scientist. I am grateful for their understanding and encouragement, as they have consistently shown belief in my abilities, even at times when I have doubted myself, and provided me with the necessary tools and resources to succeed in the science field. Chris and Daniel, your mentorship has not only enhanced my knowledge and skills but has also instilled in me a sense of confidence and enthusiasm for my chosen path.

I would like to give special thanks to Dr. Phyllis Whittlesey for the countless hours you have spent answering my questions, providing clarifications about SWEAP. Your dedication to ensuring my understanding and your commitment to my learning journey have been truly remarkable. I would like to sincerely thank Dr. Georgios Nicolaou for many in-depth scientific discussion about instrumentation that span well into the early mornings. Georgios, this has not only expanded my knowledge about instruments but has also instilled in me a deep fascination and appreciation for the world of spacecraft instrumentation. Your passion for the subject is infectious, and it has inspired me to explore further and delve deeper into this fascinating field.

I felt extremely privileged and honoured to have led the Joint Electron Project

team. I owe a debt of gratitude to all the members of the Joint Electron Project group: Prof. Rob Wicks, Dr. Jefferson A. Agudelo Rueda, Dr. Seong-Yeop Jeong, Dr. David Stansby, Dr. Jesse Coburn, Dr. Mayur Bakrania and Dr. Laura Bercic. I am immensely grateful for the unwavering support, countless scientific discussion and guidance you have provided me throughout my journey. Today, I stand proud of my accomplishments, and I owe a great deal of it to the members in this group.

I am very grateful to all the members of the Space Plasma and Planetary groups. Dr. Will Dunn thank you for the support, encouraging feedback and inspirational talks. I am very grateful to the Solar Orbiter mission operations team. Dr. Gethyn Lewis, Dr. Chandrasekhar Anekallu and Dr. Gill Watson, thank you for showing me around the operations side of the Solar Orbiter mission and how calibrations and in-flight testing is done.

I am thankful for all my office colleagues: Dr. Deborah Baker and Dr. Alex James for inspiring discussion and office chats keeping my sanity in check. I want to thank Duncan Rust for providing me a refuge during the pandemic period. I also owe a debt of gratitude to many staff members and students at MSSL. I am thankful to all the PhD students, who were all inspiring in their own ways: Sachin Reddy, Gabriel Suen, Camille Lorfing, Jinge Zhang, Abid Razvani Christian Lao, Charalambos Ioannou, Ahlam Alqasim, Samuel Grant, Sam Walton and Caoimhe Doherty. Thank you, Firat Toguz for being a great friend and being there during the highs and lows of my PhD. Thanks to Phillipa Elwell and Prof. Daisuke Kawata for all your pastoral help and support. Thank you to Sam Babister for sorting out my flights and travel for conferences, especially when there were last minute flight and train cancellations. Special thanks to my parents and sister for supporting and believing in me during my PhD from start to finish, especially during the past year, keeping me afloat during some turbulent times. Dad, thanks for believing in me. Mum, thank you for always making sure I ate something, even when I forgot to eat. Dad and Mum, thank you for inspiring me to face life's twist and turns with a smile. Sister, thank you for being the best sibling and checking up on my well-being. Finally, I would also like to thank the Science and Technology Facilities

Council for sponsoring my research.

Contents

List of Figures

Chapter 1

Introduction

1.1 Motivation

It is believed that 99.9% of all the matter in the visible universe is composed of plasma in the form of stars, stellar winds, accretion disks around black holes to galaxy clusters and clouds within supernovae remnants (Cowie and McKee, 1977; Bertschinger and Meiksin, 1986; Baumjohann and Treumann, 2012). Most astrophysical plasmas are too distant and unreachable to make any in-situ measurements to understand their fundamental properties. Conversely, the solar wind is the perfect medium to study in order to understand the nature and characteristics of space plasma. The solar wind was discovered at the dawn of the space age (Gringauz and Rytov, 1961), but the physics behind coronal and solar-wind heating, as well as the acceleration of the solar wind, remain long-standing and key unresolved issues in solar and stellar physics (Marsch, 2006; Feldman et al., 1979). In-situ measurements of the solar wind provide insight into the underlying heating and acceleration mechanisms (Feldman et al., 1975, 1976, 1979; Marsch, 2006). It is well understood that the electrons, due to their small mass and high speeds, facilitate global heat conduction, while ions facilitate momentum transport (Feldman et al., 1975; Marsch, 2006). The solar wind is composed of many particle populations with different temperatures, anisotropies, relative drifts, heat fluxes and formations, such as beam-like structures (Feldman et al., 1975, 1979; Marsch, 2006; Maksimovic et al., 2005; Štverák et al., 2009). The nature and evolution of the electron velocity

distribution function (eVDF) provide important information that can help us to understand the mechanism of solar wind acceleration and heat conduction (Feldman et al., 1975; Lemaire and Scherer, 1971). The launches of Parker Solar Probe (PSP) (Fox et al., 2016) and Solar Orbiter (SO) (Müller et al., 2020) in 2018 and 2020, respectively, provide unprecedented high-resolution measurements of the pristine solar wind near the Sun and in the inner heliosphere. These new data sets give us a unique opportunity to bridge the gap between local and global kinetic processes (Feldman et al., 1975; Marsch, 2006; Müller et al., 2020; Verscharen et al., 2019).

The research presented in this thesis aims to understand the kinetic properties of the solar wind electron populations in the inner heliosphere. In this Chapter, we introduce the necessary information that is needed to understand the original work presented in this thesis in Chapters 4, 5 and 6 respectively.

1.2 Plasma

Plasma is the fourth state of matter and is defined as a collection of ions and electrons that exhibit both quasi-neutrality and collective behaviour on a global scale. A quasi-neutral gas has approximately equal number of positive (ions) and negative (electrons) charges on scales much larger than the collective interaction scale, such that the plasma has a net-zero charge density on those scales (Kivelson and Russell, 1995). Collective behaviour is a phenomenon where the motion of the plasma does not depend on single charged particle, but depends on each charged particle interacting simultaneously with many other charged particles. This can be illustrated by considering the electric potential around an assumed point charge in a vacuum, which is defined as:

$$\phi_T(r) = \frac{q_T}{4\pi\varepsilon_0 r}, \tag{1.1}$$

where ϕ_T is the potential around the point charge, q_T is the point charge, ε_0 is the permittivity of free space and r is the distance from the point charge. If the test point charge is surrounded by many other charged particles, they act to shield the electric potential of the point charge. This is called Debye shielding (Kivelson and

Russell, 1995). The shielded potential takes the form:

$$\phi_T(r) = \frac{q_T}{4\pi\varepsilon_0 r} e^{\left(\frac{-r}{\lambda_D}\right)} \tag{1.2}$$

where λ_D is the Debye length, also known as the spatial charge separation scale length. It can be noted from Equations (1.1) and (1.2) that for small distances from the test particle, the potential is almost the same as the Coulomb potential. However, further away from the test particle, the potential in Equation (1.2) falls more rapidly with distance compared to the Coulomb potential shown in Equation (1.1). This means that charged particles within a few Debye lengths are not strongly influenced by the Coulomb potential of the point charge, as particles within a Debye length move closer to electrically screen the point charge. This collective interaction scale in an electron-ion gas is given by:

$$\lambda_D = \sqrt{\left(\frac{\varepsilon_0 k_B T_e}{n_e q^2}\right)^2 + \left(\frac{\varepsilon_0 k_B T_i}{n_i Z_i^2 q_i^2}\right)^2} \tag{1.3}$$

where T_e is the electron temperature, T_i is the ion temperature, n_e is the density of electrons, n_i is the density of ions, Z_i is the charge state of the ions and k_B is the Boltzmann constant. The ions are at least 1836 times heavier than the electrons, so the ions have a greater inertia (Kivelson and Russell, 1995). This means the response of ions to the test particle is slow and limited compared to the electrons, which are more mobile. Therefore, it is normal practice to consider the ions as immobile and ignore their contribution to shielding. With this consideration, the Debye length is given by:

$$\lambda_D = \sqrt{\frac{\varepsilon_0 k_B T_e}{n_e q^2}} \tag{1.4}$$

For a plasma to be considered quasi-neutral, the characteristic spatial scale of the system, L, must be much larger than the typical spatial charge separation scale in the plasma (Kivelson and Russell, 1995). This criterion needs to be fulfilled for an ionised medium to behave as a plasma. Moreover, for Debye shielding to work,

there must be enough particles within the charge cloud to neutralise the polarisation effects of point charges. This leads to the second criterion that needs to be fulfilled for an ionised medium to be a plasma: There should be many particles inside the Debye sphere (a sphere with a radius of 1 Debye length), a condition that can be captured mathematically as follows:

$$\frac{4\pi}{3} n_e \lambda_D^3 \gg 1 \tag{1.5}$$

where n_e is the number density of electrons. If a plasma is in charge equilibrium and a perturbation is applied to a group of electrons, with respect to the ions, the Coulomb force act on the electrons to correct for the disturbance in the charge density. This restoring force induces an oscillation. There is thus a natural frequency of plasma oscillations due to charge density perturbations, which is known as the plasma frequency :

$$\omega_p = \sqrt{\frac{n_e q^2}{m_e \varepsilon_0}} \tag{1.6}$$

where m_e is the electron mass. Some plasmas are not fully ionised, for example those forming the terrestrial ionosphere, where there are significant numbers of neutral particles. To maintain the collective behaviour, the plasma must be dominated by electrostatic forces, which means it can only experience infrequent collisions. In a proton-electron plasma, the electrons are the most mobile and ions are static in comparison due to their mass difference. For the electrons to remain unaffected, on a global scale, by collisions with neutrals, they need to fulfil a third criterion. This states that the average time for an electron-neutral collision must be large compared to the reciprocal of the plasma frequency, or alternately:

$$\omega_p \tau_n \gg 1 \tag{1.7}$$

where τ_n is the average time between collisions of an electron with a neutral particle.

1.2.1 Single particle motion

Since plasma is mainly composed of charged particles, the roles of electric and magnetic fields are important in influencing the behaviour of these particles, and therefore the plasma. We can readily solve the equations of motion for a single particle under the influence of electromagnetic fields. If a particle with a charge, q_e, moves with a velocity, $\mathbf{v}$, and encounters an electric field, $\mathbf{E}$, and a magnetic field, $\mathbf{B}$, then the particle experiences a force, the Lorentz Force ($\mathbf{F}_L$). This relationship can be expressed as the following equation of motion:

$$\mathbf{F}_L = q_e(\mathbf{E} + \mathbf{v} \times \mathbf{B}) \tag{1.8}$$

1.2.1.1 Charged particle motion in a constant magnetic field

Let us consider a case where a charged particle is exposed to a uniform magnetic field with no electric field applied. We assume that the magnetic field points along the z axis and neglect relativistic effects, so the equation of motion is as follows:

$$m\frac{d\mathbf{v}}{dt} = q_e(\mathbf{v} \times \mathbf{B}) \tag{1.9}$$

From Equation (1.9), the cross product shows that there is a force acting perpendicular to both the particle's velocity and the magnetic field. This means, in the presence of a uniform magnetic field, the particle has a circular motion in the plane perpendicular to the magnetic field, i.e., in the x-y plane. Taking the second derivative of Equation (1.9) and splitting it into each component gives:

$$\begin{aligned} \frac{d^2v_x}{dt^2} &= -\left(\frac{q_eB}{m}\right)^2 v_x \\ \frac{d^2v_y}{dt^2} &= -\left(\frac{q_eB}{m}\right)^2 v_y \\ \frac{d^2v_z}{dt^2} &= 0 \end{aligned} \tag{1.10}$$

From Equation (1.10), we can notice that the circular motion around the magnetic field gyrate with frequency, ω_g, also known as gyrofrequency:

$$\omega_g = \frac{q_e B}{m} \tag{1.11}$$

The gyration of the particle with respect to the magnetic field is dependent on the charge of the particle and the strength of the magnetic field. The positively charged particle gyrates in the clockwise direction, whereas the electron gyrates in the anticlockwise direction with respect to the magnetic field. The stronger the magnetic field, the larger the gyrofrequency. Integrating Equation (1.9) we can obtain the spatial motion of the particle in the x, y and z direction as follows:

$$\begin{aligned} x - x_0 &= \frac{V_\perp}{\omega_g} sin(\omega_g t); \\ y - y_0 &= \frac{V_\perp}{\omega_g} cos(\omega_g t); \\ z - z_0 &= V_{z_0} t; \end{aligned} \tag{1.12}$$

where $V_\perp$ is the perpendicular velocity ($V_\perp^2 = V_x^2 + V_y^2$), V_{z_0} is the initial parallel velocity, $V_{||}$; x, y, z are spatial coordinates and x_0, y_0, z_0 are constants of integration. The particle gyrates around the magnetic field with a gyrofrequency ω_g with a radius, known as Larmor radius, R_L, defined as :

$$R_L = \frac{V_\perp}{\omega_g} \tag{1.13}$$

As mentioned above, the electron mass is 1896 times smaller than that of the protons, and therefore from Equation (1.11) and (1.13), the electrons have a smaller Larmor radius. Examining Equations (1.12), it can be seen that, in addition to the circular motion, if the particle moves with a constant velocity along the z axis it produces an overall helical particle orbit. Figure 1.1 schematically represents the helical orbit in the x-z plane. Since in a uniform field the particle gyrates perpendicular to **B**, the centre of the gyrating motion is called the guiding centre at (x_0,y_0)

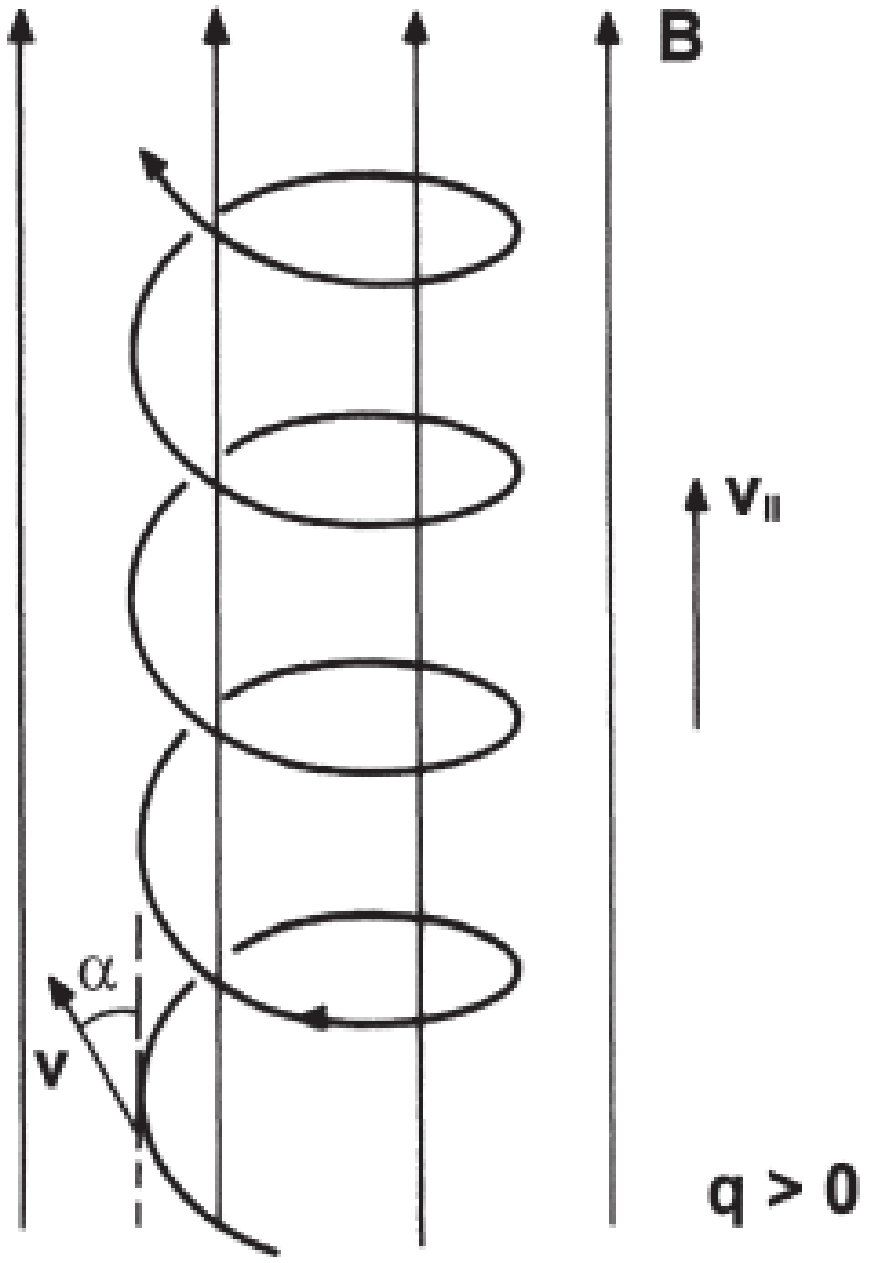

Figure 1.1: A schematic representation of the helical orbit of a positive charged particle along a uniform magnetic field, **B**. This Figure is taken from Bittencourt (2004).

and follows the magnetic field lines for a non-zero V_{z0}. The guiding centre motion is an approximation to visualise the large scale motion of the particle in a magnetic field.

Taking the dot product of velocity with Equation (1.9) we obtain the following energy equation:

$$\frac{d}{dt}\left(\frac{m\mathbf{v}^2}{2}\right) = 0 \tag{1.14}$$

Equation (1.14) tells us that the kinetic energy does not change, thus no work is done. This is only valid for a constant **B**. If **B** is time-dependent, then according to Maxwell's laws, an electric field is present that can do work on the particle and thus change its kinetic energy.

We note here that the angle formed between the particle resultant velocity vector and the magnetic field is defined as the pitch angle:

$$\alpha = \tan^{-1}\frac{V_\perp}{V_{||}} \tag{1.15}$$

A particle with a pitch angle 0° or 180° moves purely along or opposite to the magnetic field direction, i.e. $V_\perp = 0$. A particle with a pitch angle of 90° travels purely perpendicular to the magnetic field direction, i.e. $V_{||} = 0$, so this means that the particle gyrates purely around the field line with no motion in the field-parallel direction. The particle travels in a helical motion along the magnetic field line if the pitch angle is between 0° and 90° or 90° and 180°.

1.2.1.2 Charged particle motion in a constant electric field

We now consider two limiting cases, which include an electric field. The first case examines the particle's motion in the presence of a parallel electric field, $E_{||}$, where $E_{||}$ is along the magnetic field. The second case examines the particle's motion in the presence of a perpendicular electric field, $E_\perp$, where $E_\perp$ is perpendicular to the magnetic field. We treat each case separately. Considering the first case, we apply Equation (1.8) along the parallel direction, i.e, along the magnetic field direction, we obtain the following equation of motion:

$$m\frac{dV_{||}}{dt} = qE_{||} \tag{1.16}$$

This equation represents a motion with constant acceleration $\frac{qE_{||}}{m}$ along the B field direction. Integrating Equation (1.16) with respect to time, we obtain:

$$V_{||}(t) = \frac{qE_{||}t}{m} + V_{||_0} \tag{1.17}$$

where $V_{||_0}$ is the initial parallel velocity of the particle. From Equation (1.17) it can be seen that the particle is accelerated along the field by the parallel electric field. This equation is dependent on the charge, therefore ions and electrons are accelerated in opposite directions causing charge separation electric field in opposite direction to applied electric field. So, in most circumstances, we expect zero parallel electric field along field lines. As the ions are much heavier, they experience less acceleration than the electrons. In the relativistic case, the parallel acceleration of the particle is limited by relativistic effects.

Considering the second case of perpendicular electric field and applying Equation (1.8) along the perpendicular direction to the magnetic field, the following is obtained:

$$m\frac{dV_\perp}{dt} = q(E_\perp + \mathbf{V}_\perp \times \mathbf{B}) \tag{1.18}$$

We can make an ansatz such that $\mathbf{V}_\perp = \mathbf{V}'_\perp + \mathbf{V}_E$ where $\mathbf{V}'_\perp$ is the gyro motion that arises in the presence of $\mathbf{B}$ only, discussed above, and $\mathbf{V}_E$ is a constant velocity which is used to capture any extra motion that may arise due to the presence of the electric field. Substituting this ansatz into Equation (1.18) we obtain:

$$m\frac{dV_\perp}{dt} = q(E_\perp + \left(\mathbf{V}'_\perp + \mathbf{V}_E\right) \times \mathbf{B}) \tag{1.19}$$

If we remove components representing the gyro motion term derived above, we are left with $E_\perp + \mathbf{V}_E \times \mathbf{B} = 0$. Solving this equation for, $\mathbf{V}_E$ we obtain:

$$\mathbf{V}_E = \frac{\mathbf{E}_\perp \times \mathbf{B}}{B^2} \tag{1.20}$$

This is commonly referred to as the 'E cross B' drift velocity. In addition to the gyrating motion perpendicular to the magnetic field line, the particles guiding centre also drift in a direction that is perpendicular to both $\mathbf{E}$ and $\mathbf{B}$. The E cross B drift velocity is not dependent on the mass or charge of the particle, unlike in the case of

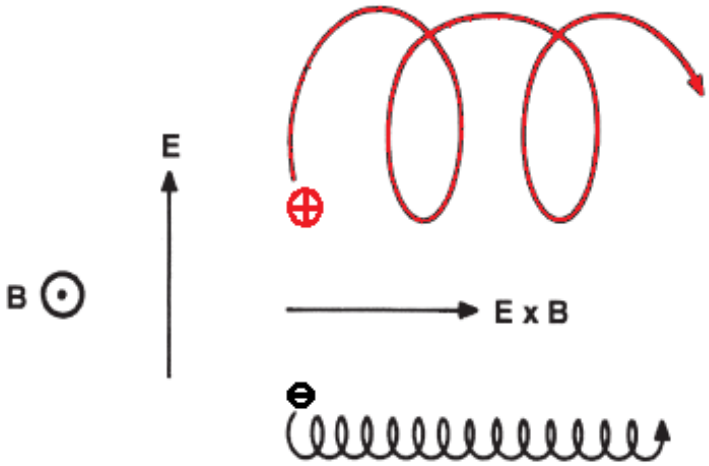

Figure 1.2: A schematic representation of the $\mathbf{E} \times \mathbf{B}$ drift of a charged particle along a uniform magnetic field and electric field. The magnetic field points out of the page, the electric field is directed up, and the drift direction is orthogonal to both $\mathbf{E}$ and $\mathbf{B}$ shown by the arrow in the direction $\mathbf{E} \times \mathbf{B}$. The red curve represents the path of a proton and the black curve represents the path of an electron. The Figure is adapted from Bittencourt (2004).

$E_{||}$ only. This means that under the influence of $E_{\perp}$, the ions and electrons drift in the same direction with a common drift speed of $\frac{E_{\perp}}{B}$. This also means that E cross B drift velocities do not induce currents in the plasma. If we combine this drift of the particle with the gyration of the particle along the magnetic field, we see that the particle is accelerated for half its gyration by the electric field and decelerated for the other half of the gyration, as seen from Figure 1.2.

The general description for a drift is that any external force acting perpendicular to the magnetic field cyclically accelerates/decelerates the charged particle as it gyrates about the magnetic field. This alters the Larmor radius at different parts of the orbit and results in a drift of the guiding centre perpendicular to the external force and the magnetic field. If we replace the electric force, $qE_{\perp}$, in Equation (1.18) with a general external perpendicular force, $\mathbf{F}_{ext}$ and undertake the same mathematical treatment, we obtain the drift equation under the presence of an $\mathbf{F}_{ext}$:

$$\mathbf{V}_F = \frac{\mathbf{F}_{ext} \times \mathbf{B}}{qB^2} \tag{1.21}$$

where $\mathbf{V}_F$ is the drift that arises due to external force. Equation (1.21) shows that if $\mathbf{F}_{ext}$ is charge-independent, then the drift direction depends on the sign of the charged particle, which thus gives rise to currents perpendicular to the magnetic field.

1.2.2 Adiabatic Invariants

An adiabatic invariant is a property of a system that arises from periodicities of motion such as gyration and stays approximately constant when perturbations made to the system occur slowly on timescales much larger than the periodicity (Kivelson and Russell, 1995). A notable feature of a charged particle's motion in a collisionless plasma is that a quantity called the magnetic moment of a particle stays constant if the field changes encountered by a charged particle within a single gyration period are small compared to the average magnetic field. The magnetic moment, μ, is called the first adiabatic invariant and is defined as:

$$\mu = \frac{mv_\perp^2}{2B} \tag{1.22}$$

Equation (1.22) shows that, if the magnetic moment is conserved, as a particle travels along a magnetic field line with slowly increasing magnetic field strength, the velocity perpendicular to the magnetic field line increases. This in turn results in a corresponding decrease in the parallel velocity in order to conserve the total kinetic energy of the particle i.e. the pitch angle (Equation (1.15)) move towards 90°, to maintain the magnetic moment. With increasing magnetic field strength, the pitch angle tends towards 90° to maintain constant kinetic energy, i.e., all the particle's velocity is directed in the perpendicular direction. Once the pitch angle has reached 90°, the particles reverse its direction of motion and continue to follow the magnetic field with decreasing field strength with pitch angle approaching either 0° or 180 °. This turning point is called the mirror point. This is due to an effective force exerted along the field in the direction of decreasing field strength, which causes the

particle to turn around at its mirror point, this force is called the "mirror force". For this thesis, we only highlight the first invariant, but note that there are additional adiabatic invariants that can arise due to other periodicities in the plasma, such as mirror trapped motion in Coronal Mass Ejection (CME) flux ropes.

1.2.3 Frozen-in Flux

The frozen-in flux theorem describes the behaviour of particles and magnetic fields of a highly conductive plasma. The theorem states that in a perfectly conductive plasma, the magnetic field lines are frozen into the plasma (Baumjohann and Treumann, 2012). This means that the plasma and the magnetic fields move together, such that the magnetic flux moving with the plasma remains constant through any given closed surface. In a collisionless plasma with infinite conductivity, this theorem can be expressed as (Baumjohann and Treumann, 2012):

$$\frac{\partial \mathbf{B}}{\partial t} = \nabla \times (\mathbf{v}_b \times \mathbf{B}) \tag{1.23}$$

where $\mathbf{v}_b$ is the bulk velocity of the plasma. Equation (1.23) describes the changes in the magnetic field, such that the magnetic field is constrained to move with the conductive plasma. The cross product between the flow velocity and the magnetic field tells us that a highly conductive plasma can flow freely in the along the magnetic field line, but the field lines are carried by any motion of the plasma perpendicular to the field lines (Bittencourt, 2004). Furthermore, equation (1.23) implies that the total magnetic flux through a closed surface, S, remain constant even if the surface changes its shape and location.

This frozen in flux principle is schematically illustrated in Figure 1.3, where the initial closed surface, S at time t_1, the same closed surface at time t_2 and the enclosed volume between the two surfaces is called a flux tube. The frozen in flux theorem states for an infinitely conductive plasma, the magnetic flux and all the particles contained in a certain flux tube stay constant at any instance regardless of the motion of the flux tubes and the changes in the form of the closed surfaces.

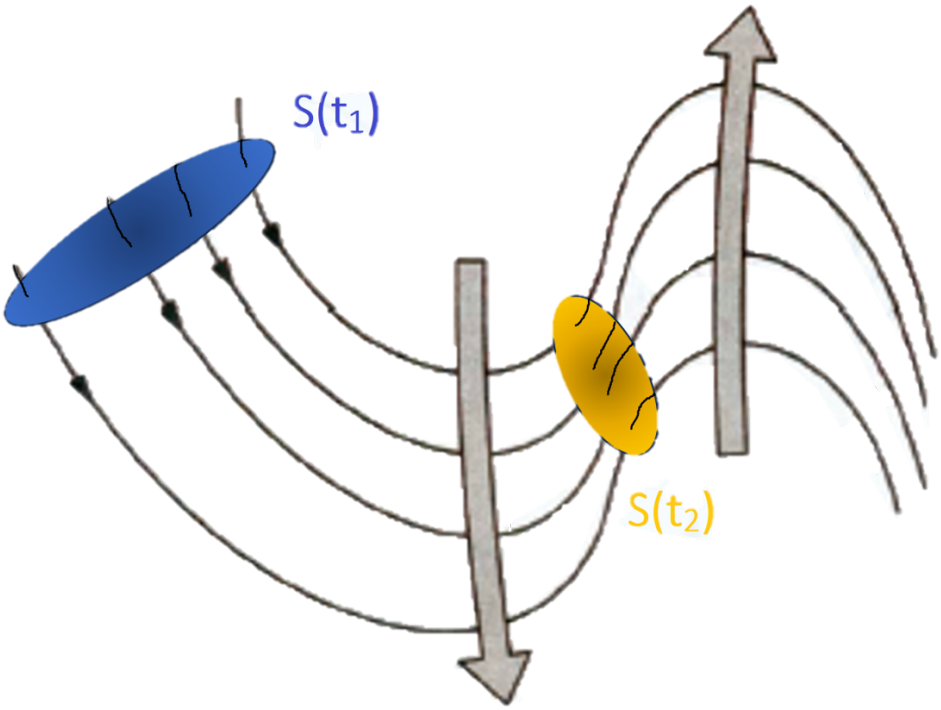

Figure 1.3: Schematic illustration of the frozen-in flux. The black lines represent the magnetic field lines, and the arrows indicate the direction of the motion of the magnetic field with the plasma. The plasma particles and the magnetic flux bounded by the blue closed surface $S(t_1)$ at time t_1 is the same as at time t_2 shown in orange. This Figure is adapted from Bittencourt (2004).

1.3 Plasma kinetic theory

In the previous subsections, we examined the motion of a single test particle in prescribed electric and magnetic fields. Plasma kinetic theory addresses the collective behaviour of (plasma) particles as a statistical ensemble. Each particle can be fully described by its position (**q**) and velocity (**v**) in phase space, a 6-dimensional space defined as three spatial coordinates (x, y, z) and three velocity coordinates (V_x, V_y, V_z). To consider each individual particle in the ensemble is not a feasible endeavour, so it is usual practice to define the number of particles in a given volume of phase space $(dx, dy, dz, dV_x, dV_y, dV_z)$, called a phase space density, commonly referred to as the distribution function, f(**q**,**v**,t) $dqdv$. When position and temporal evolution of the population is not considered, f(**q**,**v**,t) reduces to a velocity distribution function (VDF), f(**v**).

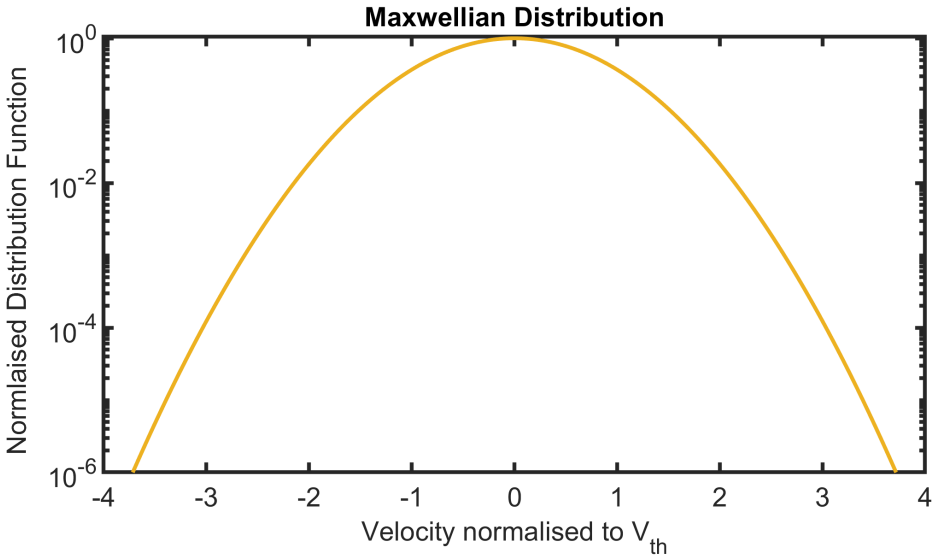

Figure 1.4: An example of a normalised distribution function of a 1D Maxwellian plotted against normalised velocity. The VDF is normalised such that the maximum value is 1. The velocity is plotted as a ratio of average thermal velocity,V_{th} of all the particles in the distribution, where $V_{th} = \sqrt{\frac{2kT}{m}}$.

The VDF for a plasma population in thermal equilibrium can be described by a Maxwellian distribution (Feldman et al., 1975; Baumjohann and Treumann, 2012). The functional form of a Maxwellian distribution in an isotropic plasma is:

$$f(\mathbf{v}) = n\left(\frac{m}{2\pi kT}\right)^{\frac{3}{2}} e^{-\frac{mv^2}{2kT}} \tag{1.24}$$

where m is the mass of the particle. The Maxwellian is defined by temperature, T, and number density, n. Figure 1.4 shows a typical 1-dimensional Maxwellian as a function of velocity.

In the presence of a magnetic field in the plasma, the VDF is often anisotropic. Anisotropic means that the parallel and perpendicular temperatures with respect to the magnetic field are different, unlike in an isotropic case where they are the same. An anisotropic distribution requires two independent temperature components that are independent, such a distribution function can be represented as the product of two Maxwellian distribution functions. This type of distribution is called

a bi-Maxwellian model, and can be expressed as:

$$f(v_{||}, v_{\perp}) = \left(\frac{n}{T_{\perp} T_{||}^{\frac{1}{2}}}\right) \left(\frac{m}{2\pi k}\right)^{\frac{3}{2}} e^{\left(-\frac{mv_{||}^2}{2kT_{||}} - \frac{mv_{\perp}^2}{2kT_{\perp}}\right)} \tag{1.25}$$

where $T_{||}$ is the parallel temperature and $T_{\perp}$ is the perpendicular temperature with respect to the magnetic field. Figure 1.5 schematically illustrates VDFs of isotropic, anisotropic and streaming distributions plotted as contours in velocity space. The colours represent the value of the phase space density. Panel A shows an isotropic distribution, where $T_{||} = T_{\perp}$. Panel B shows an anisotropic distribution where $T_{||} > T_{\perp}$. Compared to the isotropic distribution, the anisotropic distribution contours take an elongated shape. The distribution in Panel C shows a streaming distribution where the circle contours are circular and centred around a non-zero $V_{||}$. Another common type of distribution observed in space plasma is the kappa distribution (Feldman et al., 1975; Marsch, 2006; Maksimovic et al., 1997; Maksimovic et al., 2005; Štverák et al., 2009; Abraham et al., 2022a), although the exact causes for the creation of these distributions are still unknown (Livadiotis, 2019). The kappa distribution can be expressed as:

$$f(\mathbf{v}) = n \left(\frac{m}{2kT\pi\left(\kappa - \frac{3}{2}\right)}\right)^{\frac{3}{2}} \frac{\Gamma(\kappa+1)}{\Gamma(\kappa - \frac{1}{2})} \left[1 + \frac{m\mathbf{v}^2}{2kT\left(\kappa - \frac{3}{2}\right)}\right]^{-(\kappa+1)}, \tag{1.26}$$

where Γ represents the gamma function and κ represents the kappa parameter. Representations of 1-D κ distributions as functions of velocity with varying κ values are shown in Figure 1.6. Low values of κ capture more pronounced and extended tails in a distribution. As κ tends to infinity, the distribution becomes Maxwellian (Livadiotis and McComas, 2013).

Measurements of distribution functions do not immediately provide bulk physical parameters that are useful in understanding the nature of the plasma. To obtain bulk properties of the plasma, we have to take the moments of the distribution function f(**v**). The n^{th} velocity moment at a given point in real space is calculated by

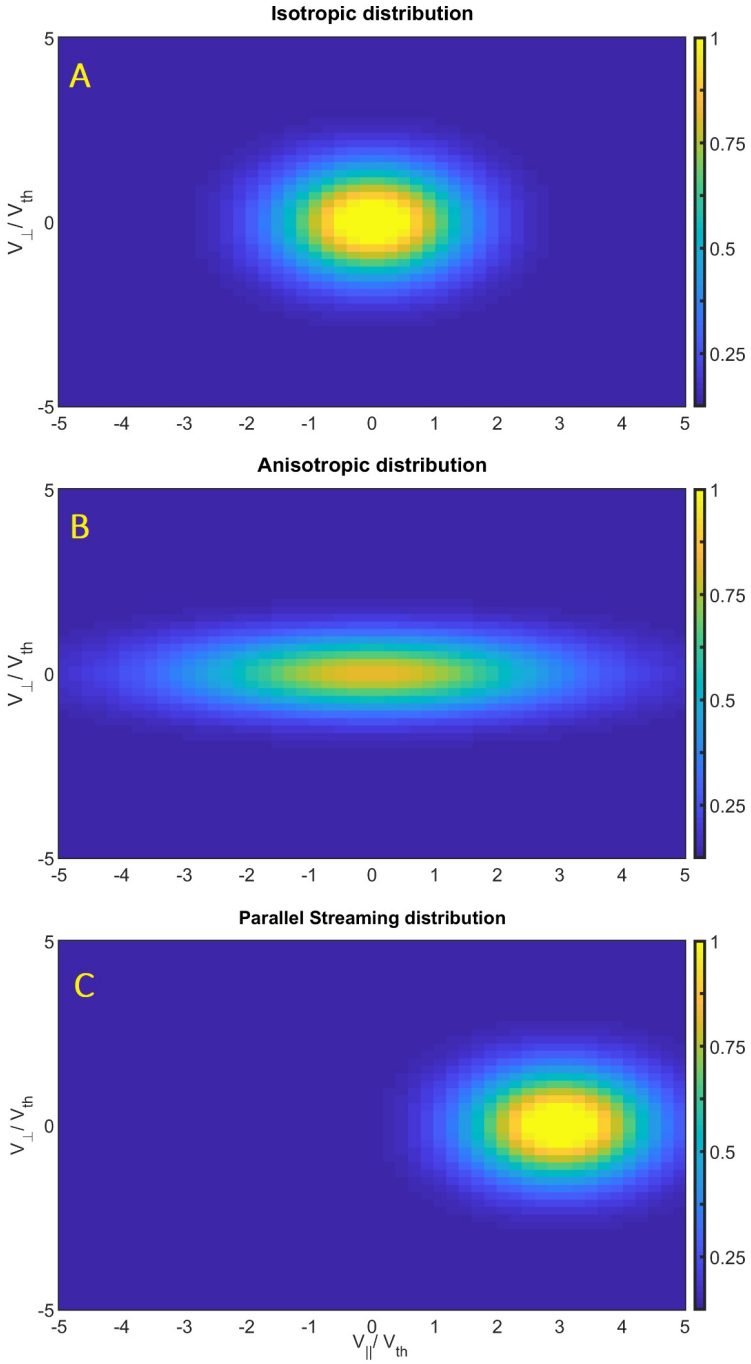

Figure 1.5: A schematic illustrating 2D contours of normalised bi-Maxwellian distribution function. The x-axis represents $V_{||}$ normalised to the thermal velocity,V_{th}, where $V_{th} = \sqrt{\frac{2kT}{m}}$. The y-axis is $V_{\perp}$ normalised to the thermal velocity. The colour bar represents the distribution function divided by the maximum value of the distribution function, where the maximum value is 1. Panel A represents an isotropic distribution, Panel B represents an anisotropic distribution and Panel C represents an isotropic parallel streaming distribution i.e. the isotropic distribution function that is centred around a non-zero value.

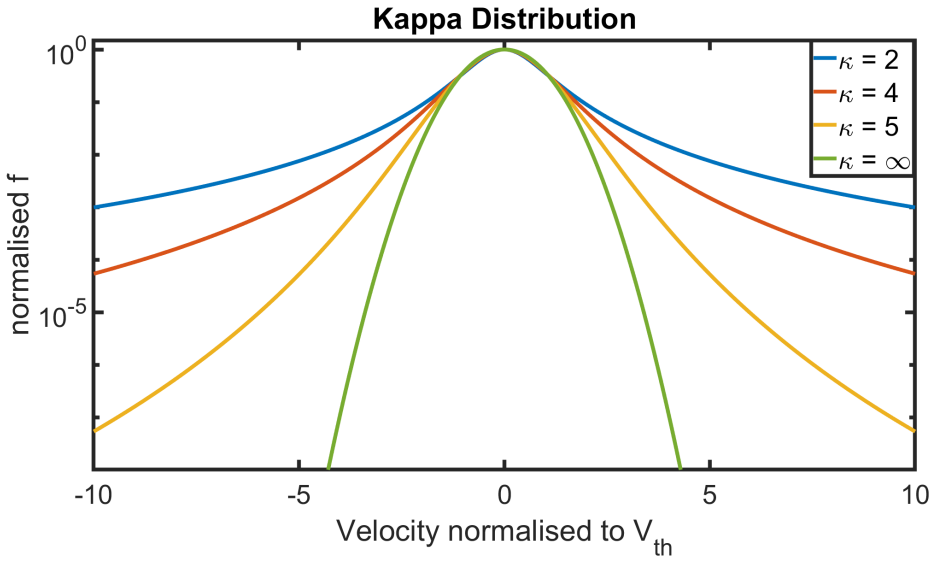

Figure 1.6: Examples of 1D kappa normalised distribution functions for varying κ values of 2, 4, 5 and ∞. The x-axis represents the velocity normalised to the thermal speed and the y-axis shows the distribution function normalised to the maximum value of the distribution function. As $\kappa \to \infty$, the distribution is identical to a Maxwellian distribution.

integrating over all the velocity space components weighted by $\mathbf{v}^n$ (Kivelson and Russell, 1995). In principle, there are an infinite number of velocity moments, but only the four lowest moments have physical relevance for our study. The zeroth moment provides the number density:

$$n = \int f(\mathbf{v}) d^3\mathbf{v} \tag{1.27}$$

The first order moment represents the bulk velocity, $\mathbf{v}_b$

$$\mathbf{v}_b = \frac{1}{n} \int \mathbf{v} f(\mathbf{v}) d^3\mathbf{v} \tag{1.28}$$

The bulk velocity describes the average flow velocity of the particle population. The second moment represents the pressure tensor, P, by taking the ensemble of the squared difference between the particle velocity and the average bulk velocity:

$$\mathsf{P} = m \int (\mathbf{v} - \mathbf{v}_b)(\mathbf{v} - \mathbf{v}_b) f(\mathbf{v}) d^3\mathbf{v} \tag{1.29}$$

The third moment describes the heat flux vector, **q**, a useful quantity in describing the flow of heat in the plasma, which can be different from the mean mass flow of the plasma:

$$\mathbf{q} = \frac{m}{2}\int (\mathbf{v}-\mathbf{v}_b)(\mathbf{v}-\mathbf{v}_b)(\mathbf{v}-\mathbf{v}_b) f(\mathbf{v}) d^3\mathbf{v} \tag{1.30}$$

The fundamental equation that governs the evolution of a particle distribution function in phase space is called the Boltzmann equation (Kivelson and Russell, 1995):

$$\frac{\partial f}{\partial t} + \mathbf{v}\cdot\nabla_{\mathbf{r}} f + \mathbf{a}\cdot\nabla_{\mathbf{v}} f = \left(\frac{df}{dt}\right)_{Coll}, \tag{1.31}$$

where $\nabla_{\mathbf{r}}$ is the gradient in configuration space, $\nabla_{\mathbf{v}}$ is the gradient in velocity space, **a** is the acceleration due to external forces and $\left(\frac{df}{dt}\right)_{Coll}$ is the change in the distribution function due to collisions. As collisions are generally rare in space plasmas, the right-hand side of Equation (1.31) can often be set to zero:

$$\frac{\partial f}{\partial t} + \mathbf{v}\cdot\nabla_{\mathbf{r}} f + \mathbf{a}\cdot\nabla_{\mathbf{v}} f = 0 \tag{1.32}$$

Equation (1.32) is commonly called the 'Collisionless Boltzmann equation' and can also be expressed as a total derivative:

$$\frac{df}{dt} = 0 \tag{1.33}$$

Equation (1.33) shows that the derivative of the distribution function along a particle trajectory is always zero for an ensemble of collisionless particles. This means that for an observer moving in phase space with any particle in the ensemble, the distribution function remains constant. This is known as the Liouville theorem. Applying Equation (1.8) to (1.32) to describe a scenario where the plasma experience forces associated with electromagnetic fields only, the following expression is obtained:

$$\frac{\partial f}{\partial t} + \mathbf{v}\cdot\nabla_{\mathbf{r}} f + \frac{q}{m}(\mathbf{E}+\mathbf{v}\times\mathbf{B})\cdot\nabla_{\mathbf{v}} f = 0 \tag{1.34}$$

Equation (1.34) is called the Vlasov Equation. The Vlasov equation does not consider any local short-range interactions, such as a Coulomb collision, between charged particles. It is thus only valid on scales of the order of collective interaction scale or larger (Baumjohann and Treumann, 2012), over which particle motion is influenced by the average field created by many particles. These fields are said to be self-consistent; this means the electromagnetic fields are determined by the plasma, and therefore they depend on the distribution function.

Chapter 2

The Solar Wind

The solar wind is a continuous outflow of a highly conductive plasma from the Sun that expands radially outwards from the solar corona into interplanetary space (Parker, 1963). The first measurement of the solar wind was made by Luna 2, which detected a solar particle flux outside the Earths magnetosphere, in the 1960s (Gringauz and Rytov, 1961). The concept of the solar wind had been first postulated in the early 20th century as an intermittent flow of ionised plasma to explain the formation of the aurorae (Chapman and Ferraro, 1940). Many space borne observations since then have made detailed measurements of the solar wind from within the orbit of Mercury to beyond the orbit of Saturn (Kohlhase and Penzo, 1977; Wenzel et al., 1992; Fox et al., 2016). In this Chapter, we will outline some key developments in this field, upon which the research in this thesis is developed. In Section 2.1 we will provide a general survey of the properties of the solar wind. Solar wind plasma is predominately composed of protons, electrons, and a few percent of heavier ions. The protons contribute to most of the mass and momentum fluxes in the solar wind due to their greater mass, while the relatively light electrons play a key role in solar wind dynamics as the main carrier of thermal energy due to their much larger thermal speeds (Marsch, 2006).

In this thesis, we will be examining the electron population of the solar wind. In Section 2.2 of this Chapter, we will outline the current research in understanding of the evolution of electron population. Finally, in Section 2.4 we will summarise a kinetic model of the solar wind, called the exospheric model, and its implication on

the evolution of the solar wind electron distribution functions.

2.1 Observational properties of the solar wind

In-situ observations of the solar wind near 1 au revealed that the solar wind speed varies from 300 $km\ s^{-1}$ to 1400 $km\ s^{-1}$ (see Marsch (2006) and references therein). Traditionally, solar wind streams with bulk velocity less than 500 $km\ s^{-1}$ are generally called slow solar wind, and solar wind streams with bulk velocity greater than 500 $km\ s^{-1}$ are called fast solar wind (Marsch, 2006). Taking an average solar wind speed of 500 $km\ s^{-1}$, the solar wind takes approximately 4 days to travel from the Sun to the Earth. Due to frozen in conditions, the solar wind carries the heliospheric magnetic field with it. Figure 2.1 shows observations of solar wind speed distributed across different heliographic latitudes as measured by Ulysses spacecraft during its first two orbits (McComas et al., 2003). The first orbit occurred during a solar minimum and the second orbit during a solar maximum. Solar maximum and minimum refer to periods of maximum and minimum solar activity during one solar cycle. The solar cycle has an average period of 11 years (Kivelson and Russell, 1995). It can be noted that, during solar minimum, the fast wind emerges from polar coronal holes dominated by open field lines and slow wind emerges from the equatorial plane (McComas et al., 2003). During solar maximum the picture is unclear and fast and slow flows may emerge from all heliographic latitudes.

On average, the slow solar wind is denser with approximately 8 ions cm^{-3}, compared to 4 ions cm^{-3} for the fast wind at 1 au (Maksimovic et al., 2005; Štverák et al., 2009). The slow wind is observed to be highly variable in its plasma parameters, it contains large structures such as magnetic clouds and shocks, whereas the fast wind is less variable (Baumjohann and Treumann, 2012). The solar wind is observed to be mostly collisionless because the density of the particles in the solar wind is very low combined with large temperature means that the probability of Coulomb collisions is very small (Marsch, 2006). The fast wind is less collisional than the slow wind, which means non-thermal kinetic features in the distribution functions can prevail further into interplanetary space (Jockers, 1970; Feld-

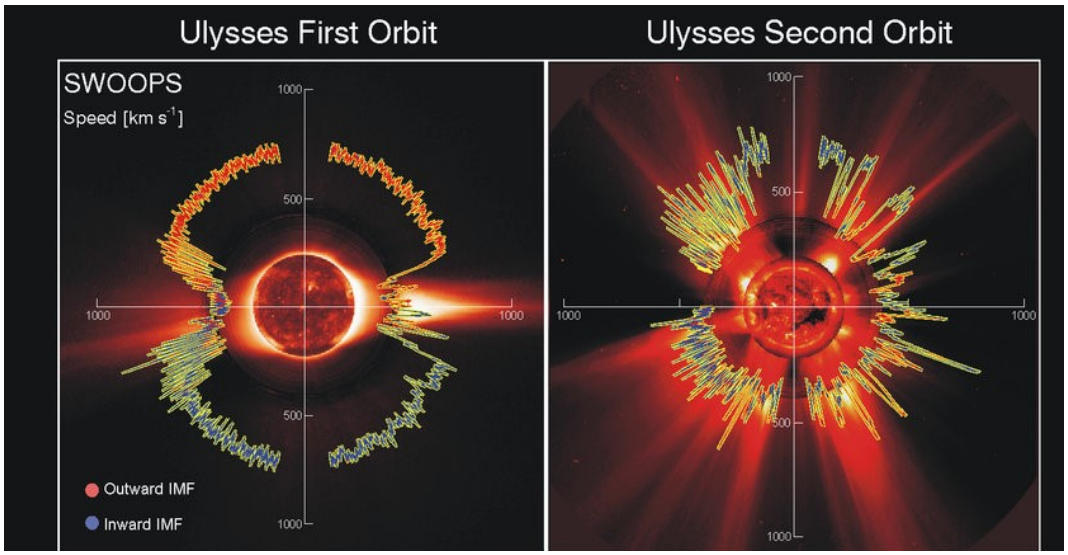

Figure 2.1: Ulysses's measurements of the solar wind speed as a function of heliographic latitudes. The red line represents the outward polarity of the Sun's magnetic field, and the blue lines represents the inward polarity of the Sun's magnetic field. The right-hand panel was taken during the first orbit of Ulysses (solar minimum) and the left-hand panel was taken during the second orbit (solar maximum). The x and y axis represents solar wind speed in kms^{-1}. This Figure is adapted from McComas et al. (2003)

man et al., 1975, 1979). The relationship between various wind streams and various source areas raises the possibility that the magnetic-field configuration in the corona significantly influences the characteristics of the wind streams (Marsch, 2006).

2.1.1 Interplanetary magnetic field

The magnetic field carried away by the solar wind from the Sun is called the Interplanetary Magnetic field (IMF). It plays a fundamental role in influencing the local properties of the solar wind evolution (Parker, 1963). The solar wind flow is highly electrically conductive and the motion of solar wind with the IMF is explained by the frozen-in flux theorem described in Chapter 1.

While the magnetic field foot points are frozen in the corona, the solar wind radial outflow convects the magnetic field from the corona to interplanetary space (Baumjohann and Treumann, 2012). The Sun rotates with an average period of 27 days and this means the IMF will not maintain a radial form as the plasma propagates radially out from the solar corona. Figure 2.2 shows a schematic of the magnetic field structure which arises from the radial outflow of the solar wind and

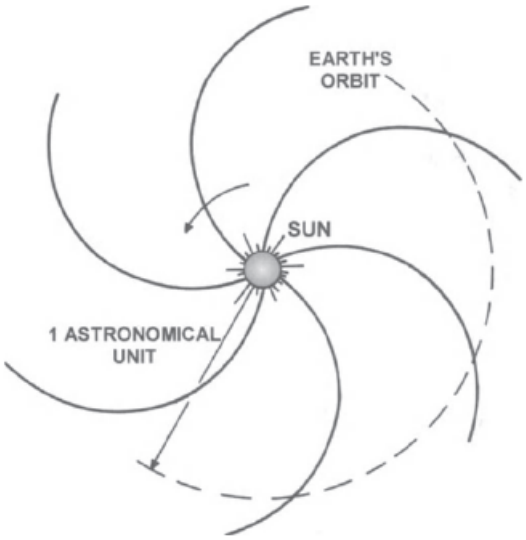

Figure 2.2: Schematic of the Archimedean Spiral form of the IMF around the Sun. The black lines represent the magnetic field, the arrow represents the rotation of the Sun and the dashed circle represents the orbit of the Earth. This Figure is taken from Bittencourt (2004)

the solar rotation. The IMF takes the form of an Archimedean spiral also known as Parker Spiral (Parker, 1963). The Parker Spiral is the long term average shape of the IMF in the equatorial plane.

2.2 Solar Wind Electrons

A central open question of solar wind dynamics is the regulation of the thermal energy and the role and nature of the electron velocity distribution as a function of radial distance (Feldman et al., 1975; Marsch, 2006). The solar wind is observed to be mostly collisionless, which means above a certain energy the particle velocity distributions may deviate from the classical isotropic Maxwellian distribution (Feldman et al., 1975; Maksimovic et al., 2005; Marsch, 2006). Observations have shown that the electrons in the solar wind can often be categorised into three populations: the core, the halo and the strahl (Feldman et al., 1975; Maksimovic et al., 2005; Štverák et al., 2009). The part of the electron population with energy < 50 eV is considered to be the core population, and is usually well described by a bi-Maxwellian distribution function. The core makes up 90-95% of the total electron density (Maksimovic et al., 2005). The bi-Maxwellian nature of the core can be

understood as the result of collisions, but as we move to higher energies, where collisions become less significant, non-equilibrium structures, such as beams and high-energy tail may develop (Feldman et al., 1975; Marsch, 2006). In particular, the suprathermal tails of the electron velocity distribution function (eVDF) can be characterised into two parts: halo and strahl (Feldman et al., 1975; Maksimovic et al., 2005; Štverák et al., 2009). The halo population exhibits a higher temperature than the core and is often described by a bi-kappa distribution. Both the core and the halo are quasi-isotropic and thus show significant fluxes at all pitch angles. In contrast, the strahl is usually seen as a strongly field-aligned beam of electrons which is observed to be moving either parallel, antiparallel, or both, to the local magnetic field (Feldman et al., 1975; Scudder and Olbert, 1979; Gosling et al., 1987; Maksimovic et al., 2005; Štverák et al., 2009; Graham et al., 2017; Halekas et al., 2020).

Due to the field aligned nature of the strahl, it can also be used to indicate the global structure of the heliospheric magnetic field. The origins of the suprathermal populations remain actively studied and poorly understood. The weak collisionality of the suprathermal electrons mean that they are believed to carry an imprint of the information about the conditions near the Sun into the heliosphere (Scudder and Olbert, 1979; Hefti et al., 1999; Berčič et al., 2020). The strahl population is reported to be seen more often in the fast wind compared to the slow wind (Rosenbauer et al., 1977). Figure 2.3 shows a typical solar wind eVDF measured in the fast solar wind at 1 au by the Helios spacecraft. The main core population is surrounded by a hotter halo population, and the clear elongation along the magnetic field indicates the presence of the strahl population. These descriptions of the electron populations were based on numerous observations of the solar wind from 0.3 au outwards, where the solar wind travels with supersonic speeds (Feldman et al., 1975; Scudder and Olbert, 1979; Gosling et al., 1987; Rosenbauer et al., 1977; Maksimovic et al., 2005; Štverák et al., 2009; Berčič et al., 2020; Halekas et al., 2020).

A classical collisional distribution model cannot be used to describe the full electron distribution, as it fails to capture the non-Maxwellian features exhibited by

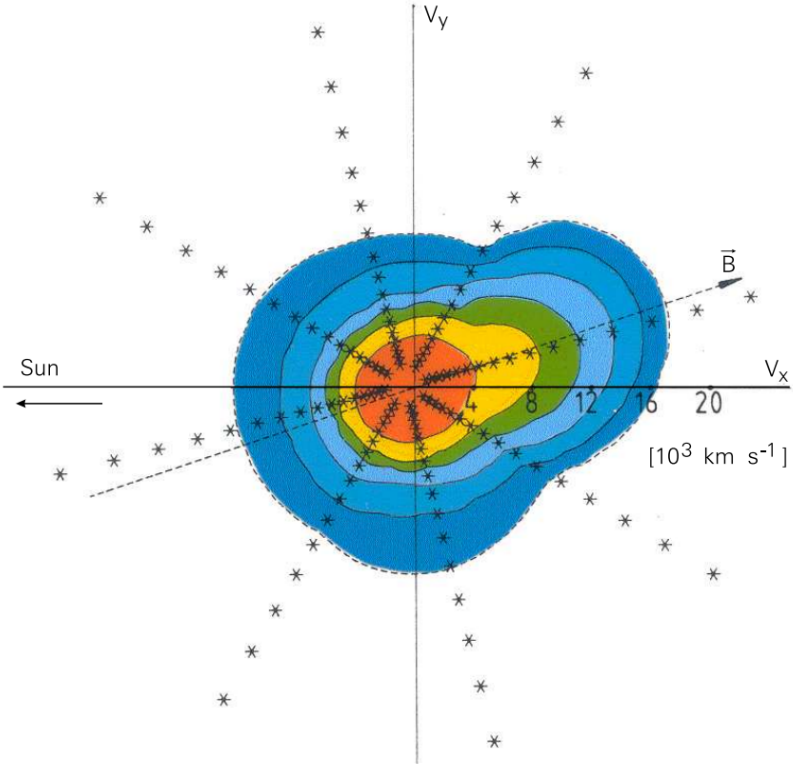

Figure 2.3: Electron velocity distribution function in the solar wind as measured by the plasma instrument on the Helios spacecraft at 1 au. The dashed line with an arrowhead represents the magnetic field direction. The asterisk lines represent the 8 measurement bins of the Helios spacecraft. The distinct extension of the VDF along the magnetic field is the strahl, the core is indicated in red and the hotter quasi isotropic population around the core is called the halo. The contours represent constant total velocity. This Figure is taken from Marsch (2006).

the suprathermal electrons. Maksimovic et al. (2005) fit the three populations by first fitting the core and halo respectively as a bi- Maxwellian and a bi-kappa function, defined in velocity space in the magnetic field-aligned frame. In this study, once the core and halo are fitted well, the resulting model core-halo distribution is subtracted from the observed distribution, and the remaining population is integrated in velocity space to obtain strahl density. Štverák et al. (2009) also fit the core with a bi-Maxwellian distribution and the halo and strahl with a truncated bi-kappa distribution. Both studies show that the non-thermal halo population can be modelled well by a bi-kappa function and the thermal core with a bi-Maxwellian function, but there is not an accepted common method to model the strahl. Štverák

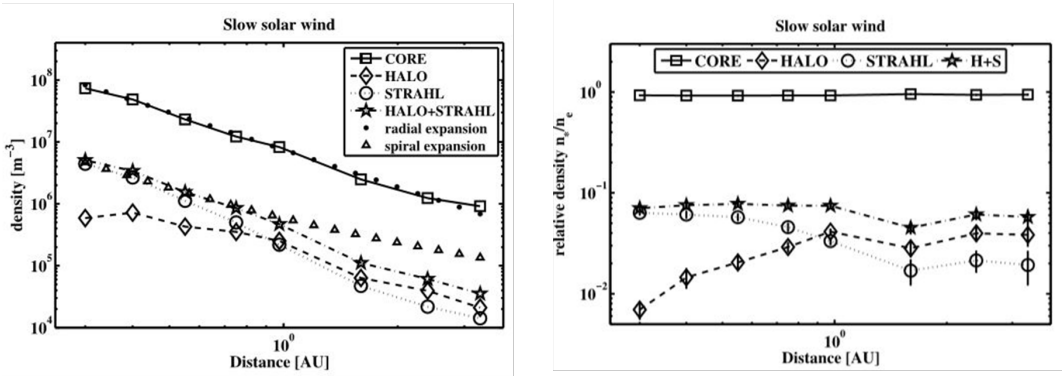

Figure 2.4: The radial evolution of the core, halo and strahl parameters during slow solar wind regimes. The left panel shows the evolution of the electron population density with heliocentric distance. It also compares the measured density profiles with theoretical spiral and radial expansion profiles in the slow wind. The right panel shows the evolution of the relative density of each population with the total electron density with heliocentric distance for slow wind. This Figure is taken from Štverák et al. (2009)

et al. (2009) show that below 0.5 au the strahl can be well described with a bi-Maxwellian distribution.

Observations from Helios show that the relative density of the core population with respect to the total electron density remains constant as the solar wind expands, as seen in Figure 2.4. It also shows that the relative densities of the halo and strahl vary in an inverse way over the distance range covered, whilst maintaining the total suprathermal relative density constant. The trend between the suprathermal electron populations indicates that the strahl electrons may be scattered into the halo with increasing radial distance via some process/processes, whilst leaving the core unaffected (Maksimovic et al., 2005; Štverák et al., 2009). Figure 2.4 also shows the core density evolution is in an excellent agreement with the prediction for an isotropic expansion, since the core density, as a function of radial distance r, drops as r^{-2}. In contrast, the halo and strahl populations show more complex evolution than a steady radial expansion from 0.3 au. The overall suprathermal density profile in Figure 2.4 is consistent with a spiral expansion profile up to a point, $\sim$ 1 au, which may be due to the fact that the most abundant suprathermal population is the strahl below 1 au. Compared to the core, the relative density of the suprathermal population is only about 5-10 % of the total electron density for the slow solar wind.

Another interesting observation is that the contribution of the halo closer to the Sun is almost negligible, which suggests that the halo may not be present closer to the Sun.

The origin of the variation in the halo and the strahl remains elusive, although many authors (e.g. Saito and Gary (2007); Vocks et al. (2005); Verscharen et al. (2019)) have proposed different mechanisms that scatter strahl electrons into the halo while the core remains unaffected. Moreover, Berčič et al. (2020) show that the strahl parallel temperature does not vary with radial distance up to 1 au, which again implies that the strahl population retains information relating to the source coronal temperature. The origins of the strahl are still not well understood, although it is thought to originate from the corona (Hefti et al., 1999).

Under purely adiabatic conditions, the strahl population should continue to narrow in pitch angle as it propagates radially away from the Sun and into regions of lower magnetic field strength, in order to conserve the particle magnetic moments. This adiabatic focusing would result in the strahl taking the shape of a highly field-aligned beam-like population with decreasing strahl pitch angle width with distance. However, observations have shown that the typical strahl pitch angle width is observed to be much greater than the few degrees expected for the purely adiabatic case near 1 au (Hammond et al., 1996; Anderson et al., 2012; Graham et al., 2017). Owens et al. (2008) create a simple model that examines the combined effects of adiabatic focusing and an ad-hoc constant rate of scattering on the strahl population. According to this model, beyond ~ 0.1 au, the constant scattering rate dominates over the adiabatic focusing and the strahl pitch angle width increases with heliocentric distance. This model is illustrated in Figure 2.5 and explained in the caption. The observations made by Hammond et al. (1996) show that the degree to which strahl pitch angle width increases with radial distance is energy dependent, and that low-energy electrons display greater broadening per astronomical unit than those of higher energies.

The exact nature of the scattering mechanism of the strahl remains elusive. It has been proposed that this scattering mechanisms may include wave particle

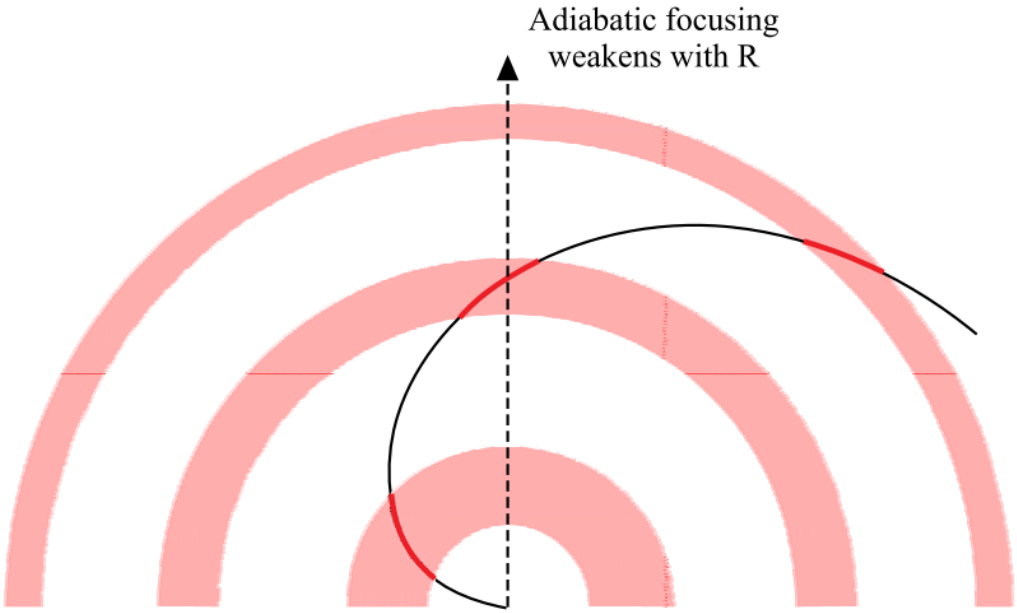

Figure 2.5: The red intervals along the spiral field line show the distance an electron of a given energy can move in a fixed unit of time, with red-shaded regions showing the associated change in heliocentric distance. Close to the Sun, field lines are nearly radial so that electrons experience a large change in r and field strength per unit time and, thus, strong adiabatic focusing. Far from the Sun, the angle between the field and the radial direction is much larger so that electrons experience a smaller change in field strength per unit time and weaker focusing. Consequently, the strahl broadens at greater heliocentric distances, although the scattering rate is constant. This Figure is taken from Owens et al. (2008).

interactions (Vocks et al., 2005). The relationship between strahl width and energy can help us understand the role of the scattering mechanism. A conclusive result has yet to emerge: some studies find that the strahl width decreases with energy (Fitzenreiter et al., 1998), others find that the strahl width can increase with energy (Pagel et al., 2007). Hammond et al. (1996) show that there is no strong correlation between the strahl width and energy. Anderson et al. (2012) show that it is equally probable that strahl width could increase or decrease with energy.

2.2.1 Electron Energetics

The question of solar wind heating is one of the long-standing fundamental problems in heliophysics (Viall and Borovsky, 2020). One way to address the heating problem is by considering the temperature profiles. From a theoretical perspective, for a purely adiabatic expansion the temperature should decrease with a radial pro-

file of $r^{-4/3}$, while for a purely Coulomb collision scenario the temperature profile decreases with radial distance as r $^{-1/3}$ (Scudder and Olbert, 1979). Observations have shown that the temperature of the overall electron population decreases more slowly than adiabatic expansion, but much faster than an isothermal profile (Feldman et al., 1979; Pilipp et al., 1990; Scime et al., 1994; Maksimovic et al., 2000; Štverák et al., 2015). The temperature profile approximately varies from $r^{-0.5}$ – $r^{-0.7}$. Meanwhile, in the fast solar wind, the profile varies as $r^{-0.3}$ to $r^{-0.4}$ (Štverák et al., 2015).

The variation in the temperature profiles reveals the presence of a non-adiabatic heating process. To understand the nature of the mechanisms involved in the non-adiabatic heating, we have to first examine the electron energetics to help quantify the flow of thermal energy. Pilipp et al. (1990) provide a basic formulation of the electron energetics based on the heat flux. Explaining the properties of an observed fast stream reported in their study require invoking external heating, while those of an observed slow stream did not need external heating at distances between 0.3 and 1 au. However, due to the limited data set used in their study, assessment of the full global evolution of the thermal energy budget was not possible. More recently, work on the solar wind electrons energy budget is presented by Štverák et al. (2015). Using an approximation of the thermal energy balance, their study finds that the effective electron heating rates are negative for both the slow and fast solar wind, since there is a significant degradation of the electron heat flux with increasing radial distance from the Sun. Cooling mechanisms acting on electrons are found to be significantly stronger in the slow wind than in the fast wind streams. In addition, this study highlights that the observed non-adiabatic electron cooling is not driven by any external process, but rather a direct consequence of mechanisms that exchange and redistribute the internal electron energy from the parallel to the perpendicular degrees of freedom. If there is a rapid cooling of the solar wind electrons, then it is reasonable to expect the temperature profiles to drop faster than $r^{-\frac{4}{3}}$, but this is not the case. These studies highlight that the balance of thermal energy of the electrons as a function of radial distance still needs to be better established. We address this

topic in Chapter 5.

2.3 Parkers Hydrodynamic Model

Parker (1958) argued that the corona is not a static atmosphere because of the high temperature, but is blown away and continually expanding as the interstellar pressure cannot contain a static corona.This expansion is called the solar wind. Aspects of this model were later confirmed by the Mariner II in the early 1960s (Neugebauer and Snyder, 1966). Using the equations for conservation of mass and momentum, Parker (1958) undertook a hydrodynamic approach and the solution to the time-independent symmetric equation of motion, which describes how the speed of the solar wind varies with distance, was of the following form:

$$\frac{1}{\mathbf{u}}\frac{d\mathbf{u}}{dr}\left(\mathbf{u}^2 - \frac{2kT}{m}\right) = \frac{4k_BT}{mr} - \frac{GM}{r^2} \tag{2.1}$$

where $\mathbf{u}$ is the radial expansion speed, G is the gravitational constant, M is the mass of the Sun. Integrating Equation 2.1 results in five mathematically feasible solutions, shown in Figure 2.6 (Parker, 1958).

In solution, I and IV, the solar wind starts as a subsonic flow in the corona and develops differently. For Solution IV, the flow speed increasing with height but at some height the flow propagates radially outwards and slows down. Solution IV can be thought as the 'solar breeze'. In solution I, the flow has accelerated away from the lower corona to supersonic speed before reaching the critical height. It then turns around and flows back towards the Sun as a supersonic flow, which has not been observed. Solution III shows that a flow leaving the Sun at supersonic speeds which then decelerates a little with height but is still supersonic at the critical radius and as the flow propagate radially outwards the flow continues to accelerate while still remaining in the supersonic regime which has not been observed. Solution II is completely different, as the wind flows from infinity towards the Sun at supersonic speed and then gets turned back and propagates radially outwards at supersonic speed. Solution V is often noted as that corresponding to the observed quiet solar wind: the flows start in the corona at subsonic speed and gradually in-

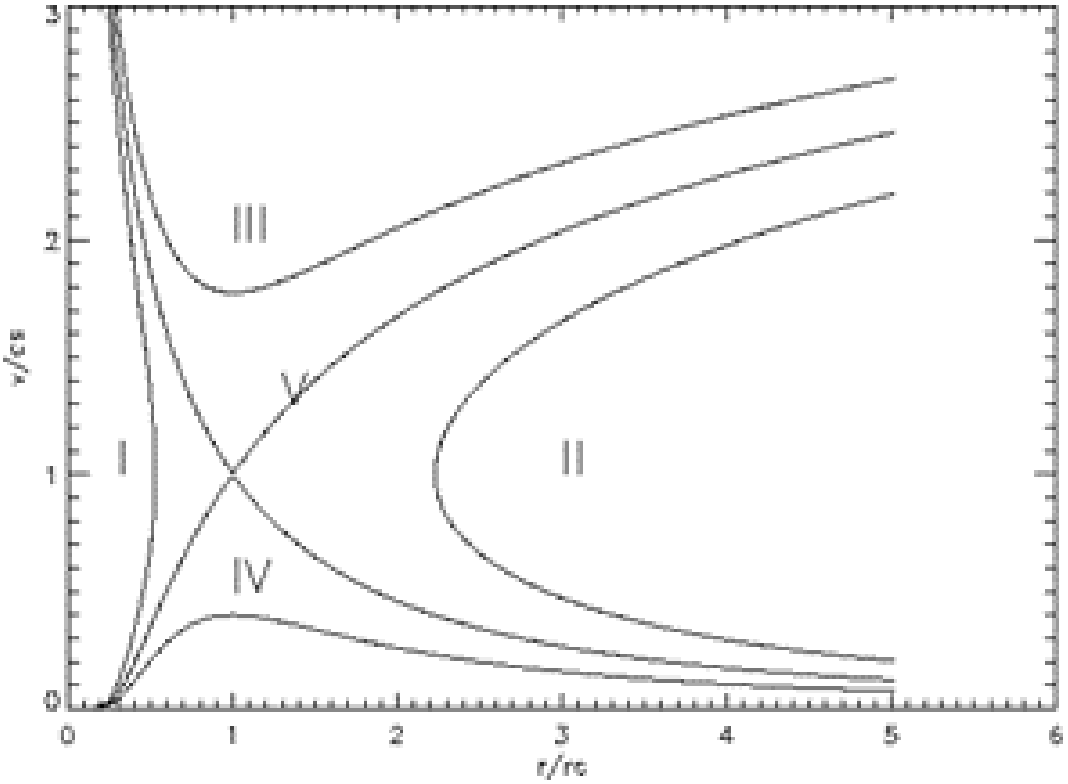

Figure 2.6: The topology of all the different solutions to Parker's hydrodynamic corona model.The solar wind speed with distance. The critical point is defined at (1,1). This Figure was taken from Parker (1958).

creases in speed with radial distance until at the critical radius, where the flow speed changes from a subsonic to a supersonic flow regime. Parkers Solution V is a good approximation to the observed solar wind, but it is far from perfect. Parker's solutions have assumed isothermal conditions and that the pressure is isotropic, which may be valid when closer to the Sun where collisions play a role, but as mentioned above collisions in the solar wind are rare as we move further out, which influences the parallel and perpendicular plasma pressure along the magnetic field. Nevertheless, with all these assumptions, the general behaviour of a slow solar wind is captured well by the model. The one major limitation of the Parker model is that it is purely hydrodynamic and does not explain the fast-solar wind with the observations. Electromagnetic forces are ignored and are not considered directly in the momentum calculation. As discussed above, electromagnetic fields play a vital role in plasma dynamics. Parker and Chapman models fail to address the question of solar heating and heat transport mechanisms. One of the main drawback of the hy-

drodynamic model is the assumption that the plasma is fully collisional. Under this assumption, the solar wind electrons distribution takes the form of a Maxwellian. However observations have shows deviation from thermodynamic equilibrium and limited validity of these assumptions.

2.4 Exospheric Models

Exospheric models are a type of kinetic model that has been postulated to explain the outflow and acceleration of the solar wind (Jockers, 1970; Lemaire and Scherer, 1971; Maksimovic et al., 1997). This model type assumes that the plasma is fully collisionless above a certain altitude above the corona, called the exobase (Lemaire and Scherer, 1971; Maksimovic et al., 2001). The exobase location is defined as the point above the corona where the collisional mean free path of the thermal particles, λ_c, is equal to the atmospheric density scale height of the coronal plasma, H. This can be formally represented by the Knudsen number, K_n = 1, where:

$$K_n = \frac{\lambda_c}{H} \tag{2.2}$$

H is defined by:

$$H = \frac{k_b T}{m_p g} \tag{2.3}$$

where g is the gravity of the Sun, m_p is the mass of protons, and k_b is the Boltzmann constant. The typical location of the exobase varies from 2 to 10 solar radii, depending on the density and temperature profiles adopted for the corona (Jockers, 1970). Above the exobase, in the absence of collisions, the trajectory of a charged particle can be determined by the first adiabatic invariant and the conservation of the total energy, E:

$$E = \frac{mv^2}{2} + m\phi_g + q\phi_e = constant \tag{2.4}$$

where m is the mass of the particle, ϕ_g is the interplanetary gravitational potential, ϕ_e is the interplanetary electric potential and q is the electric charge.

2.4.1 Ambipolar electric field

For particles to escape the corona above a height, r_0, they need to have a velocity greater than the Sun's escape velocity, V_{Escape}:

$$V_{Escape} = \sqrt{\frac{2GM}{r_0}} \tag{2.5}$$

where G is the gravitational constant and M is the mass of the Sun. From Equation (2.5), we can determine that the velocity needed to escape the Sun's gravitational potential is $\approx 618\ km\ s^{-1}$. Assuming the temperature of electrons and protons are both 1×10^6 K at the corona, the associated thermal speed of the electrons is $\approx 5507\ km\ s^{-1}$ and the thermal speed of protons is $\approx 128\ km\ s^{-1}$. Thus, for hot coronal plasma, the electrons can escape, but the protons are bound by the Sun's gravity (Jockers, 1970; Lemaire and Scherer, 1971; Maksimovic et al., 2001). This gives a rise to a global electric field, as the plasma will react to maintain quasi neutrality, which is called the ambipolar electric field. To maintain quasi neutrality, this electric field decelerates the escaping electrons and accelerates the protons from the corona into the interplanetary space, where they may reach supersonic velocity (Chamberlain, 1960; Lemaire and Scherer, 1971; Parker, 2010).

As calculated above, electrons can easily overcome the gravitational potential, but for the particles to escape to infinity they must also overcome the ambipolar potential field (Maksimovic et al., 2001). Assuming the potential and the solar wind density are zero at infinity, and substituting this into Equation (2.4), the minimum ambipolar escape velocity also commonly referred to as the cut-off velocity, V_ϕ, needed at the exobase is :

$$V_\phi = \sqrt{-2\phi_g - \frac{2q\phi_e}{m}} \tag{2.6}$$

From the cut-off velocity, we can calculate the electric potential difference ,Φ_e, between the exobase and infinity as follows (Berčič et al., 2021):

$$\Phi_e = \frac{mV_\phi^2}{2q} \tag{2.7}$$

2.4.2 Evolution of the VDF

In exospheric models, it is assumed that the energy and the first adiabatic invariant are conserved. For a given VDF at the exobase, the evolution of the VDF through the heliosphere can be traced by applying the Liouville's theorem (Lemaire and Scherer, 1971). Assuming there are no particles coming from infinity, exospheric models then yield three particle trajectory types above the exobase (Chamberlain, 1960; Jockers, 1970):

1. **Ballistic particles**: Particles that do not have sufficient energy to escape the interplanetary potential well and fall back towards the Sun.

2. **Trapped particles**: Particles that are trapped between a magnetic mirror point and an interplanetary potential well turning point.

3. **Escaping Particles**: Particles that have sufficiently large velocities to escape the interplanetary potential well and form the outgoing solar wind. The escaping particles for the electrons are often considered to be the strahl population, while all protons escape.

Figure 2.7 shows the evolution , under exospheric theory, for protons and electrons, at the exobase (Panel A), at 1 au (Panel B) and at infinity (Panel C) along the radial direction. The logarithm of the electron and proton VDF is plotted against energy, E, multiplied by the sign of the velocity. The positive direction along the x-axis indicates away from the Sun, and the negative direction indicates towards the Sun. In this format, the Maxwellian distribution is represented by the solid lines and the κ distribution is represented by the dashed lines.The protons are described by a Maxwellian distribution and two test distribution functions for the electrons: a Maxwellian and a κ distribution at the exobase. The truncation in the distribution in the sunward direction in the eVDF shown by $-e\Phi_{E0}$ and $-e\Phi_{E1AU}$ represents the energy cut off due to V_ϕ at the given distance. This truncation is called the electron deficit, which arises due to the lack of electrons that escape the ambipolar electric potential well (Maksimovic et al., 2001; Berčič et al., 2020).

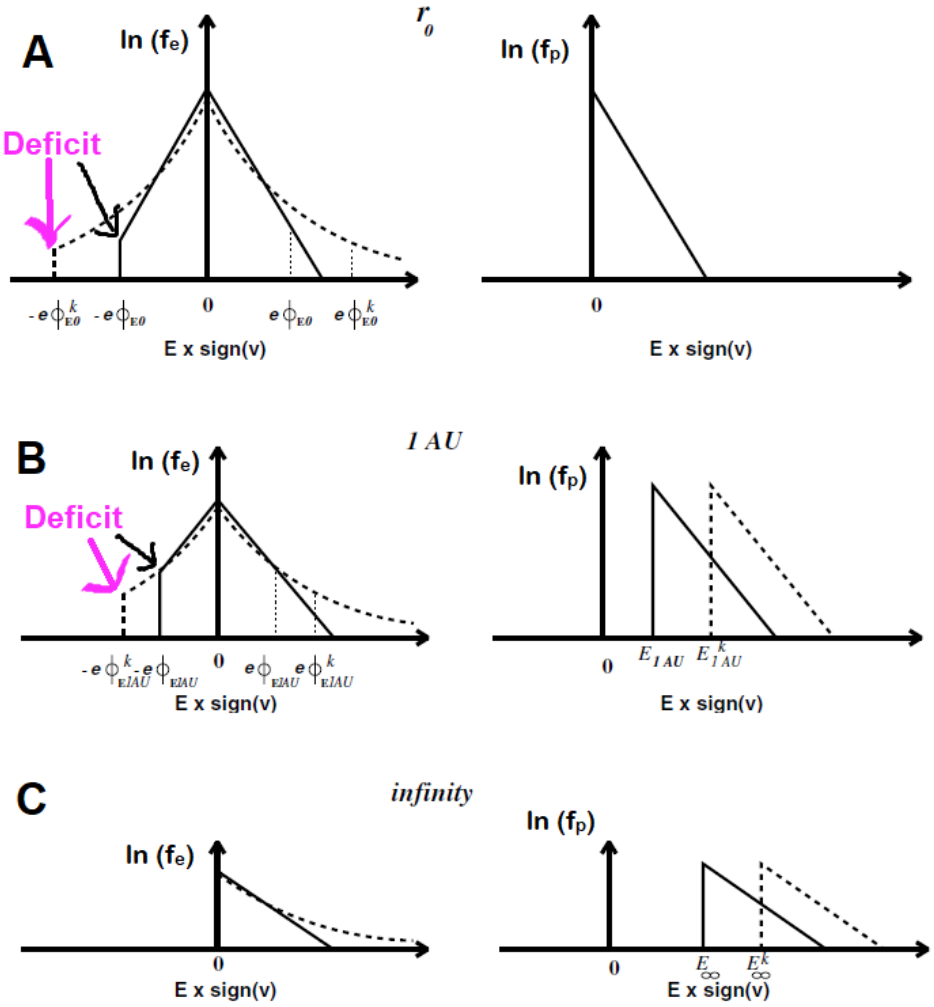

Figure 2.7: Radial evolution of the velocity distribution function at the exobase (r_0) (Panel A), 1 au (Panel B) and infinity (Panel C). The solid lines represent a Maxwellian distribution and the dotted lines represents a κ distribution. The x-axis is the energy, with the sunward direction represented by the negative x-axis. The y-axis on the left panels represents ln(fe) and the right panel ln(fp) where fe is the electron distribution function and fp is the proton distribution function. The pink arrow represents the location of the deficit cut off location of the κ distribution, and the black arrow of the deficit cut off location of the Maxwellian distribution. This Figure is adapted from Maksimovic et al. (2001).

2.4.2.1 VDF at exobase

Panel A in Figure 2.7 shows the VDF of the electrons (left-hand side) and protons (right-hand side) at the exobase. For the electron population, the energy associated with the ambipolar electric field is represented by $-e\Phi_{E0}$ and $-e\Phi^{k}_{E0}$ for the Maxwellian and κ distribution, respectively. There are no incoming particles from infinity, therefore there are no particles moving towards the Sun with energy less than $-e\Phi_{E0}$ and $-e\Phi^{k}_{E0}$ for the Maxwellian and κ distribution respectively. The electron population within $-e\Phi_{E0}$ and $e\Phi_{E0}$ for a Maxwellian distribution and $-e\Phi^{k}_{E0}$ and $e\Phi^{k}_{E0}$ for the κ distribution, represents the ballistic and trapped particles. All electrons with energy greater than $e\Phi_{E0}$ and $e\Phi^{k}_{E0}$ for the Maxwellian and κ distribution respectively form the escaping particles.

As described above, the outflow of the solar wind arises from the ambipolar electric field established by the electron pressure gradient, which accelerates the protons from the corona to satisfy equal electron and proton fluxes to ensure quasi-neutrality in the plasma. This means there is only one proton population in the exobase and all protons escape from the Sun with energy > 0.

2.4.2.2 VDF at 1 au

Panel B in Figure 2.7 show the VDF of the electrons (left-hand side) and protons (right-hand side) at 1 au. Since ballistic or trapped electrons are reflected towards the Sun due to the electrostatic potential barrier, only electrons with energy greater than the electrostatic potential between 1 au and the exobase reach 1 au from the exobase. These are bounded in energy by $-e\Phi_{E1AU}$ and $e\Phi_{E1AU}$ for a Maxwellian and $-e\Phi^{k}_{E1AU}$ and $e\Phi^{k}_{E1AU}$ for the κ distribution. Also, all the escaping electrons from the exobase reach 1 au. All electrons with energy greater than $e\Phi_{E1AU}$ and $e\Phi^{k}_{E1AU}$, for the Maxwellian and κ distribution respectively, form the escaping particles.

All escaping protons from the exobase are also seen at 1 au. As the protons are accelerated by the electron thermal pressure gradient, the protons have a minimum energy of E_{1AU} and E^{k}_{1AU} for a Maxwellian and κ electron VDF respectively.

2.4.2.3 VDF at infinity

Panel C in Figure 2.7 show the VDF of the electrons (left-hand side) and protons (right-hand side) at infinity. At infinity the electrostatic potential reaches 0 and therefore only escaping protons and electrons are present. The proton distribution is very similar to the VDF at 1 au, but the minimum energy of the protons has increased to E_∞ and E_∞^k for a Maxwellian and κ electron VDF respectively.

2.4.3 eVDF at the exobase

The overall evolution of the eVDF from exobase to infinity for a Maxwellian and a κ distribution at exobase is the same as described above (Maksimovic et al., 2001). The main difference between the two is that the κ distributions have a larger electron energy cut off and also are associated with larger minimum energy for the protons at 1 au and infinity compared to the Maxwellian distribution. The primary reason for this is that the tails of the κ distribution provide larger $f(v)$ at higher energies. This means that to ensure global quasi-neutrality, the zero current condition needs to be satisfied giving rise a stronger electric potential, which in turn accelerates the protons to a larger bulk velocity than for the Maxwellian electron distribution at the exobase (Maksimovic et al., 2005; Scudder, 1992; Maksimovic et al., 1997; Zouganelis et al., 2004).

Figure 2.8 shows the influence of using a Maxwellian and κ VDF at the exobase on the number density, electric potential, bulk speed and the total potential for protons (Lamy et al., 2003). The thin line represents the evolution of a κ distribution with a κ = 3 and the dashed line represents the Maxwellian distribution at the exobase. The exobase location for both scenarios is fixed at 6 solar radii (r_s) with the same coronal temperature of 1.5×10^6 K. Assuming a κ distribution or a Maxwellian distribution function at the exobase has negligible effect on the number density of the solar wind. However, assuming a κ distribution in the exosphere leads to larger electric potential than the Maxwellian, as explained above (Lamy et al., 2003; Maksimovic et al., 2005; Maksimovic et al., 1997; Marsch, 2006). It can be seen that with a κ distribution, the solar wind bulk velocity can be accelerated to over 400 $km\ s^{-1}$. Conversely, a Maxwellian distribution can only achieve a

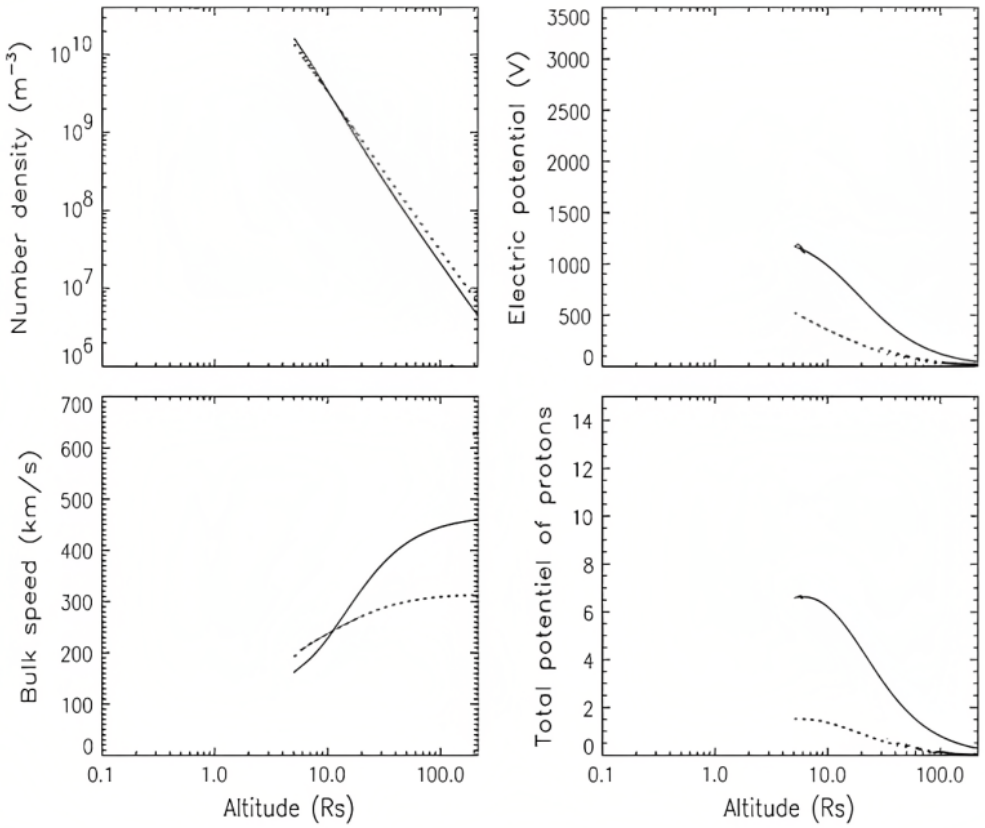

Figure 2.8: Results of an exospheric model for the density (upper left panel), electric potential (upper right panel), bulk velocity (lower left panel), and total potential (lower right) for solar protons from the model. The dotted curves refer to a exospheric model based on a Maxwellian VDF at the exobase which is set at 6 solar radii; the thin solid curves correspond to an exospheric model for which the exobase is at the same altitude but for which the electron and proton VDFs are kappa functions. The thick solid line corresponds to an exospheric model whose VDFs are also kappa functions but for which the exobase altitude is at 0.2 solar radii, i.e. below the altitude where the total potential energy of the protons has its maximum value. In all the three models, the coronal temperature of electrons and protons is the same. This Figure is adapted from Lamy et al. (2003)

maximum solar wind bulk velocity of 300 $km\ s^{-1}$. This highlights that the nature and evolution of the solar wind electron distribution can have a significant influence on the acceleration profiles of the solar wind.

2.4.4 Observations of the ambipolar electric field

The ambipolar electric field is fundamental in exospheric models to explain solar wind acceleration that arises from the electron thermal pressure gradient (Jockers, 1970; Lemaire and Scherer, 1971; Maksimovic et al., 1997, 2001; Zouganelis et al., 2004). The electron deficit derived from theory is shown in Figure 2.7 as a sharp cut-off in the sunward direction. Recent observations by Parker Solar Probe and Solar Orbiter show that the electron deficit signature is more complex than predicted in this theory, and the signature of the local deficit is more prevalent in the inner heliosphere than the outer heliosphere (Halekas et al., 2021; Owen et al., 2022; Berčič et al., 2020, 2021). The electron deficit is observed in almost 80 % of the data below 0.2 au (Halekas et al., 2021) and less than 5% past 0.4 au (Owen et al., 2022). Thus, the complex shape of the deficit and the overall eVDF suggests that the distribution is heavily processed (Halekas et al., 2020; Scudder and Olbert, 1979; Berčič et al., 2021; Gary et al., 1975; Saito and Gary, 2007; Verscharen et al., 2019; Verscharen et al., 2022). The ubiquitous nature of the electron deficit below 0.2 au indicates that the functional form commonly used to describe needs to be reconsidered, which could lead to more accurate solar wind models (Marsch, 2006). However, the nature of the observed deficit signature is still poorly understood and calls for more detailed study to model the electron deficit signature in phase space to recover the structure of the ambipolar electric potential. In Chapter 6, we aim to address this by modelling the deficit. Understanding the shape of the deficit can help us uncover the mechanisms for solar wind acceleration and its implication on the evolution of the solar wind electrons (Jockers, 1970; Maksimovic et al., 2001; Berčič et al., 2020, 2021; Halekas et al., 2020; Halekas et al., 2021). Furthermore, the difference in the shape and nature of the eVDF in the observations and the exospheric models could be attributed to the fact that exospheric models ignore collisions and other wave-particle interactions (Berčič et al., 2021; Verscharen et al., 2022).Furthermore,

ions are observed to be always escaping from the corona in the plasma rest frame (Woodham et al., 2020). Although PSP distribution show a deficit like feature in the electron VDF there is no currently no observational evidence signature of the deficit in the protons.

Chapter 3

Instrumentation

In order to examine the evolution and characteristics of the solar wind electrons, we use in-situ observations from the NASA Parker Solar Probe (PSP) mission (Fox et al., 2016).

3.1 Preface

PSP was launched on 12^{th} August 2018 on a Delta IV Heavy rocket from Cape Canaveral, Florida and will achieve the closest perihelion distance of 9.86 r_s on 24^{th} December 2024, giving us unprecedented measurements of the near Sun solar wind (Fox et al., 2016). In this Chapter, we describe the working principles of instruments used and measurements obtained from PSP to produce and analyse the data in Chapter 4, 5 and 6. The work presented in this thesis uses observations over four perihelion passes or "encounters": encounter 2 (30 th March 2019 – 10^{th} April 2019), encounter 3 (16^{th} August 2019 – 20 th September 2019), encounter 4 (24 th January 2020 – 4 th February 2020), and encounter 5 (20 th May 2020– 15 th June 2020). Encounter 1 was discarded due to instrumentation operation issues, which made the measurements non-viable for our scientific analysis. PSP is composed of four instrument suites: FIELDS (measures the electric and magnetic fields), SWEAP (measures the solar wind plasma), ISIS (measures the energetic particles) and WISPR (images the Sun's corona and inner heliosphere), as shown in Figure 3.1. The working principle of an electrostatic analyser (ESA) will be discussed in Section 3.2 of this Chapter, followed by a detailed description of the

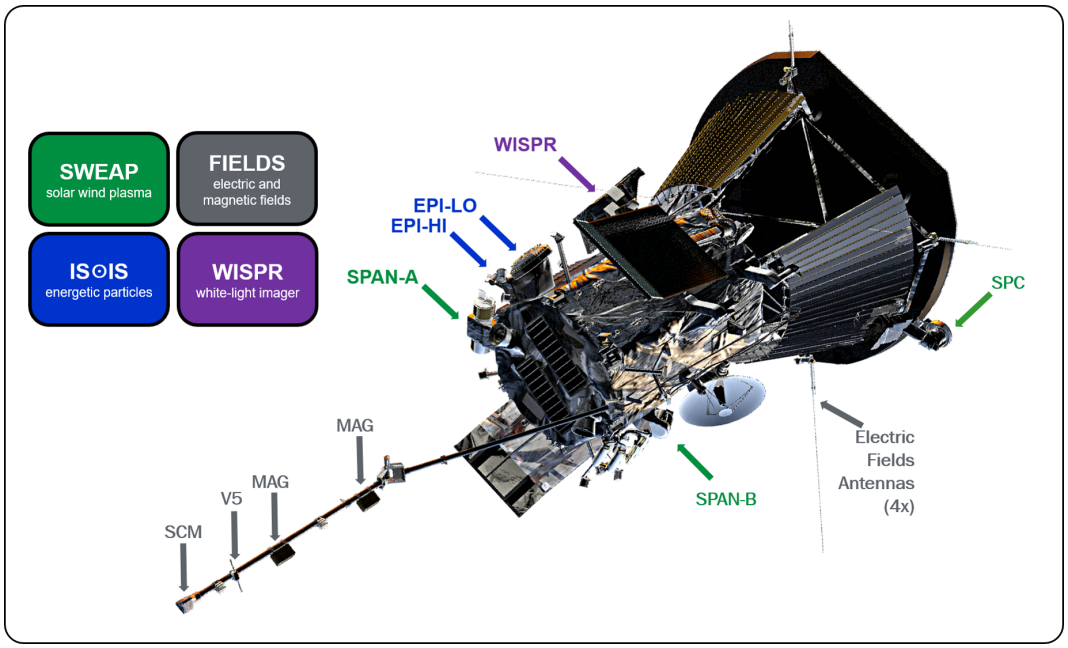

Figure 3.1: This figure illustrates the location of the various scientific instrument payload onboard PSP. PSP has four instrument suites: SWEAP (green), FIELDS (grey), ISIS (blue) and WISPR (purple).This Figure is taken from : `http://sweap.cfa.harvard.edu/PSP_Spacecraft.html`

electron ESA's from the SWEAP instrument suite, which we utilise to obtain the eVDF needed for the research presented in Chapters 4 and 6. Finally, in Section 3.3 of this Chapter, we discuss the working principle of a fluxgate magnetometer, followed by a description of the fluxgate magnetometer from the FIELDS instrument suite, which we utilised to obtain the magnetic field measurements needed for the research presented in Chapters 4 and 5.

3.2 Electrostatic Analysers (ESA)

ESAs are used to measure ions and electrons for a given energy interval, given time interval and a given direction. In this Section, we will explain the working principle of a typical top hat ESA. Figure 3.2 shows a simplified cross-section of a typical top hat ESA. The ESA is composed of two collimators called upper and lower collimator; two concentric nested curved surfaces called the upper hemisphere and lower hemisphere; an aperture at the apex of the outer hemisphere; a micro channel plate (MCP); and an anode board. Particles enter the instrument through the aperture of the collimator and are focussed and guided to the hemisphere via the aperture at the

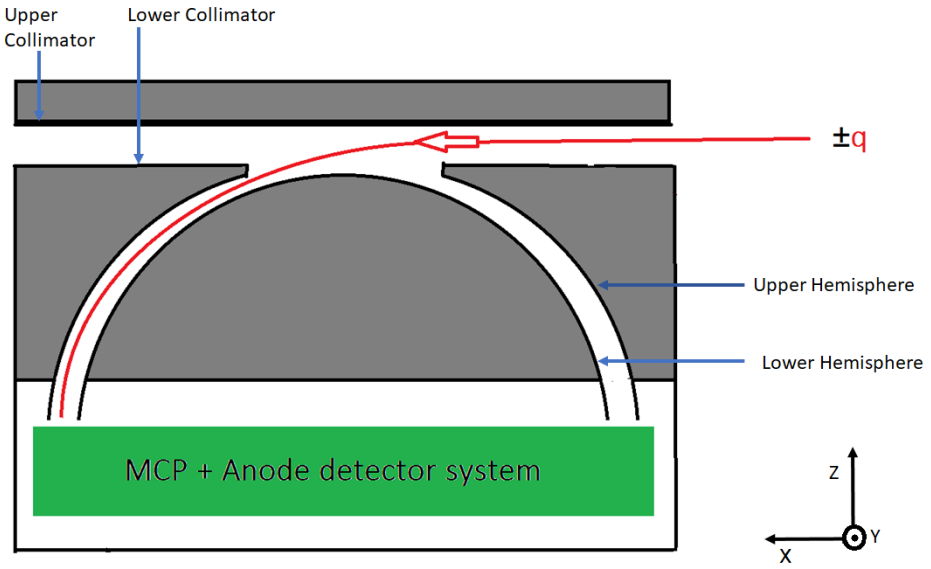

Figure 3.2: A cross-sectional view of a typical top hat ESA. Elevation is defined as the angle formed with the x-y plane. The azimuth is defined as the angle formed between the x and y-axis. The red curve with arrow represents the path of a successful particle with charge q through the instrument. The ESA is composed of an upper and lower collimator through which the particles enter the instrument. The nested concentric hemispheres are composed of an upper hemisphere and a lower hemisphere. The hemispheres are biased to select a specific energy per charge of the incoming particles. The green box represents the MCP + anode system. The ESA is often built in cylindrical symmetry around the z-axis.

apex of the outer hemisphere. The aperture of the collimator takes in electrons from 360° in the azimuth direction and a fixed elevation angle. The typical elevation acceptance angle of an ESA collimator aperture is 5°-15° (Carlson et al., 1982), The azimuth is defined as the angle in the x-y plane and elevations defined as the angle formed with the x-y plane. An electric field is set up between the hemispheres by positively biasing one of the hemispheres with respect to the other, in order to allow particles of a selected an energy/charge to pass through the space between the hemispheres without impacting the walls, which is shown by the red curve in Figure 3.2. Adjusting the voltage bias between the surfaces allows the ESA to select particles from different energy per charge within a narrow energy interval. The width of the energy range is determined by the gap between the hemispheres. The smaller the gap, the smaller the width of the energy acceptance range, which in turn means better energy resolution (Carlson et al., 1982).

Once a particle successfully passes through the gap between the collimators and the hemispheres, it exits the hemisphere at an angle near normal to the surface of the MCP located underneath the hemispheres, as shown by Figure 3.2. An MCP is a resistive plate with perforations called channels. The channels are designed such that a single particle entering the system would strike the inside walls of the channel, starting a cascade of electrons through secondary emission. The MCP thus increases the original signal of a single electron by many orders of magnitude. The MCP is positively biased to accelerate the electrons through the plate and collected at the exit of the plate by an anode board. The anode board is composed of a series of metallic pads that collect the emerging particle charge clouds at the exit of the MCP and convert them into digital signals (Rosenbauer et al., 1977). The digital signals are fed into the digital board, which runs signal processing and calibration to obtain the scientific products. The separation between the metallic pads determine the azimuth resolution. A typical ESA has a fan beam field of view (FOV) due to the fixed narrow elevation range. To provide a 360° coverage of the elevation, a few strategies can be employed. The ESAs onboard Helios (Rosenbauer et al., 1977), Wind (Lin et al., 1995), and Cluster (Johnstone et al., 1988) utilised the spin of spacecraft to sweep the fan beam FOV through various elevations whilst ESAs onboard three-axis stabilised missions like Solar Orbiter (Owen et al., 2020), PSP (Whittlesey et al., 2020) and MAVEN (Halekas et al., 2015) adopted an electrostatic deflector system, discussed in Section 3.2.1, to draw in electrons from a wider elevation angle and also to scan through various elevations.

3.2.1 SWEAP

For this thesis, we use electron measurements from the Solar Wind Electrons Alphas and Proton Investigation (SWEAP) suite onboard PSP (Whittlesey et al., 2020). The SWEAP instrument suite uses ESAs to measures protons and electron VDFs but for our research we will be focussing on the 3D electron VDFs with the Solar Probe Analyzer—Electron (SPAN-E) sensors, consisting of two top-hat electrostatic analysers (ESAs): SPAN-A and SPAN-B. SPAN-A is located on the ram side and SPAN-B is located on the anti-ram side of the spacecraft as shown by Figure

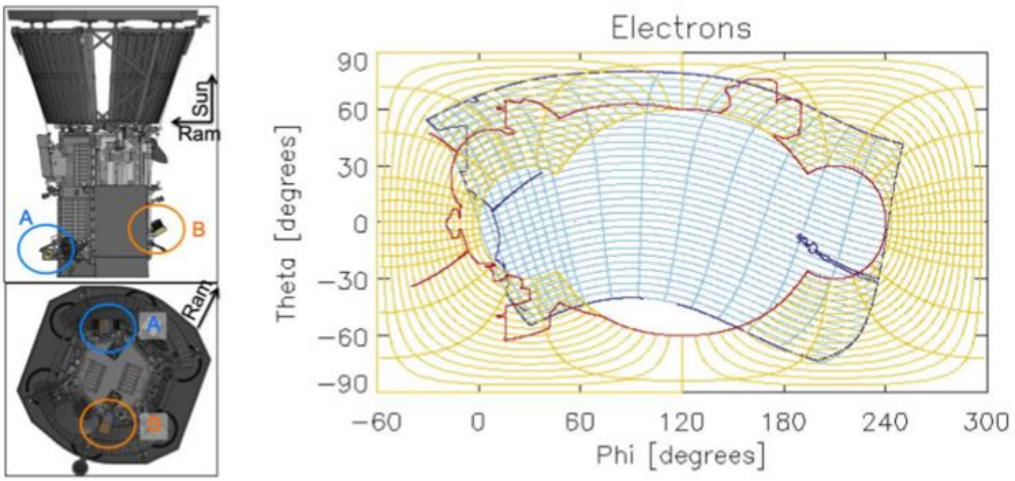

Figure 3.3: The picture on the left shows the location of SPAN-A and SPAN-B. SPAN-A is positioned on the ram side of the spacecraft, highlighted by a blue circle. SPAN-B is positioned on the anti-ram side of the spacecraft, highlighted by an orange circle. The picture on the right shows the FOV of SPAN-A and FOV of SPAN-B overlaid on the same sky map. The X axis is the azimuth and the y-axis are the elevation in degrees. The blue is the FOV of SPAN A and the orange trace is the FOV of SPAN B. The red line describes the actual FOV of SPAN B after accounting for intrusion caused by the spacecraft body. The darker blue trace is the actual FOV of SPAN A after accounting for intrusion caused by the spacecraft body. The lines of intrusion in the FOV are from the antenna and the instrument boom. The Sun is situated at (0,0). This Figure is taken from Whittlesey et al. (2020).

3.3. Together, the two ESAs measure electrons arriving from across almost the full sky, using orthogonally positioned 120° × 240° FOV, over an energy range from 2 to 1793 eV during the measurement intervals. The FOV of SPAN-A and SPAN-B on a full sky map is shown in Figure 3.3. The Parker Solar Probe instrument frame is oriented in such a way that its Z axis is along the normal to the heat shield i.e. pointing to the Sun, its X axis points in the RAM direction of the spacecraft and the Y axis points toward ecliptic south. Each ESA scans through 16 azimuths, 8 elevations and 32 energy bins.

A graphical cross-section of the SPAN-E optics is shown by Figure 3.4. As discussed above, the elevation acceptance angle width of an ESA ranges from 5° to 15°. To enhance this field of view, a deflector system composed of curved plates is added to the entrance of the collimator, as shown in green in Figure 3.4. The individual deflector plates are positively biased to draw in electrons from wider FOV

with elevation to angle increased to +/- 60° (Kasper et al., 2016; Whittlesey et al., 2020). Adjusting the bias on the deflector plates changes the elevation direction of the incoming particle into the instrument. The elevation resolution for each sensor is composed of eight $\sim 15°$ steps and covers a total of 120° (Whittlesey et al., 2020).

As PSP moves to the inner heliosphere, it is expected to measure particle fluxes a few orders of magnitude greater than typically observed at 1 au. This poses an increased risk of saturation to the instrument. To account for this, SPAN-E employs two methods of attenuation: spoiler mode and a mechanical attenuator plate. The spoiler mode is achieved in the design by splitting the outer hemisphere into two parts, called the upper outer hemisphere (blue) and lower outer hemisphere (yellow) as shown by Figure 3.4. The upper outer hemisphere is held at ground at all times and operates as a normal ESA as described in Section 3.2. The lower part of the outer hemisphere is called the spoiler and can be held at ground or swept up to 80 V in cadence with the inner hemisphere (purple) which is positively biased. When the spoiler is held at ground the instrument works as a normal ESA, as described above, but when the spoiler is biased it will effectively decrease the energy resolution and thereby reduce the total number of particles permitted through the hemispheric space between the lower outer hemisphere and the spoiler to reach the MCP (Whittlesey et al., 2020). The level of attenuation depends on the ratio between the spoiler and the inner hemisphere voltage.

Another design consideration made for PSP was to employ a mechanical attenuator. This consists of a series of slits on a thin metal piece which can be deployed at the instrument aperture when the particle's number flux exceeds the sensor saturation threshold (Kasper et al., 2016). When the mechanical attenuator is engaged, it reduces the total instrument particle flux by a factor of 10 (Whittlesey et al., 2020). This correction factor is accounted for on ground before the data is publicly released.

Each ESA, SPAN A and B, contains a dedicated electronics package consisting of an anode board to measure electron counts, a digital board which processes the counts into science data, a high voltage power supply (HVPS) to power the de-

flectors, spoiler and hemispheres, a low voltage power supply (LVPS) to power the boards and an additional board, called the backpane, to act as a bridge between the HVPS and LVPS (Kasper et al., 2016). The backpane board also acts as a switch to enable/restrict the power supply for the attenuator, hemispheres, and deflectors.

The anode boards of SPAN-A and SPAN-B are electrically identically except for the spacing of the pads and size of the anode to facilitate the variation in azimuth resolution. The azimuth resolution of each sensor is composed of eight 6° and eight 24° sectors, depending on the look direction, and covers a total of 240°. The digital board controls the communication flow between the instrument and the central data processing unit of SWEAP called SWEAP Electronics Module (SWEM). The digital board also processes the anode board signals into counts and sends this data packet to the SWEM for storage on board. For most of the operation, the digital board of SPAN-A and SPAN-B are run identically, apart from when the spacecraft location is outside 0.7 au, when SPAN-B can be pointed directly at the Sun. The digital board also contains a field programmable gate array (FPGA) which synchronises the acquisition measurement of the respective ESAs.

The HVPS board provides the power of the deflectors (0 - 4kV), spoiler (0 - 80V) and hemispheres (0 - 2kV). The voltage settings are sent from the digital board to the HVPS via a digital-to-analog converter (DAC) chip. The LVPS generates the low voltages, 1.5 - 8 V, needed to run the boards. The backpane board acts as a bridge between the digital, HVPS and LVPS and also acts as a fail-safe to control the mechanical attenuator from actuating erroneously and corrupting the science data.

The in-orbit operation of PSP is split into two phases: encounter and cruise. The encounter phase is centred around each PSP perihelion and lasts about 15 days, with distance less than 0.4 au. During this phase, the instrument collects nominal science data with an integration time of 13.98 seconds. The cruise phase is defined as the rest of the orbit, during which the science data rates are lower, with a cadence of 895 seconds. The cruise phase data taking is also interrupted by spacecraft communications, power limitations and other spacecraft critical operations. For the

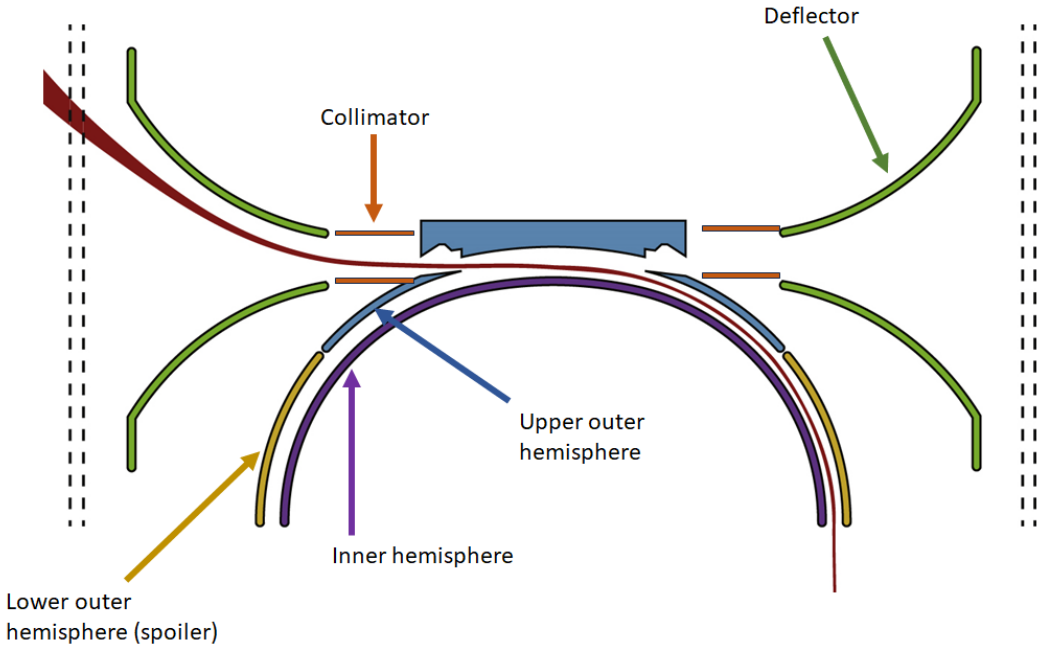

Figure 3.4: The graphical cross-section of SPAN-E. The green curves represent the deflectors, the orange represents the collimators, the blue curve represents the upper part of the outer hemisphere, the yellow is the lower outer hemisphere, the purple curve is the inner hemisphere and the red curve represents the trajectory path of a successful electron through the ESA. This Figure is adapted from (Whittlesey et al., 2020)

work presented in this thesis, we only utilise data taken during the encounter periods.

For this thesis, we use the level 3 data product. The SWEAP level 3 data product is provided in differential energy flux (DEF) as a function of pitch angle and energy. In Chapter 4, we discuss how this differential energy flux is converted into distribution function. The level 3 data product uses the magnetic field measurements from the Fluxgate magnetometer on board to produce the pitch angle associated with each measurement pixel.

3.3 Fluxgate magnetometer

Fluxgate magnetometers are used to measure the magnetic field in space plasmas (Aschenbrenner, 1936; Ness, 1970). A fluxgate sensor typically consists of a magnetically permeable ring core which is wrapped by two coil windings, called a drive winding and a sense winding. A fluxgate magnetometer relies on the magnetic hys-

teresis of the permeable ring core. An idealised hysteresis curve is shown by the figure in the centre left of Figure 3.5, which shows the variation in the magnetic field of the core when an auxiliary field, H, is applied to the core. When an alternating current is passed through the drive winding, it produces an auxiliary field as shown by the top left-hand plot in Figure 3.5 with an amplitude H_0 and a time period Π. The total core's magnetic field is the combination of the nonlinear response of the core's hysteresis and the auxiliary field, as shown by the centre right plot in Figure 3.5. The magnitude of H must be large enough for the core to experience negative and positive saturation during each cycle of $H_d(t)$.

The sense coil measures voltage induced by the total core's magnetic field, B(t). As the core experiences the same amount of positive and negative saturation from the hysteresis, the voltage periodicity in the sense winding and the driving winding will be the same. When an external field is applied, there is an offset in the total auxiliary field, shown by ΔH_z in Figure 3.5. This offset causes the core's total magnetic field to experience different levels of positive and negative saturation for a given cycle of $H_d(t)$. This variation in saturation, represented by the variation in the width of the shading, gives rise to harmonics in the induced voltage in the sense winding. The magnitude of the external magnetic field is determined by the amplitude of the second harmonic of the drive winding frequency in the sense winding (Ness, 1970). A single fluxgate sensor can measure the strength of the magnetic field in one direction. Therefore, a flux gate magnetometer consists of three flux gate sensors placed orthogonal to each other to provide a 3D vector measurement of the magnetic field.

3.3.1 FIELDS

For this thesis, we use the magnetic field measurements produced by the fluxgate magnetometer (MAG) from the FIELDS suite onboard PSP (Bale et al., 2016). MAG is mounted on a 3 m boom to reduce contamination of spacecraft generated magnetic field. We use the level 2 data product which is sampled at 292 Hz over the measurement range $\pm$65536 nT (Malaspina et al., 2016; Bale et al., 2016). The data are then down sampled to match the integration time of SWEAP and provided

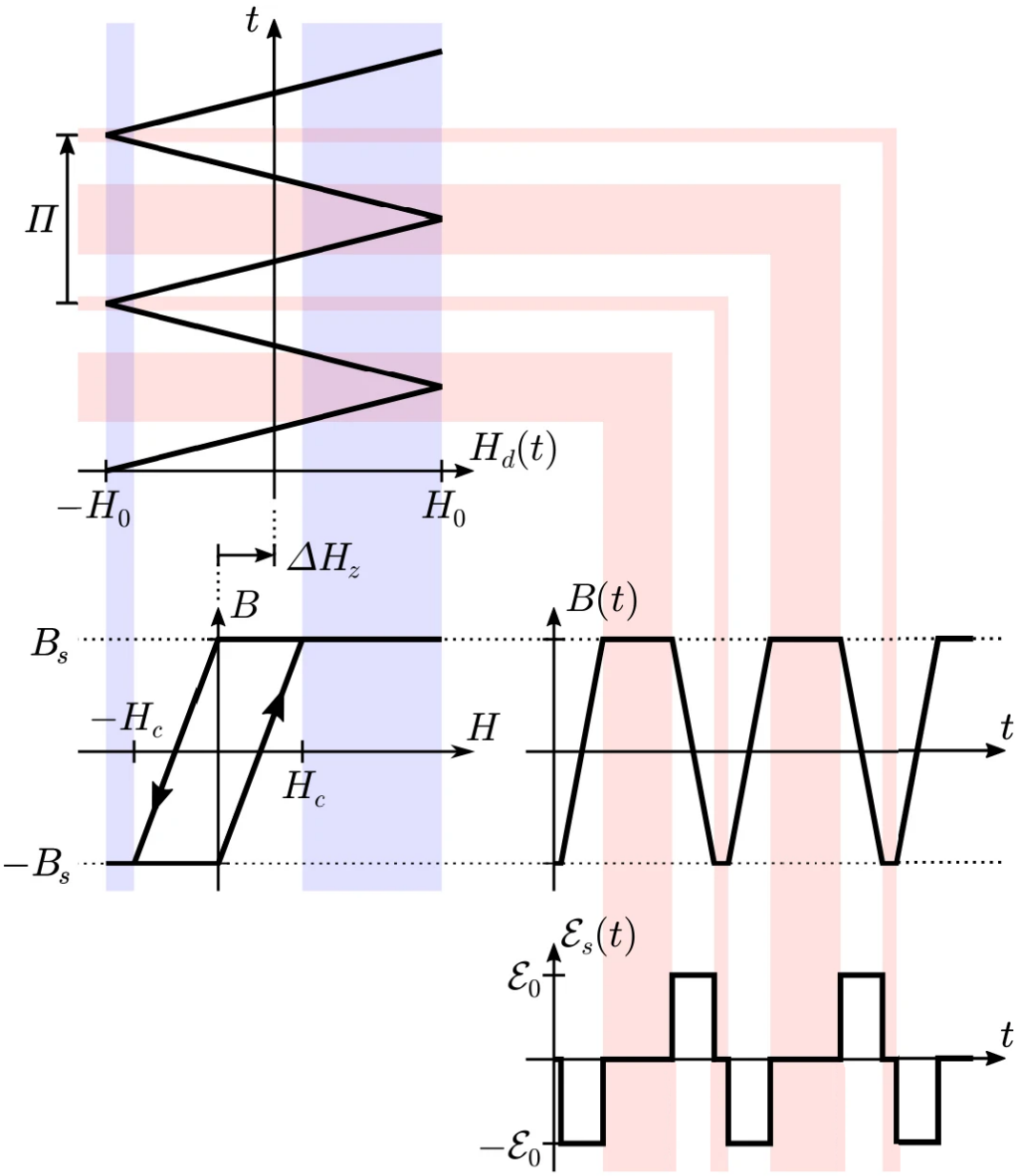

Figure 3.5: The basic working principle of an idealised fluxgate sensor. The centre left plot shows an idealised hysteresis loop of a fluxgate sensors core. The x-axis represents the auxiliary field applied to the core and the y-axis represents the magnetic field of the core. The H_c represents the value of auxiliary field which saturates the core at B_s. The upper left-hand plot shows the variation of the auxiliary field H varying with time, t. The ΔH_z represents the offset caused by the external field H_z. Π represents the time period of the signal. The centre right plot shows the core's magnetic field which is limited by the saturation values B_s in the hysteresis plot. The lower right plot shows the induced voltage ε_s in the sense winding from B(t). The H values for which the core is saturated are indicated by light-blue shading, and the times when this occurs are indicated by light-red shading. This Figure is adapted from Verscharen et al. (2019)

in the SWEAP level 3 data in the Radial-Tangential-Normal (RTN) frame, where Radial (R) is the vector that points along the sun-spacecraft line, Tangential (T) is the cross product of the solar rotation axis with the Radial vector and Normal (N) completes the direct orthogonal frame line(Whittlesey et al., 2020).

Chapter 4

Radial Evolution of Thermal and Suprathermal Electron Populations in the Slow Solar Wind from 0.13 to 0.5 au: Parker Solar Probe Observations

4.1 Preface

This Chapter describes methodology, results, discussion and conclusions that have also been published in the Astrophysical Journal (Abraham et al., 2022a). Under the supervision of Professor Christopher J. Owen and Dr. Daniel Verscharen, this work was carried out in collaboration with Dr. Mayur Bakrania who developed the algorithms underpinning the machine learning aspect of the work. Dr. Phyllis Whittlesey provided the SWEAP data and also provided instrument parameters needed to estimate the geometric uncertainties which are important for this work. Dr. David Stansby provided the proton data needed for this work.

4.2 Introduction

In Chapter 2, we showed that on average, the evolution of the solar wind electron core density, n_c, with radial distance, r, is in excellent agreement with expectations for an isotropically expanding gas, for which $n \propto r^{-2}$. In contrast, the halo and strahl populations show more complex density profiles than a steady radial expansion from 0.3 - 4 au (Maksimovic et al., 2005; Štverák et al., 2009). Under purely adiabatic conditions, the strahl population would continue to narrow in pitch angle as it propagates radially away from the Sun into regions of lower magnetic field strength, due to conservation of the magnetic moment. However, this is not generally observed, and the strahl appears to undergo significant pitch-angle scattering, as its width gradually increases with radial distance (Anderson et al., 2012; Hammond et al., 1996; Graham et al., 2017). In a simple model, Owens et al. (2008) examine the combined effects of adiabatic focusing and a constant rate of scattering on the electron populations. According to this model, a constant scattering rate dominates over the adiabatic focusing beyond ~ 0.1 au, and the strahl pitch-angle width thus increases with heliocentric distance. Moreover, the strahl parallel temperature does not vary with radial distance close to the Sun (Berčič et al., 2020), which supports the assumption that the strahl carries information about the coronal temperature. However, the exact physics of the origin of the strahl is still unclear.

The origin of the radial evolution of the halo parameters remains elusive, although beam instabilities and resonant wave-particle interactions are potential mechanisms for the scattering of strahl electrons into the halo, while leaving the core relatively unaffected (Vocks et al., 2005; Saito and Gary, 2007). Alternatively, Coulomb collisions (Horaites et al., 2017) or background turbulence (Saito and Gary, 2007) can play similar roles in the evolution of the halo.

The solar wind near the Sun is more pristine, or less processed by transport related effects, which means that the electron distribution function is likely to be closer to the original distribution in the outer corona of the Sun. Comparing electron distributions at different distances from the Sun with those recorded very close to the Sun enables us to improve our understanding of processes which facilitate solar

wind acceleration and heating. At the same time, it allows us to probe the mechanisms that modify the distribution as the solar wind travels to greater heliocentric distances. In this Chapter, we present the evolution of macroscopic quantities such as the density and temperature of the thermal and suprathermal populations at heliocentric distances below 0.3 au, which has not been examined using data from missions launched prior to Parker Solar Probe.

4.3 Data handling

In this Chapter, we use SPAN electron (SPAN-E) level 3 pitch-angle data. The level 3 data are provided in 32 energy bins and in twelve pitch-angle bins of width 15° with bin centres ranging from 7.5 to 172.5°. In the production of the level 3 dataset, the measurements from both sensors (SPAN-A and SPAN-B) are re-sampled from their intrinsic resolution onto this pitch angle grid, which eliminates each instrument pixel one count effects. These level 3 data are provided in units of differential energy flux ($cm^{-2}\,s^{-1}\,str^{-1}\,eV^{-1}eV$).

In order to distinguish between solar-wind streams with different bulk speeds, we perform bi-Maxwellian fits to the proton core distribution function from the `spi_sf00_8dx32ex8a` data product, observed by Solar Probe Analyzer — Ions (SPAN-I) sensors, using the methodology described by Woodham et al. (2020), based on earlier routines developed by Stansby et al. (2018). Only the proton core speed is used from these fits in this work. The proton measurement cadence is higher than SPAN-E's and thus in this work the values are averaged over the SPAN-E integration times.

Parts of the electron distributions are missing due to spacecraft obstruction. To mitigate for this, we remove any VDFs for which more than 20% of the data are missing. The level 3 data are converted from differential energy flux to the phase space density through

$$f(v_{\parallel}, v_{\perp}) = \frac{m_e}{V^2} J(E, \alpha) \mathrm{d}A\, \mathrm{d}\Omega\, \mathrm{d}E\, \mathrm{d}t, \tag{4.1}$$

where f is the phase space density, V is the velocity J is the differential energy flux

(DEF), Ω is the solid angle, dt is the acquisition time per elevation and energy bin.

As PSP approaches the Sun, the UV radiation reaching the spacecraft surface generates increasing numbers of secondary electrons, which affect the lower energy bins. Halekas et al. (2020) account for these lower energy secondary electrons in their fitting model by assuming the secondary electrons have a Maxwellian distribution with a fixed temperature of 3.5 eV. As our data set spanned over 2 years, we have noted large variations in the nature of the secondary electrons. In our fitting procedure, to avoid the effects of secondary electrons especially during the encounters, we have thus ignored all data points associated with energies below 30 eV. This selection criterion makes core-temperature measurements below 30 eV less reliable than measurements at larger core temperatures.

4.4 Distribution fitting

Fitting techniques are widely used in solar and space plasma physics in order to derive plasma bulk parameters from observations (Halekas et al., 2020; Berčič et al., 2020; Nicolaou et al., 2020; Stansby et al., 2018; Štverák et al., 2009; Maksimovic et al., 2005). To capture the properties of the electrons, we analytically describe the anticipated distribution function and then fit to the measured data. Once fitted, we obtain parameters such as density, temperature, and bulk speed of each modelled population. A single, classical, collisional distribution model cannot be used to describe the overall electron distribution, as it fails to capture the non-Maxwellian features exhibited by the suprathermal electrons. Similar to Maksimovic et al. (2005), we fit the core electrons with a bi-Maxwellian function in the magnetic field aligned frame, while we fit a bi-κ function to the halo population. Once the core and halo were fitted, Maksimovic et al. (2005) subtracted the resulting core-halo distribution model from the observed distribution. They integrated the remaining population in velocity space to obtain macroscopic strahl properties. Štverák et al. (2009) performed a similar fitting routine, but modified it by fitting the suprathermal components with a truncated model, such that suprathermal components are restricted to the suprathermal parts of velocity space. Both studies show that the non-thermal

halo population is modelled well by a bi-κ and the core by a bi-Maxwellian, but Štverák et al. (2009) applied a different methodology, using a truncated κ-model to represent the strahl. This shows that closer to the Sun, the κ index of the strahl population approaches a value of 15, which provides a distribution that is close to a Maxwellian below 0.5 au. In our fit model, we employ machine learning techniques (Bakrania et al., 2020) to determine the break-point energies of the measured distribution and then use these in the fitting routine to constrain the fits, as described in Section 4.4.1. The breakpoint energy is defined as the energy at which the non-thermal structures deviate from the thermal Maxwellian distribution (Feldman et al., 1975; Marsch, 2006). We discuss the fitting routine in Section 4.4.2 and the error analysis in Section 4.4.3.

4.4.1 Determination of breakpoints through machine learning

As our fitting routine uses the breakpoint energy between the core and halo as an input, we employ the machine learning techniques described by Bakrania et al. (2020). These use unsupervised learning algorithms to determine these breakpoint energies. We also use these techniques to separate halo and strahl electrons in pitch angle and energy space. This technique uses the K-means clustering method (Arthur, 2007) from the `scikit-learn` library (Pedregosa et al., 2011). K-means clustering works by grouping a set of observations into K clusters, based on similarities between the observations. Unsupervised learning algorithms do not require the user to assign labels to training data, thereby reducing bias (Arthur, 2007). In our method, we manually set the number of clusters in the K-means algorithm to 2, which represents the core cluster and a suprathermal cluster. The algorithm calculates the breakpoint energy at a specific pitch angle by separating the energy distributions, at that pitch angle, into two clusters with the mid-point determined to be the breakpoint energy.

The K-means algorithm clusters these energy distributions by minimising the function:

$$\sum_{i=1}^{u} \sum_{j=1}^{K=2} \omega_{ij} \left\| x_i - \mu_j \right\|^2, \tag{4.2}$$

where

$$\mu_j = \frac{\sum_{i=1}^{u} \omega_{ij} x_i}{\sum_{i=1}^{u} \omega_{ij}}, \tag{4.3}$$

$$\omega_{ij} = \begin{cases} 1 & \text{if } x_i \text{ belongs to cluster } j \\ 0 & \text{otherwise,} \end{cases} \tag{4.4}$$

and u is the number of 3-tuples at the defined pitch angle. In Equation (4.2), x_i is defined as the vector representation of the differential energy flux (DEF) tuples, where the index i indicates tuples of three adjacent energy bins (i.e., energy distributions which range across three energy bins). The variable μ_j is the vector representation of two random DEF tuples, where the index j labels each cluster. The K-means algorithm calculates the breakpoint energy by: (1) randomly selecting two DEF vectors to become the central points, or 'centroids' of each cluster, μ_j, (2) allocating each DEF vector, x_i, to its nearest centroid, by finding the smallest least-square error between that vector and the centroids, (3) determining new centroids, μ_j, by averaging the DEF vectors assigned to each of the previous centroid, (4) re-allocating each DEF vector, x_i, to its new closest centroid, μ_j, and (5) repeating steps 3 and 4 until no more new re-allocations occur. After the algorithm has computed the two clusters, the breakpoint energy at the relevant pitch angle is calculated as the centre between the highest energy bin in the lower energy cluster (which represents the core), and the lowest energy bin in the higher energy cluster (which represents the suprathermal populations).

In order to distinguish between strahl and halo electrons, we apply this method to distributions both pitch angle and energy space. The method used for distinguishing between populations in pitch angle space is analogous to the method described above, with x_i now defining a pitch angle distribution at a certain energy. However the K-means algorithm is now finding the 'break' in pitch angle. A detailed description of this method and an analysis of its effectiveness is provided by Bakrania et al. (2020). Arthur (2007) details a comprehensive and more general account of the K-means algorithm.

After applying this method, the K-means algorithm outputs a list of pitch angle

bins, energy bins, and time-stamps which characterise the transition from core to suprathermal electrons. With these outputs we obtain a set of parameters, including times when a strahl is present, strahl energies, and widths, which we use to constrain our fitting analysis.

4.4.2 Fitting of the eVDF

We fit the observed electron distribution functions, f_i, to the sum, f_e, of three analytical expressions which separately describe each of the electron populations, namely the core, halo and strahl:

$$f_e = f_c + f_h + f_s, \tag{4.5}$$

where f_c is the fitted core, f_h is the fitted halo, f_s is the fitted strahl. Following on from previous work (Maksimovic et al., 2005; Štverák et al., 2009; Halekas et al., 2020; Berčič et al., 2020), the core electrons are modelled with a two-dimensional bi-Maxwellian distribution function:

$$f_c = \frac{N_c}{\pi^{3/2} V_{\parallel \omega c} V_{\perp \omega c}^2} \exp\left(-\frac{V_\parallel^2}{V_{\parallel \omega c}^2} - \frac{V_\perp^2}{V_{\perp \omega c}^2} \right), \tag{4.6}$$

where N_c is the core density, $V_{\parallel \omega c}$ is the core parallel thermal velocity, $V_{\perp \omega c}$ is the core perpendicular thermal velocity. For the halo population, we fit to a bi-κ function:

$$f_h = \frac{N_h}{V_{\parallel \omega h} V_{\perp \omega h}^2} \left(\frac{2}{\pi(2\kappa - 3)} \right)^{3/2} \frac{\Gamma(\kappa+1)}{\Gamma(\kappa - \frac{1}{2})} \left[1 + \frac{2}{2\kappa - 3} \left(\frac{V_\parallel^2}{V_{\parallel \omega h}^2} + \frac{V_\perp^2}{V_{\perp \omega h}^2} \right) \right]^{-(\kappa+1)}, \tag{4.7}$$

where N_h is the halo density, $V_{\parallel \omega h}$ is the halo parallel thermal velocity, $V_{\perp \omega h}$ is the halo perpendicular thermal velocity, and κ is the κ index. For the strahl component, we use a modification to the previous works cited above and fit to a bi-Maxwellian function drifting in the parallel direction at speed $U_{\parallel_s}$ with respect to the magnetic

field. Thus, the strahl is described by:

$$f_s = \frac{N_s}{\pi^{3/2} V_{\parallel_{\omega s}} V_{\perp^2_{\omega s}}} \exp\left(-\frac{(V_\parallel - U_{\parallel_s})^2}{V^2_{\parallel_{\omega s}}} - \frac{V^2_\perp}{V^2_{\perp \omega s}} \right), \tag{4.8}$$

where N_s is the strahl density, $V_{\parallel_{\omega s}}$ is the strahl parallel thermal velocity, $V_{\perp_{\omega s}}$ is the strahl perpendicular thermal velocity, and $U_{\parallel_s}$ is the strahl parallel bulk velocity.

As there are 11 free parameters involved in the fit (N_c, N_h, N_s, $V_{\parallel_{\omega c}}$, $V_{\perp_{\omega c}}$, $V_{\parallel_{\omega h}}$, $V_{\perp_{\omega h}}$, κ, $V_{\parallel_{\omega s}}$, $V_{\perp_{\omega s}}$, $U_{\parallel_s}$), we split our fitting process into two stages. This has the advantage of reducing the number of nonphysical fits which can arise due to the large number of degrees of freedom. The first stage is to fit only to the core + halo model before we fit to the strahl model. An example of the results of this stage are shown in the left panel of Figure 4.1, which presents the core and halo fits (blue and red lines respectively) to the data points from a single measured distribution (purple diamonds). In the second stage, we use the core-strahl breakpoint energy from our machine learning algorithm to constrain the relevant velocity space of the strahl electron population. This second fit captures the strahl using the drifting Maxwellian model, with the outputs of the first fit for the core and halo parameters and the strahl break point energy as fixed inputs to constrain the velocity space. The right panel of Figure 4.1 presents the results of this strahl fit (yellow line) for the example distribution, plotted on top of the core and halo fits and the data points from the left panel. The overall fit is shown as the green trace, and from visual inspection it can be seen that a reasonable overall fit is achieved.

The fits are performed using the Levenberg Marquardt fitting algorithm in log-space to capture the 2D electron distribution function in the field aligned velocity space, (Levenberg, 1944) with each point weighted with the errors described in Section 4.4.3. The free parameters are constrained as follows: core, halo and strahl density must be greater than 0; the strahl parallel bulk velocity must be less than $2.5 \times 10^7\,\mathrm{m\,s^{-1}}$, as this would be outside the instrument measurement range; and κ must be greater than 1.5 and less than 25. The machine learning algorithm will provide the times when there is a strahl present or not into the fitting routine, If

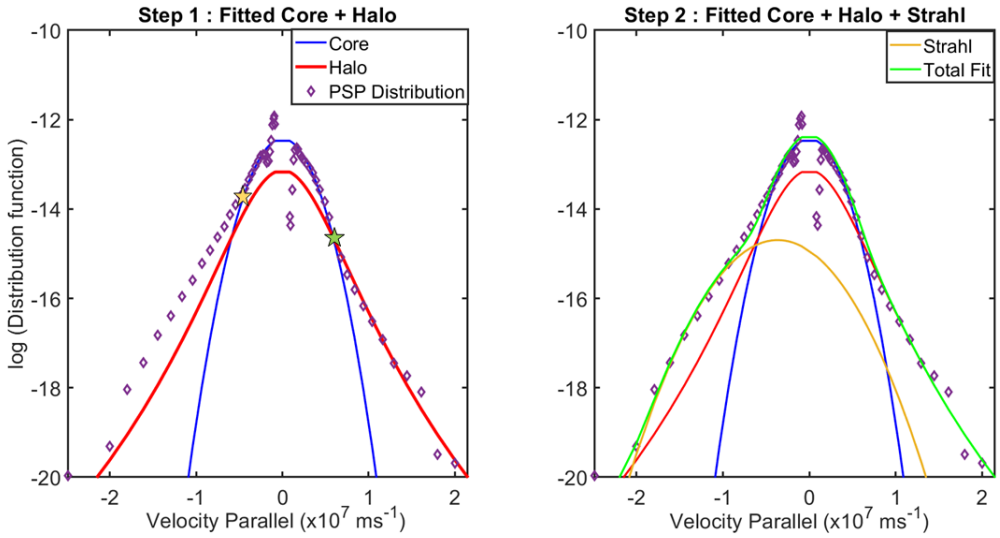

Figure 4.1: Two-step fitting process. The purple diamonds mark the measured distribution at 0.2940 au on 25^{th} Aug 2019 at 03:28:28 UT, red the fit for the bi-Maxwellian core, and blue fit for the bi-kappa halo. The gold line represents the fit for the drifting bi-Maxwellian strahl. The panel on the left shows the core and halo fit for the measured distribution. The green and yellow stars with black border represents the halo and strahl breakpoints obtained from the machine learning. The second fit is shown in the right-hand panel where the strahl is fitted. The green line represents the total fit. This Figure is taken from Abraham et al. (2022a)

there is no strahl detected then we only undertake the first step of the fitting routine. Furthermore, we exclude bidirectional strahl identified by the machine learning algorithm for this study.

A quantitative goodness of fit parameter is evaluated by comparing measured and modelled points along the perpendicular direction, as it is expected that there is no strahl present at these pitch angles, and along the parallel or anti-parallel direction which does not have the strahl (i.e, the anti-strahl direction). This allows us to capture the anisotropic nature of the core and halo populations. To evaluate the overall goodness of the fit, we evaluate the reduced χ^2 parameter:

$$\chi^2 = \frac{1}{n-m}\sum_i \frac{(O_i - C_i)^2}{\sigma^2}, \tag{4.9}$$

where $O_i = \log(\tilde{f}_i/1s^3m^{-6})$ are the measured data point from the measured full distribution function $\tilde{f}_i$, $C_i = \log(f_e/1s^3m^{-6})$ are the fitted data point from the fitted

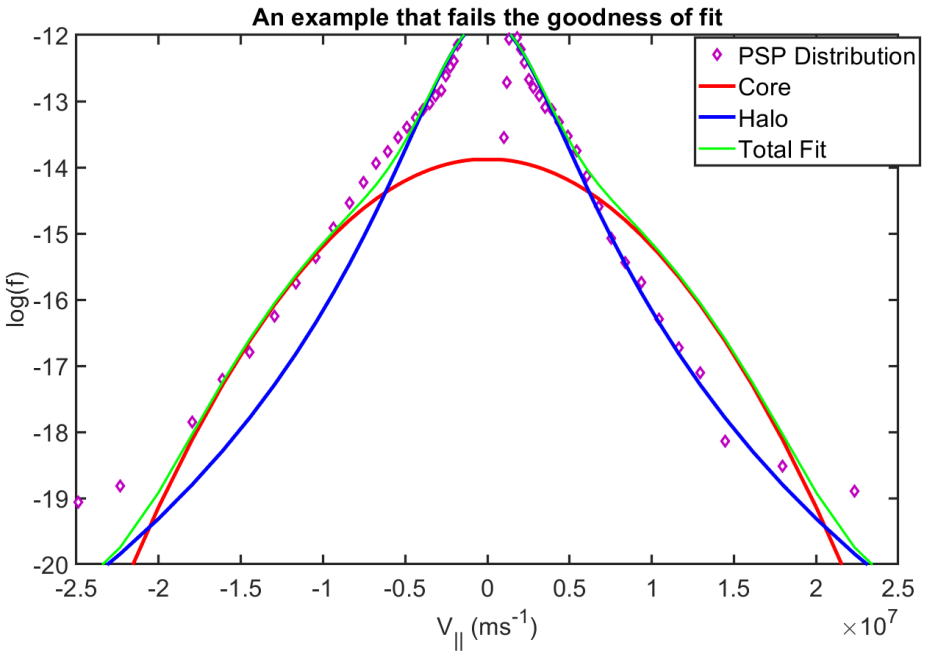

Figure 4.2: An example of a distribution failed the goodness of fit. The purple diamonds mark the measured distribution on 3^{rd} June 2020 at 00:43:17 UT, red the fit for the bi-Maxwellian core, and blue fit for the bi-kappa halo.The green line represents the total fit. The χ^2 of this fitting routine is 2.45.

distribution function,f_e, n is the number of fitted data points, m is the number of variables to fit and σ^2 is the variance of $\log(f_i)$.

We assume that the bulk speeds of the core and halo populations are zero in our fit models in the instrument frame. Consequently, any measured distributions with significant non-zero drifts will manifest as a large reduced χ^2 value and would be excluded from the analysis. Figure 4.2 shows an example of an eVDF that failed the good of fit test. The electron densities and temperatures obtained from the fits were compared and validated with the densities and temperature measurements obtained from the quasi-thermal noise measurements (Moncuquet et al., 2020).

Once that is done, we undertake the analysis of features of the suprathermal populations by taking partial moments of the fitted curve by integrating over the part of velocity space constrained by the breakpoints obtained from the machine learning algorithm described in Section 4.4.1.

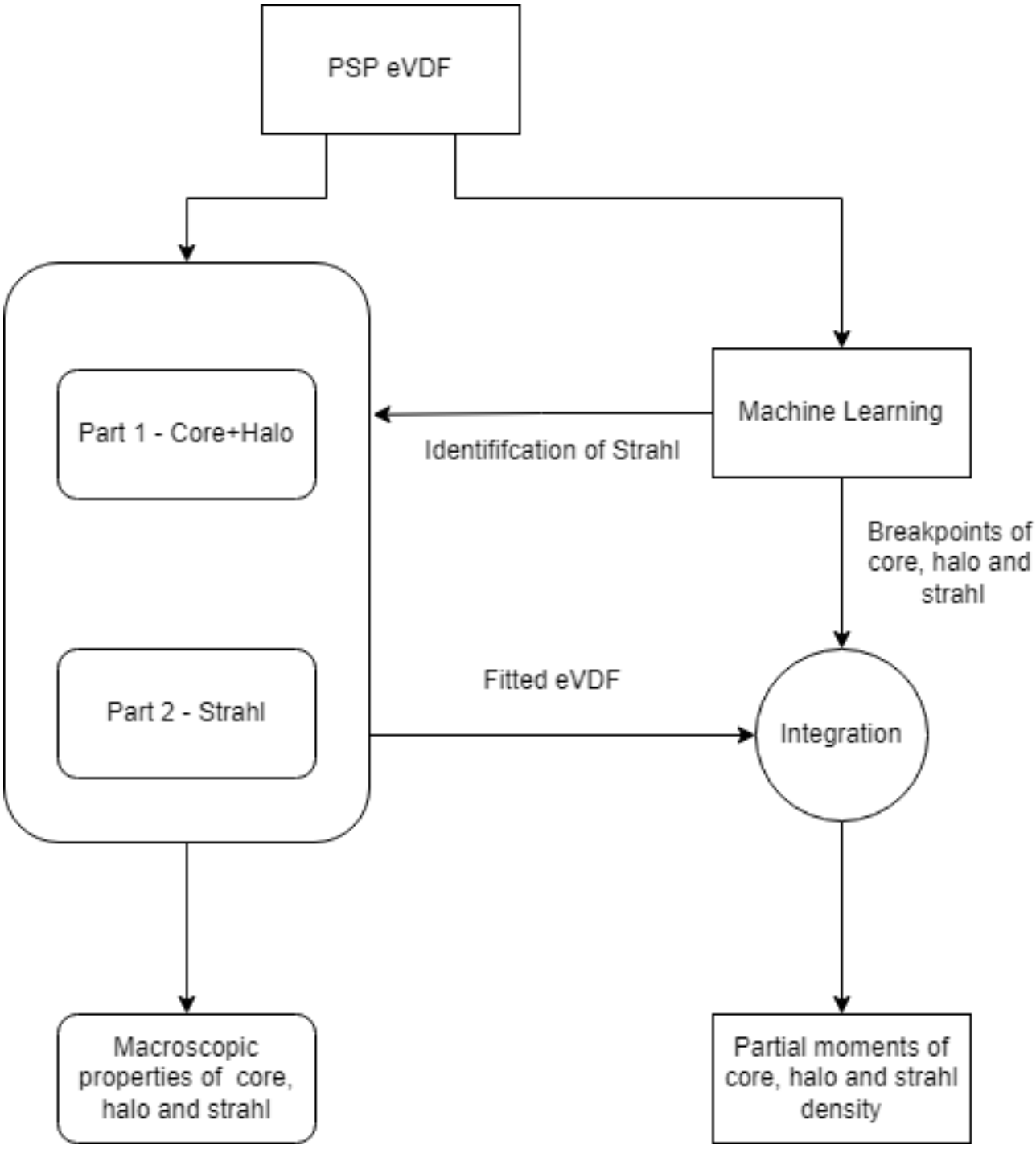

Figure 4.3: Fitting routine flowchart with machine learning. The fitting routine is split into two stages : core and halo fit followed by a strahl fit. The machine learning algorithm outputs for the identification of the strahl is used in the fitting routine. The breakpoints are used to integrate the fitted eVDF to obtain the partial moments.

4.4.3 Error Analysis

We model the overall measurement error as a combination of that given by Poisson statistics, combined with an additional error which reflects the likely systematic error in the instrument measurement, arising due to the finite MCP efficiency and uncertainty in other instrumental effects, which we combine and capture here as an effective overall uncertainty in the instrument geometric factor. The Poisson error is the dominant error source when the number of counts is small. We quantify the relative error in the geometric factor as 10 %, a value which has been adopted following direct discussions with the data provider team.

In the creation of the SWEAP VDF data, the value of the distribution function f_i at a given energy, azimuth, and elevation is calculated based on the raw counts C as :

$$f_i = \frac{{m_e}^2 C}{2\Delta t\, E^2 G}, \tag{4.10}$$

where Δt is the counter readout time, G is the geometric factor, and E is the energy. Based on Gaussian error propagation, the Poisson error and the geometric factor uncertainty lead to the following result for the variance of the data points (i.e., of $\log(f)$) in our measured distribution function:

$$\sigma^2 = \left(\frac{m_e}{\ln(10) E \sqrt{2\Delta t\, G f_i}}\right)^2 + \left(\frac{1}{\ln(10)}\frac{\Delta G}{G}\right)^2, \tag{4.11}$$

where $\Delta G/G = 0.1$ is the relative error in the geometric factor. In our analysis, we only include fits that have a $\chi^2 \leq 1$.

Overall, we have examined over 450,000 electron velocity distribution functions obtained by PSP SWEAP from the years 2019 and 2020. After applying the χ^2 limit and further removal of some clearly non-physical fits, we obtain $\sim$ 300,000 fits for further analysis, of which 220,000 fits have an associated solar wind speed measurement.

4.5 Results

Most of the data measured during this time period are associated with solar wind speeds less than 400 $\mathrm{km\,s^{-1}}$ which we classify as the slow solar wind. We split the data into 50 equal-width radial distance bins, and the median value of a given parameter of interest in each radial distance bin is calculated. We calculated the upper and lower error bar for each radial distance bin as the upper and lower quartile respectively.

Figure 4.4 shows the radial evolution of the averaged fitted parameters. Panel (a) of the Figure shows the averaged core density as a function of the heliocentric distance. This is broadly in line with the expectations for a radial isotropic expansion of this population. The r^{-2} trend is represented by the solid green curve. Below 0.2 au, the halo density (panel (b)) shows only a moderate dependence on heliocentric distance within the error bars. However, over the same radial distance range, the strahl density (panel (c)) has a clearly steeper gradient which is more significant.

The radial evolution of the κ value for the fitted halo distribution is shown in panel (d). The kappa parameter provides a measure of the non-thermal state of the halo population. As κ tends to infinity, the distribution becomes closer to a Maxwellian. For the slow solar wind regime shown here, the κ value is low at ~ 4 for the lowest distances sampled. The κ value rises from $\sim$4 to $\sim$12 between 0.13 au and $\sim$ 0.24 au and thereafter steadily decreasing with increasing radial distance from $\sim$12 at $\sim$ 0.24 au to $\sim$ 7 at $\sim$ 0.5 au.

The thermal speed of the fitted core distribution (panel (e)) stay approximately constant with radial distance with a parallel anisotropy from 0.13 au to 0.2 au, thereafter the thermal speed continue to decrease with increasing radial distance and is approximately isotropic within the error bars. The thermal speed of the fitted halo distribution (panel (f)) initially increases from $2.2\times10^{6}\ m\,s^{-1}$ at 0.13 au to 3.5×10^{6} $m\ s^{-1}$ at 0.24 au and thereafter the thermal speed decrease. The parallel thermal velocity is enhanced above the perpendicular at all distances shown, indicating a persistent anisotropy in the parallel direction for the halo population.

The strahl thermal speed (panel (g)) component is $V_{\parallel_{\omega s}} > V_{\perp_{\omega s}}$ closer to the

Sun like the core thermal speed, but slowly decreases with radial distance, such that this distribution is isotropic (within error bars) by ∼0.2 au, unlike the core and halo thermal velocities, panel (e) and (f) respectively, which both show clear declines with radial distance from 0.2 au onwards.Figure 4.5 shows the relative density of the fitted electron population with respect to the total electron density. The core makes up more than 90% of the electron density and the halo increases from 1 % at 0.13 au to 10 % at 0.25 au and stay constant for distances greater than 0.25 au. The strahl total density stays constant at 1% from 0.13 to 0.5 au. This plot is not comparable to previous observations by Štverák et al. (2009).

To examine the complex radial evolution of the suprathermal population without the ambiguity of the regions of overlapping electron populations and making it comparable to previous observations by Štverák et al. (2009), we numerically integrate the total fitted curve over velocity space using the breakpoints to define the energy and/or pitch angle limits for the core, halo and strahl populations. In Figure 4.6 we present the integrated density evolution of the three electron populations on a common scale as a function of heliocentric distance. Here the integrated core density data are shown in blue, the integrated halo density in orange and the integrated strahl density in yellow. The two suprathermal populations are at least an order of magnitude lower in density than the core population across the entire distance range shown. As mentioned above, the core density falls as r^{-2} up to 0.25 au. From 0.25 au, we note a deviation of the core electron population from the radial expansion line (black dashed line).

Figure 4.6 also shows that from 0.2 au outwards, the halo (orange line) makes up most of the suprathermal population, while the strahl makes up most of the suprathermal population below 0.2 au. Moreover, the evolution of the suprathermal population with radial distance does not follow a r^{-2} trend. Below 0.25 au we see that the halo density decrease with radial distance closer to the Sun, while there is an increase in the strahl density. Above 0.25 au both populations show a steady decline in density with increasing radial distance.

To remove the effects of expansion, we look at the relative densities of the three

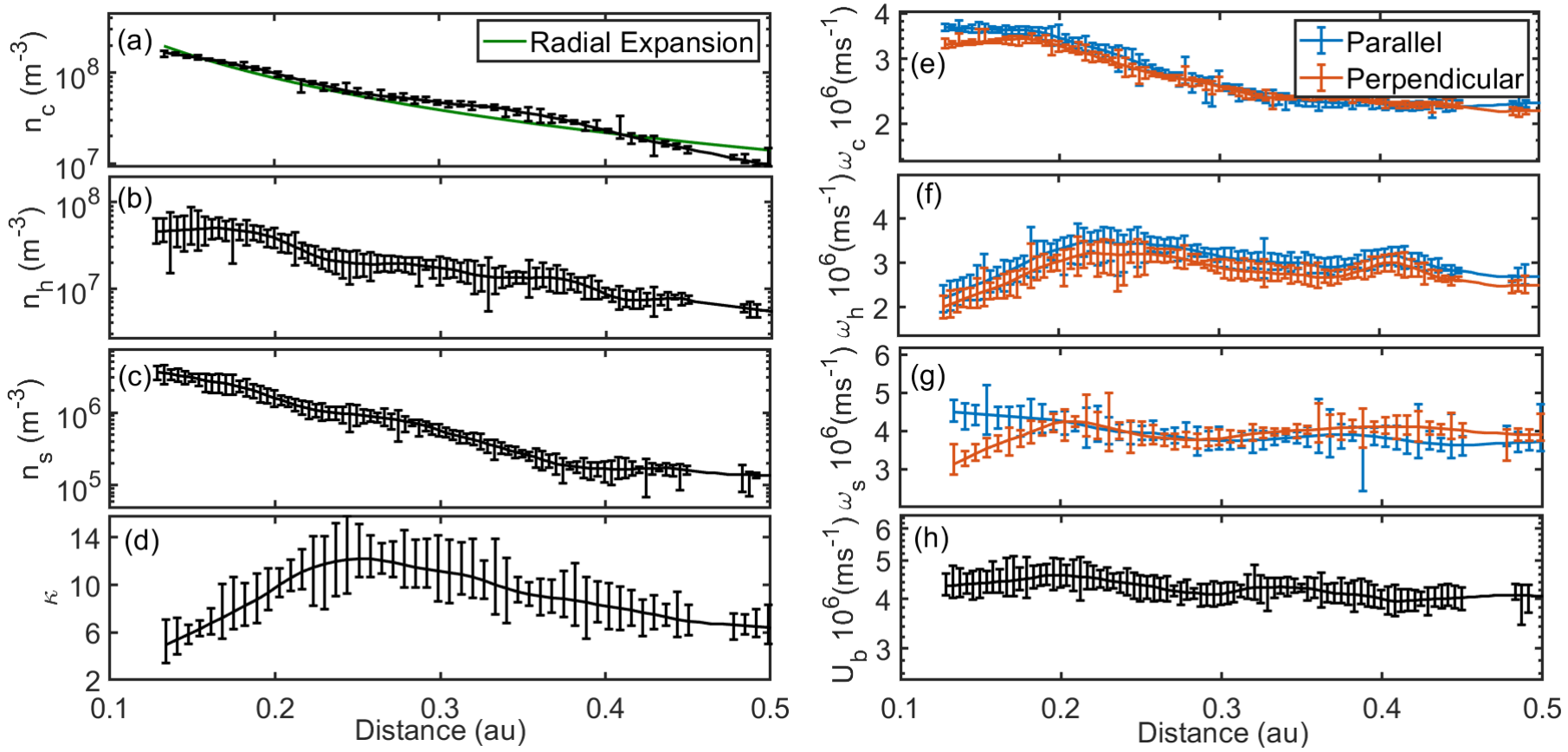

Figure 4.4: The radial evolution of the fit results for solar wind in the speed regime less than 400 kms^{-1}.Panel (a) shows the radial evolution of the core density and the black dashed line shows the expected evolution of an isotropically expanding gas. Panel (b) and (c) represents the radial evolution of the halo and strahl population respectively. Panel (d) shows the radial evolution of the kappa value for the fitted halo population. Panel (e), (f) and (g) represents parallel and perpendicular thermal speeds of the core, halo and the strahl respectively. Panel (h) shows the radial evolution of the strahl bulk parallel thermal speed. This Figure is taken from Abraham et al. (2022a)

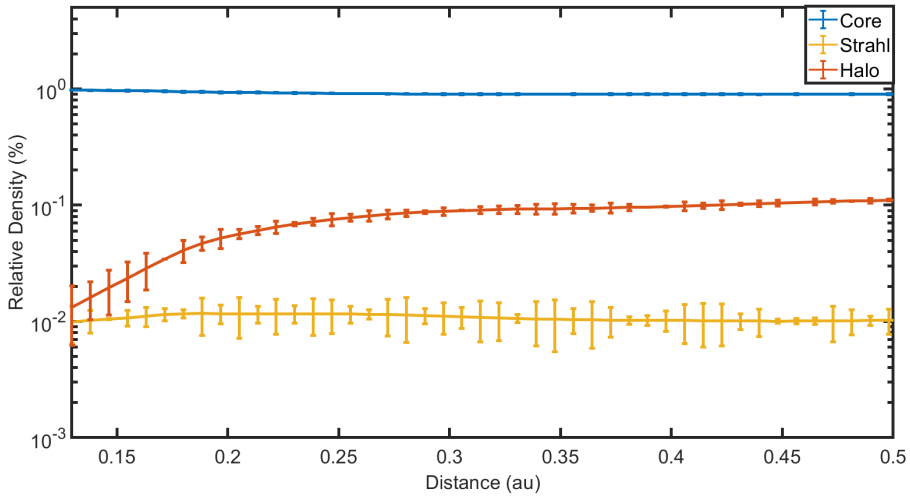

Figure 4.5: The blue line is the core density, the orange line is the halo density, the yellow line is the halo.

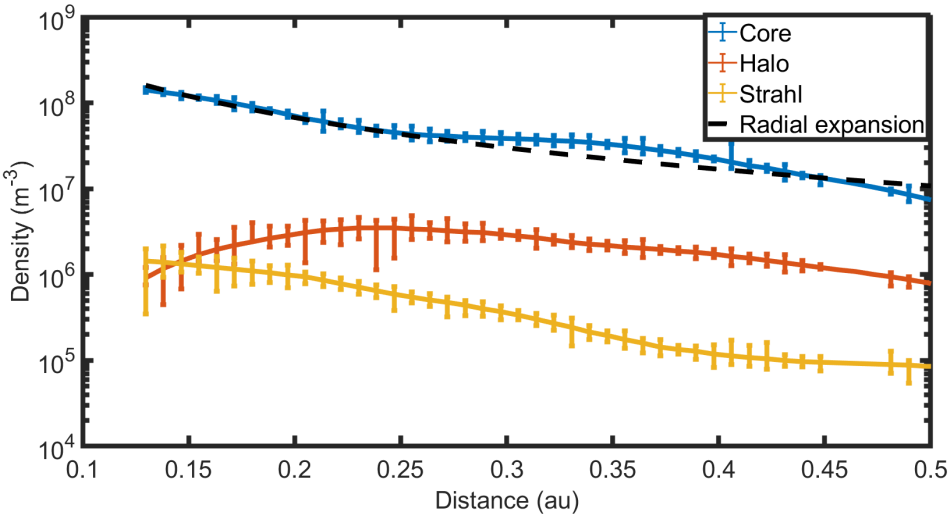

Figure 4.6: The blue line is the core density, the orange line is the halo density, the yellow line is the halo, the black dashed line is the theoretical line for an isotropically expanding gas. This Figure is taken from Abraham et al. (2022a)

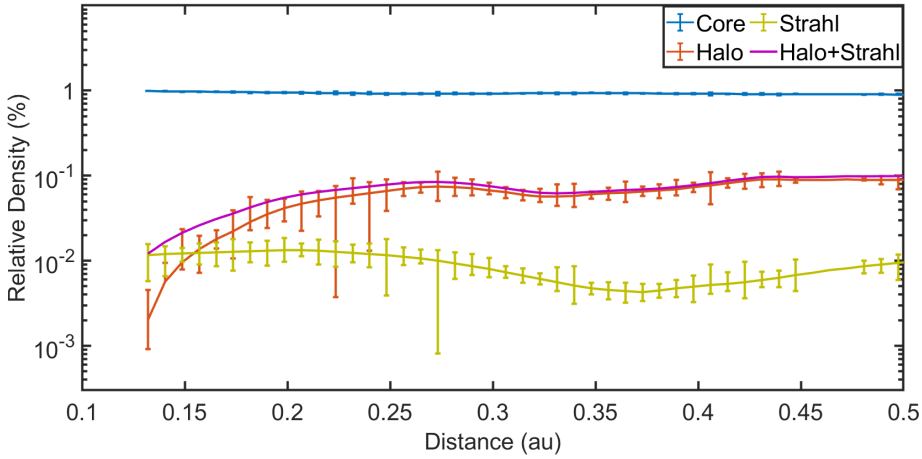

Figure 4.7: The blue line is the core density, the orange line is the halo density, the yellow line is the strahl density and the purple line is the total suprathermal population. This Figure is taken from Abraham et al. (2022a)

electron populations with respect to the total local electron density in a similar way to Štverák et al. (2009). Figure 4.7 shows the relative density of the core population is above 90% across the full distance range sampled. Thus, the combined density of the suprathermal populations (shown in these plots by the purple line) makes up to 10% of the total electron density observed at any distance. From 0.124 au to 0.25 au the relative halo density (orange line) increases from less than 1% to $\sim$ 9% of the total electron density. Between 0.15 and 0.2 au there is a point in which the relative halo density is equal to the relative strahl density, which we will refer to as the *halo strahl cross over* point in this Chapter. It is not straightforward to determine the exact location of the *halo strahl cross over* point due to the size and overlaps in the error bars. The relative strahl density stays approximately constant ($\sim$1%) below 0.25 au, but there is a sharp rise in relative halo density from less than 1% to $\sim$8%. The total fractional density of the combined suprathermal populations rises from $\sim$ 1% at the closest distances sampled ($\sim$0.13 au) to almost 10% above 0.25 au.

To examine this in more detail, we looked at the average shape of the distribution function below the *halo strahl cross over* point. For this subselection of data, most of the VDFs can be described well with just the core and strahl elements of the model fit, with no explicit need to include a halo model, as seen from the example distribution/fits illustrated in Figure 4.8. It also shows the signature of electron

deficit which will be addressed in Chapter 6.

4.6 Discussion

The relative densities and radial trends of properties of the core electron population are broadly in agreement with previous observations by Maksimovic et al. (2005) and Štverák et al. (2009) for distances > 0.28au. These authors demonstrated, for this distance range, that the relative density of the strahl is greater than the relative density of the halo closer to the Sun ($\sim$ below 0.6 au). Contrary to these previous results, our observations show that the relative density of the two suprathermal electron populations does not evolve in an inverse manner below 0.3 au, where the strahl density decreases as the halo density increases. Below 0.2 au, the total fractional density of the suprathermal population is not constant, but drops from $\sim 10\%$ to $\sim 1\%$. This would imply that with increasing distance from the Sun there must be some process or processes which drive an increase in the total number of electrons in the suprathermal energy range. The most likely source of these electrons would be the core in this region. If this is the case, then it is possible that the quasi-isotropic nature of the halo could be explained by a process which creates the halo from the core population. Extrapolating the lines in Figure 4.7 to distances closer to the Sun, we notice for the slow solar wind the distribution function can be typically represented by a core and a strahl model without a significant halo component.

The fact that the fractional strahl density remained relatively constant $\sim$1% and fractional halo density increased from less than 1% at 0.124 au to $\sim$9% at 0.25 au shows that the halo cannot just be formed from the scattering of strahl alone, as suggested by Štverák et al. (2009). Thus, there appears to be more than one process contributing to the growth of the halo population. This may be a multi-stage process in which, say, a fraction of the core population is accelerated to suprathermal energies by a resonant wave-particle interaction or other plasma processes. Alternatively, larger scale dynamics may play a role, such as the field-aligned acceleration of reconnection outflow beams, followed by scattering in pitch angle to form the halo. Further analysis is needed to confirm the nature of any such relationship be-

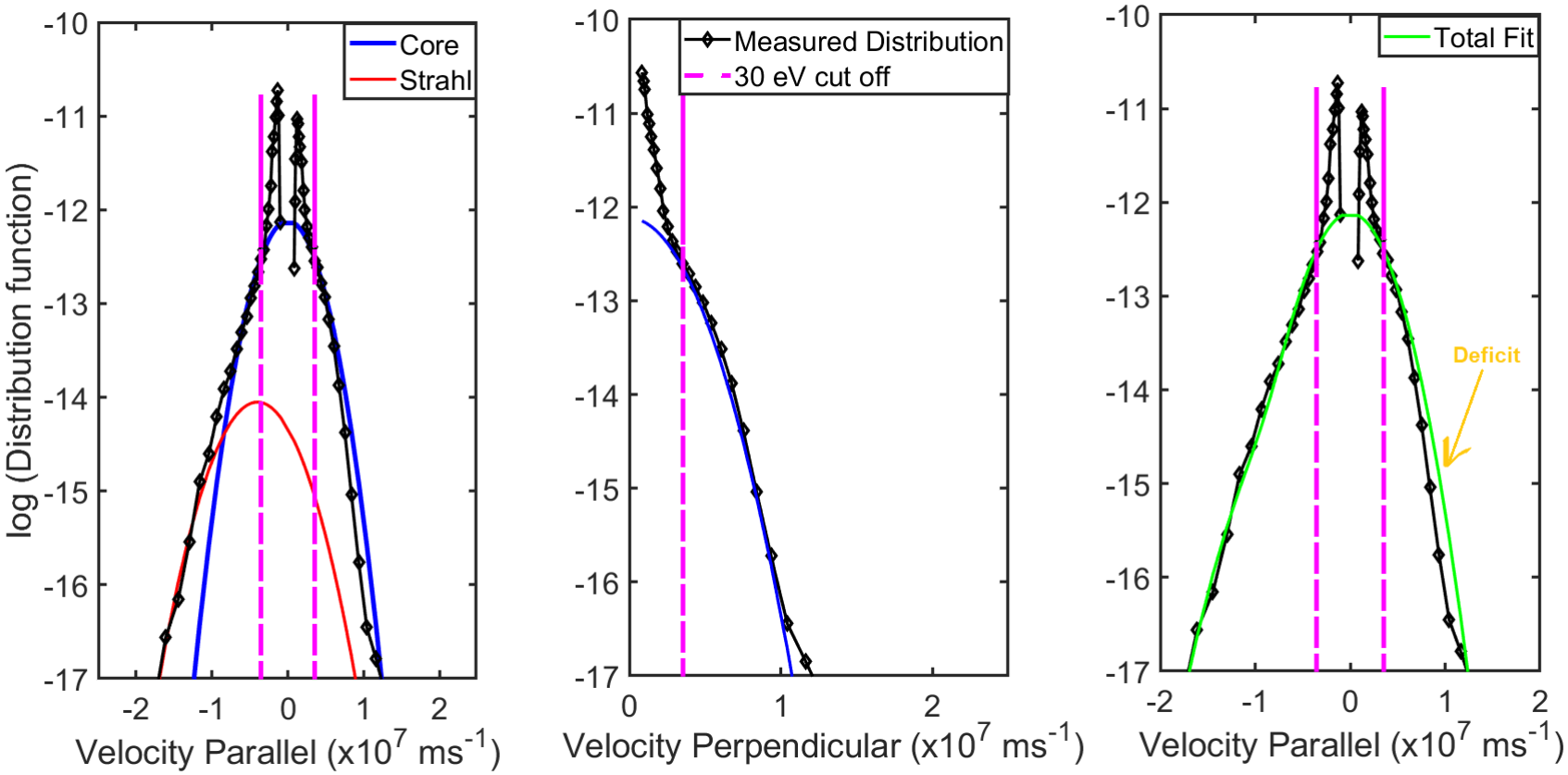

Figure 4.8: A representative distribution recorded at a distance of 0.13 au. The black trace with diamonds shows the measured distribution. The blue trace represents the output of our fitting routine for a Maxwellian core, and the red trace represents the output for the fit to a Maxwellian strahl drifting along the B-field direction. The pink vertical dashed lines represent the 30 eV measurement energy below which we do not fit to data due to secondary electron contamination, as discussed in the text. The left-hand panel shows a cut along the parallel velocity direction, while the middle panel shows the cut along $V_{||}$=0 in the perpendicular direction. In the right-hand panel, the green trace shows the final combined fitted curve to the measured distribution. Note that this panel indicates an excellent fit to the data without the need to infer a third fit for the halo model, such that the halo contribution to this fit is negligible. The orange arrow points to a portion of the distribution in anti-sunward direction where the distribution gradually decreases away from the Maxwellian fit. This feature is called a deficit. This Figure is adapted from Abraham et al. (2022a)

tween the core and the suprathermal population.

We also define the *halo strahl cross over* point, as the point where the halo density and strahl density are equal. Below the *halo strahl cross over* point most of the suprathermal population moves along the field line while above this point most of the suprathermal population is present at all pitch angles. This point maybe important in the study of processes that concern the evolution of the suprathermal populations. However, the fractional trends in Figure 4.6 show that the total suprathermal population continues to decrease in the same radial distance range.

We have also specifically examined electron VDFs which were recorded at radial distances below the the *halo strahl cross over* point. Electron distributions below 0.15 au can be well described with only a core and a strahl model as shown by a representative example in Figure 4.8. Another feature we often note at the closest distances sampled is a deficit in the measured distribution function, with reference to the core fit, in the anti-strahl direction. Halekas et al. (2020) examined the first 2 orbits and reported a similar truncation in the Maxwellian core distribution. This deficit is not included explicitly by the version of our model used in this Chapter, and this means the core density estimate at the closest distances to the Sun maybe slightly overestimated. However, if the deficit is sufficiently large then this should result in a large reduced sum of the squares and thus such cases would have been discarded from our analysis.

Another interesting result from our analysis is the variation in the κ value with radial distance. The variation in κ indicates the change in the average shape of the high energy tails with radial distance. At the closest distance sampled, the κ value is ~ 4 and rises to 11 around 0.25 au. When we compare this rise in κ with the halo density trend shown by Figure 4.7 we notice that the halo density was less than 0.01 % and rises to ~ 8 % from 0.13 to 0.25 au.

From panel (e) to (g) of Figure 4.4, we are able to infer the non-adiabatic nature of the slow solar wind. At the closest distance sampled there seems to be a persistent anisotropy in all three electron populations, with the strahl exhibiting the strongest parallel enhancement over perpendicular thermal speed. The core popu-

lation cooling rate varies with radial distance while remaining quasi-isotropic with similar perpendicular and parallel thermal speeds within the error bars. However, the halo thermal speed initially rises from 2×10^6 $m\ s^{-1}$ at 0.13 au to 3.7×10^6 $m\ s^{-1}$ at 0.25 au and then decreases with radial distance. The initial rise can be attributed to the growth of the halo as more particles populate the upper halo energy range. We are unaware of any theory that explains these thermal trends. Further research into what drives the global thermal trends is needed.

As evident from Figure 4.4, the strahl parallel thermal velocity does not vary with radial distance when fitted to a drifting bi-Maxwellian model. This result has also been reported by Berčič et al. (2020). This result is consistent with a recent kinetic model for the strahl evolution in the inner heliosphere, which also shows that the strahl parallel temperature and bulk velocity are constant with heliocentric distance (Jeong et al., 2022b). In exospheric models, the strahl is believed to carry information about the exobase (Jockers, 1970), which means that the constant strahl parallel temperature and bulk speed provides critical information about the coronal electrons at its origin. The temperature associated with the strahl parallel thermal speed derived from our fits is approximately the same magnitude as the typical temperature on the corona ($\approx 10^6$ K). Further analysis of data taken closer to the Sun during future PSP encounters will be needed to confirm whether the strahl parallel temperature indeed preserves the coronal electron temperature. The core and strahl have a parallel anisotropy closer to the Sun at 0.13 au, but this anisotropy decreases with increasing radial distance and approaches isotropy within the statistical errors. Another new finding from our work is that the strahl parallel bulk speed stays roughly constant within the error bars. This means that the strahl could be a useful indicator of the origins of the source regions of the solar wind (Hefti et al., 1999; Berčič et al., 2020).

In exospheric solar wind models, the electrons with energy less than the electric potential at a given radial distance are reflected and are trapped in a potential well Maksimovic et al. (2001). The deficit in the distribution function that we observe in the anti-strahl direction could then be a result of the existence of this trap-

ping boundary explained in Chapter 2. However in this theory, this cut-off in the distribution is quasi-discontinuous as shown by 2.7, while we observe a smoother drop below the Maxwellian VDF values in the sunward side of the VDF. Regardless, more research is required to better understand these deficits by quantifying the point where the Maxwellian truncates, since they potentially give insight into the role of the interplanetary electrostatic potential for the acceleration of the solar wind. We will further examine this feature in more detail in Chapter 6.

4.7 Summary and Conclusions

We have applied a new and novel fitting routine to electron VDF measurements, which for the first time incorporates breakpoint energies obtained from a machine learning algorithm (Bakrania et al., 2020).This new technique was applied to a large data set of PSP SPAN observations of electrons at varying distance from the Sun. We use our fitting results to investigate the evolution of the eletron core, halo and strahl for encounters 2, 3, 4, and 5. We have shown that the core makes up more than 90% of the total electron density for all the distances sampled, whereas the non-thermal electrons make up less than 10%, which is agreement with observations for distance $>$ 0.3 au (Maksimovic et al., 2005; Štverák et al., 2009; Halekas et al., 2020). The radial r^{-2} dependence of the core population extends below 0.3 au. Observations at radial distances greater than 0.3 au have shown that the relative density of the suprathermal population stays constant which is in agreement with our observation greater than 0.3 au (Štverák et al., 2009; Maksimovic et al., 2005). However a new novel result we find is that this is not the case belwo 0.2 au. We have shown that the relative suprathermal population increases from $\sim$ 1% at the closest distances sampled to $\sim$ 10% around 0.2 au. This indicates that there is a relative increase in the non-thermal particle densities over the inner regions of the heliosphere.

Furthermore, prevcious missions have shown that are larger distances greater than 0.5 au the halo and strahl densities have an inverse relationship (Štverák et al., 2009). our analysis does not reveal a distinct inverse relationship between the den-

sities of the halo and strahl population below 0.25 au. Rather, we find that the strahl density stays approximately constant whilst the halo density increases. We note a point called the *halo strahl cross over* point, where the relative halo density is equal to the relative strahl density. At the closest distances sampled, i.e. below this point, the distribution can generally be well modelled with only a core and strahl components of the fit, with little/no contribution from the halo model. The often negligible halo density closer to the Sun suggests the halo drops below the one count sensitivity level of the instrument.

As far as we are aware there is no studies that examined the densities and temperature of the solar wind in a statistical manner as we have presented in this Chapter. We find that strahl parrallel temperature and the parallel temperature could be used a tracer for coronal origins. We also show for the first time that below 0.2 au where halo popualtion is nelgible that core and strahl parrallel temperaures stays constant radial distance with a strong parralel anisotropy which tends to quasi-isotropic within the error bars when the halo population has formed.

Another key feature we report is that, below the *halo strahl cross over* point, we generally see a distinct deficit in the core population in the anti-strahl direction. This indicates that there are fewer particles in the part of velocity space corresponding to particles returning in the direction of the Sun, compared to that expected from the Maxwellian fit. Such a cut-off in the distribution is predicted by Maksimovic et al. (2001). However, above the *halo strahl cross over* point we do not generally see such a deficit in the distribution with respect to the modelled fits.

In Chapter 6, we quantify the nature of these deficits with a bespoke fitting routine which helps us to better understand the role the interplanetary electrostatic potential could play in solar wind acceleration. An interesting avenue for further research would be to look at alignments of Solar Orbiter with Parker Solar Probe to study the same plasma stream with this technique. Further to this, examining the growth of the non thermal halo populations can give insights into the origins of the κ distribution which is ubiquitous in space as discussed in Chapter 7.

Chapter 5

The Thermal energy budget of electrons in the inner heliosphere: Parker Solar Probe Observations

5.1 Preface

This Chapter contains results, discussion, and conclusions which have been published as Abraham et al. (2022b). Under the supervision of Professor Christopher J. Owen and Dr. Daniel Verscharen, this work was carried out also in collaboration with Dr. Jefferson Agudelo, who derived the theoretical complete expression for the second moment of the Boltzmann equation. This work carries on from the results obtained from Chapter 4.

5.2 Introduction

The solar wind is a highly-ionized plasma that continuously flows out from the solar corona and fills the heliosphere with protons, electrons, α-particles, and small traces of heavier ions (Marsch, 2006). Electron populations evolve in a complex manner as they propagate into the heliosphere under the influence of processes such as expansion, turbulent dissipation, plasma instabilities, wave–particle interactions, Coulomb collisions, global electric fields, and gravity (Lie-Svendsen et al., 1997; Vocks and Mann, 2003; Smith et al., 2012; Jeong et al., 2022b). Each of these

processes may play a role in modifying the shape of the eVDF, which in turn has significant ramifications for the solar wind energy budget.

Electrons have a strong impact on the solar wind thermodynamics. Due to their small mass compared to the ions, electrons make negligible contributions to the solar wind's total mass, momentum, and kinetic-energy fluxes. However, due to their larger thermal speeds, electrons play a key role in influencing the thermal energy budget by efficiently carrying away heat from the Sun (Cranmer et al., 2009; Landi et al., 2014; Štverák et al., 2015; Halekas et al., 2021). Most kinetic models of solar wind acceleration rely on a contribution from an electric field which arises due to ambipolar diffusion, which in turn is a consequence of the strong electron pressure gradient between the corona and the heliosphere (Parker, 2010; Lemaire and Scherer, 1971).

As discussed in Chapters 2 and 4, the electron VDF is often reported to be composed of three populations: the core, the halo, and the strahl (Feldman et al., 1975; Maksimovic et al., 2005; Štverák et al., 2009; Abraham et al., 2022a). The thermal core population usually takes a Maxwellian form and comprises more than 90% of the total local electron density. The halo population is present at higher energies and is often modelled as a bi-κ-distribution. The core and halo are each quasi-isotropic and thus have significant electron fluxes at all pitch angles. The strahl takes the form of a magnetic-field-aligned beam of electrons moving parallel or anti-parallel (or sometimes bi-directionally) to the local magnetic field.

In-situ observations of the solar wind electron temperature gradients often show deviations from those expected for adiabatic profiles, but vary between adiabatic and isothermal expectations (Ogilvie and Scudder, 1978; Feldman et al., 1979; Pilipp et al., 1990; Maksimovic et al., 2000). This observation motivates the important question regarding the physical mechanisms responsible for the non-adiabatic evolution of the plasma electron populations. To date, few studies have addressed the non-adiabatic evolution of the electron temperature. However, Pilipp et al. (1990), Cranmer et al. (2009), and Štverák et al. (2008) have tried to quantify the heating/cooling rate required in the solar wind to support the observed radial

profiles of the temperature and the electron heat flux, as discussed in Chapter 2.

In this Chapter, we evaluate the electron thermal energy balance by first providing and examining an exact and complete description of the thermal energy density based on the second moment of the Boltzmann equation. We address the fundamental question about the deposition rate of thermal energy between various contributions to the budget as a function of heliocentric distances in the very inner heliosphere. We quantify contributions of thermal energy sinks and sources using the PSP dataset.

In Section 5.3, we derive a framework based on the second moment of the Boltzmann equation to study the conservation of thermal energy. This approach is based on the theoretical framework developed by Agudelo Rueda et al. (2022) and Agudelo Rueda (2022). In Section 5.4, we apply this framework to our PSP dataset described in Chapter 4. In Section 5.5, we present our results. In Section 5.6, we discuss our results and the implications of this work. Finally, in Section 6.6, we summarize our findings and outline perspectives for future work.

5.3 Thermal Energy Budget

The evolution of the eVDF in phase space follows the Boltzmann equation,

$$\frac{\partial f}{\partial t} + \mathbf{v}\cdot\nabla f + \frac{q}{m}(\mathbf{E}+\mathbf{v}\times\mathbf{B})\cdot\nabla_{\mathbf{v}} f = \left(\frac{df}{dt}\right)_{Coll}, \tag{5.1}$$

where f is the eVDF, t is the time, $\mathbf{v}$ is the particle velocity, q is the charge of a particle, m is the mass of a particle, $\mathbf{E}$ is the electric field, and $\mathbf{B}$ is the magnetic field. The term $\left(\frac{df}{dt}\right)_{Coll}$ represents the change in the distribution function due to collisions.

To address the thermal energy budget of the electrons, we take the second moment of Equation (5.1) for electrons, which leads to the following differential equation:

$$\frac{\partial \varepsilon}{\partial t} + (\mathbf{u}_e\cdot\nabla)\varepsilon + \nabla\cdot\mathbf{h}_e + \nabla\mathbf{u}_e : \mathsf{P}_\mathsf{e} + (\nabla\cdot\mathbf{u}_e)\varepsilon = \Xi, \tag{5.2}$$

where ε is the thermal energy density, $\mathbf{h}_e$ is the electron heat flux, $\mathbf{u}_e$ is the electron bulk velocity, P_e is the electron pressure, and Ξ is the irreversible contribution to

the thermal energy budget (i.e., the second moment of $(df/dt)_{Coll}$). The thermal energy density ε is defined as

$$\varepsilon = \frac{1}{2}\mathrm{Tr}(\mathsf{P_e}), \tag{5.3}$$

where $\mathrm{Tr}(\mathsf{P_e})$ is the trace of the electron pressure tensor and P_e is defined by Equation (1.29).

The left-hand side of Equation (5.2) is the reversible transfer of the thermal energy density, and the right-hand side is the irreversible transfer of the thermal energy density. On the left-hand side, the first term describes the partial time derivative of the thermal energy density. The second term describes the advection of ε with $\mathbf{u}_e$. The third term describes the divergence of the electron heat flux. The fourth term describes the pressure-strain term, and the fifth term describes the expansion/contraction of the solar wind plasma. The right-hand side represents any spatial deposition of thermal energy through irreversible processes. If the right-hand side is zero then the energy budget of the measured electron distribution evolves reversibly. If the right-hand side is non-zero, then the thermal energy budget of the electron distribution have an sink or a source of thermal energy density. The quantity Ξ thus corresponds to the irreversible thermal power density of the electrons. Equation (5.2) does not encapsulate the full energy conservation of the solar wind because it does not account for the electromagnetic energy, the electron bulk kinetic energy, and the energy associated with other particle species. However, Equation (5.2) is accurate and complete in its description of the thermal energy budget of the electron species.

We transform Equation (5.2) into a format in which we can use fit parameters of our electron VDF fits as inputs. As we use data from a single spacecraft, it is not possible to measure the temporal evolution of the plasma, which would requires multi-spacecraft measurements. We thus assume steady-state conditions, which removes the partial time derivative in Equation (5.2). Therefore, all remaining terms on the left-hand side of Equation (5.2) arise from free-streaming effects in Equation (5.1).

5.3.1 Advection of the thermal energy density by bulk flows

Assuming spherical symmetry, we write the second term of Equation (5.2) as,

$$(\mathbf{u}\cdot\nabla)\varepsilon = u_r\frac{\partial\varepsilon}{\partial r}, \tag{5.4}$$

where u_r represents the radial electron bulk speed.

In our data analysis, we use the radial proton speed instead of the radial electron speed for u_r because of the technical difficulty in determining the electron radial speed from data directly. The proton radial speed is approximately the same as the electron bulk speed due to the zero-current requirement (Pierrard et al., 2020).

Our fit results from Chapter 4 provide macroscopic properties such densities, bulk velocities and pressure tensors for the three electron populations separately (Abraham et al., 2022a). We now derive total electron moments from these quantities. Integrating and solving for Equation (1.29) in terms of each electron population, we obtain the following:

$$\mathsf{P_e} = \mathsf{P}_c + \mathsf{P}_h + \mathsf{P}_s + m_e\left[n_s(u_s-u_e)^2 + n_c(u_c-u_e)^2 + n_h(u_h-u_e)^2\right]\hat{\mathbf{b}}\hat{\mathbf{b}}, \tag{5.5}$$

where n_c is the core density, n_h is the halo density, n_s is the strahl density, u_c is the core bulk speed, u_h is the halo bulk speed, u_s is the strahl bulk speed, u_e is the electron bulk speed and $\hat{\mathbf{b}}\hat{\mathbf{b}}$ is the dyadic product of $\hat{\mathbf{b}} = \mathbf{B}/|\mathbf{B}|$ with itself. The total pressure arises from the thermal pressures of each population and from the drifts of each population with respect to the electron bulk speed. Taking the trace of the pressure tensor from Equation (5.5), we obtain

$$\mathrm{Tr}(\mathsf{P}_e) = \sum_{j=c,h,s}(n_j k_b(2T_{\perp j} + T_{||j}) + n_j m_e(u_j - u_e)^2), \tag{5.6}$$

where the subscript j indicates the core (c), halo (h) and strahl (s) populations, k_b is the Boltzmann constant, $T_{\perp j}$ is the perpendicular temperature, $T_{\|j}$ is the parallel temperature, and u_j is the bulk speed of population j.

We decompose the total electron bulk speed as

$$\mathbf{u}_e = \frac{1}{n_e}\sum_j n_j \mathbf{u}_j, \tag{5.7}$$

where $n_e = n_c + n_h + n_s$ is the total electron density. Substituting Equation (5.6) into Equation (5.4), we obtain

$$(\mathbf{u}\cdot\nabla)\varepsilon = \frac{1}{2}u_r\frac{\partial}{\partial r}\sum_{j=c,h,s}\left[n_j k_b(2T_{\perp j} + T_{||j}) + n_j m_e(u_j - u_e)^2\right]. \tag{5.8}$$

5.3.2 Divergence of Heat Flux

The third term in Equation (5.2) describes the divergence of the electron heat flux. The divergence of the heat flux can be expressed as

$$\nabla\cdot\mathbf{h_e} = \frac{1}{r^2}\frac{\partial(r^2 h_r)}{\partial r}, \tag{5.9}$$

where h_r is the radial electron heat flux. The heat flux vector is defined as the third moment of the VDF:

$$\mathbf{h}_e = \frac{1}{2}\int f_e(\mathbf{v}-\mathbf{u_e})\cdot(\mathbf{v}-\mathbf{u_e})(\mathbf{v}-\mathbf{u_e})d^3v. \tag{5.10}$$

Integrating Equation (5.10) yields:

$$h_r = \sum_j\left[h_{rj} + \frac{3}{2}n_j k_b T_{||j}(u_j - u_e) + (u_j - u_e)n_j k_b T_{\perp j} + \frac{1}{2}m_e n_j (u_j - u_e)^3\right]\hat{b}_r, \tag{5.11}$$

where h_{rj} represents the intrinsic heat flux of population j that arises due to reflectional asymmetries in the individual population's distribution around its bulk speed. For symmetric component VDFs, this terms vanishes. Substituting Equation (5.11) into Equation (5.9), we obtain the following expression for the divergence of the heat flux in terms of the fit parameters:

$$\nabla \cdot \mathbf{h_e} = \frac{1}{r^2}\frac{\partial}{\partial r} r^2 \sum_j \left[\frac{3}{2} n_j k_b T_{||j} (u_j - u_e) + (u_j - u_e) n_j k_b T_{\perp j} + \frac{1}{2} m_e n_j (u_j - u_e)^3 \right] \hat{b}_r. \tag{5.12}$$

5.3.3 Pressure strain term

The fourth term in Equation (5.2) is called the pressure strain term. This term quantifies a contribution to the thermal energy density by pressure that is advected by spatially inhomogeneous bulk flows. Yang et al. (2022) show that the pressure strain term serves as an estimate of the transfer of bulk-flow energy into thermal energy. Therefore, the pressure strain term is an important tracer for changes in internal energy.

Using Equation (5.5), we obtain the following expression for the pressure strain term:

$$\nabla \mathbf{u}_e : \mathsf{P}_e = \sum_j (\nabla \mathbf{u_j} : \mathsf{P}_j + \nabla \mathbf{u_j} : m_e (n_j (u_j - u_e)^2) \hat{\mathbf{b}} \hat{\mathbf{b}}. \tag{5.13}$$

We fit our data in the magnetic field aligned coordinate system $(V_{\|}, V_{\perp_1}, V_{\perp_2})$. For our analysis of Equation (5.2), we work in the spherical coordinate system (radial distance r, polar angle θ, azimuth angle ϕ). To account for this, we transform the pressure tensor from the magnetic field aligned frame to the spherical coordinate frame by applying the following transformation:

$$T^{-1} \tilde{\mathsf{P}}_e T = \mathsf{P}_e, \tag{5.14}$$

where T is the transformation matrix, T^{-1} is the inverse of the transformation matrix, $\tilde{\mathsf{P}}_e$ is the pressure tensor in the magnetic field aligned frame, and $\mathsf{P_e}$ is the pressure tensor in the spherical coordinate frame. The transformation matrix is defined as follows with the assumptions $u_\phi \neq 0$, $u_\theta = 0$, $\partial/\partial\theta = 0$, and $\partial/\partial\phi = 0$:

$$T = \begin{pmatrix} a_1 b_T & -a_2 b_T & -a_3 \\ a_2 & a_1 & 0 \\ b_R & -b_N & b_T \end{pmatrix}, \tag{5.15}$$

where

$$a_1 = \frac{B_R}{\sqrt{B_R^2+B_N^2}}, a_2 = \frac{B_N}{\sqrt{B_R^2+B_N^2}}, a_3 = \frac{\sqrt{B_R^2+B_N^2}}{|B|}, b_R = \frac{B_R}{|B|}, b_T = \frac{B_T}{|B|}, b_N = \frac{B_N}{|B|}, \tag{5.16}$$

B_R is the magnetic field component in the radial direction, B_T is the magnetic field component in the tangential direction, and B_N is the magnetic field component in the normal direction. Applying the transformation in Equation (5.14), we rewrite Equation (5.13) as

$$\nabla \mathbf{u}_e : \mathsf{P}_e = \frac{\partial u_r}{\partial r}\mathsf{P}_{e,rr} + \frac{u_r}{r}(\mathsf{P}_{e,\theta\theta} + \mathsf{P}_{e,\phi\phi}) + \frac{\partial u_\phi}{\partial r}\mathsf{P}_{e,r\phi} - \frac{u_\phi}{r}\left(\mathsf{P}_{e,r\phi} + \frac{\mathsf{P}_{e,\theta\phi}}{\tan\theta_B}\right), \tag{5.17}$$

where θ_B is the angle between the magnetic field direction and the radial direction.

5.3.4 Expansion term

The fifth term in Equation (5.2) quantifies the effects of expansion and compression on the thermal energy density:

$$(\nabla \cdot \mathbf{u}_e)\varepsilon = \frac{1}{r^2}\frac{\partial (r^2 u_r)}{\partial r}\varepsilon. \tag{5.18}$$

This term arises from the acceleration and deceleration of the electron population.

5.3.5 Polytropic index

Although our kinetic description in Equation (5.2) does not require a polytropic closure, it is useful to compare our results with the polytropic properties of the electron fluid in the solar wind. The polytropic relationship describes the correlation between the pressure and the density of a fluid during a transition from one state to another. During a polytropic process, the ratio of the energy transferred as heat over the energy done as work is constant (Parker, 1963; Chandrasekhar, 1967). For an electron plasma, the polytropic relationship is given as

$$P_e \propto n_e^{\gamma_e} \tag{5.19}$$

where P_e is the scalar electron pressure, n_e is the total electron density, and γ_e is the electron polytropic index. The polytropic relationship brings closure to the moments' hierarchy, (e.g., Kuhn et al., 2010) as it relates higher-order moments (pressure or temperature) with the zeroth order moment (density). Moreover, the value of the polytropic index is a useful metric to investigate the nature of the mechanism in the solar wind electrons that involve heat transfer. By taking the logarithm of Equation (5.19), we obtain

$$\log(P_e) = \gamma_e \log n_e + C, \tag{5.20}$$

where C is a constant. Equation (5.20) allows us to determine γ_e from linear fits to observations of $\log(P_e)$ vs $\log(n_e)$. The slope of the fitted polytropic model determines γ_e (Totten et al., 1995; Nicolaou et al., 2020). An adiabatic electron fluid exhibits $\gamma_e = 5/3$, and an isothermal electron fluid exhibits $\gamma_e = 1$.We calculate the scalar pressure as $P_e = \mathrm{Tr}(\mathsf{P}_e)/3$.

5.4 Parker Solar Probe Data

We analyse the electron VDFs measured by the Solar Wind Electrons, Alphas and Protons (SWEAP) instrument suite onboard PSP (Kasper et al., 2016), described in Chapter 3. We use the fitted parameters of the electron populations needed for this Chapter from Chapter 4.

5.4.1 Data handling

We use the fitted parameters directly to calculate all the terms in Equations (5.8), (5.12), (5.17), and (5.18). We then split the data into 10 radial bins and use the central difference method to approximate the necessary radial gradients. We account for the statistical uncertainties in each term in Equations (5.8), (5.12), (5.17), and (5.18) by propagating the errors of the fitted parameters using Monte Carlo error propagation technique evaluated 100 000 iterations. For each radial distance bin, we plot the mean and the confidence interval as the standard deviation of the sorted samples from the Monte Carlo method.

5.5 Results

In Figure 5.1, we show the four contributions to the left-hand side of Equation (5.2). The blue line represents the advection due to the bulk flow, the red line represents the divergence of the heat flux, the yellow line represents the pressure strain term, and the purple line represents the expansion rate. The error bars for each term decrease with radial distance and become roughly equal to the line width at $r > 0.35$ au.

On a linear scale, it is difficult to recognize the relative contribution of each term at larger radial distances. Therefore, we plot the means of these terms on a logarithmic scale in Figure 5.2. When a contribution is positive, we use a solid line. When a contribution is negative, we use a dashed line. We also plot the resulting irreversible electron thermal power density Ξ from the right-hand side of Equation (5.2). We propagate the cumulative errors to Ξ. The Ξ term decreases from $\sim 1 \times 10^{-13}$ $\mathrm{W\,m^{-3}}$ at 0.15 au to $\sim 3 \times 10^{-15}$ $\mathrm{W\,m^{-3}}$ at 0.35 au then remains roughly constant $\sim 3 \times 10^{-15}$ $\mathrm{W\,m^{-3}}$, within the error bars, from 0.35 au to 0.48 au. The advection, pressure strain, and the expansion rate follow this same decreasing trend in magnitude. The largest contribution from the left-hand side of Equation (5.2) is from the expansion $(\nabla \cdot \mathbf{u}_e)\varepsilon$, and the smallest contribution arises from the divergence of the heat flux $\nabla \cdot \mathbf{h}_e$.

The magnitude of the divergence of the heat flux is $\sim 3 \times 10^{-14}$ $\mathrm{W\,m^{-3}}$ at 0.15 au and continues to decrease to $\sim 7 \times 10^{-16}$ $\mathrm{W\,m^{-3}}$ at 0.48 au. The divergence of the heat flux is positive for $r < 0.33$ au and negative for $r > 0.33$ au. It contributes $\sim 10\%$ to Ξ for $r < 0.33$ au. The radial gradient of Ξ steepens near 0.33 au, where the divergence of heat flux changes sign.

The pressure strain term and the advection term are approximately equal in magnitude for $r > 0.35$ au, yet with opposite signs. The advection term and the pressure strain term thus largely cancel each other, so that the thermal balance is mainly determined by the competition between the remaining terms: the divergence of the heat flux and the expansion term. Ξ is positive across all explored heliocentric distances within the error bars. It drops below the contribution from the expansion

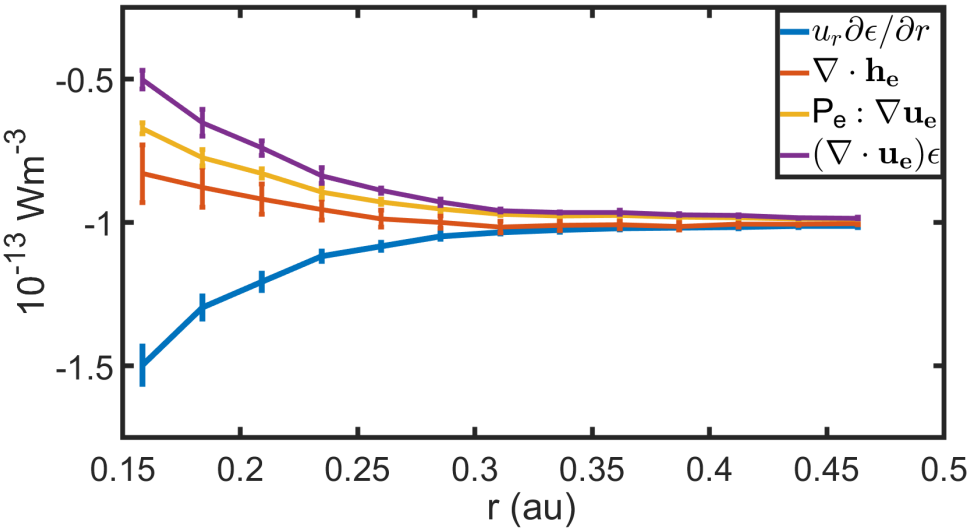

Figure 5.1: Thermal energy budget of solar wind electrons as a function of radial distance. The blue line represents the advection of the thermal energy by the bulk flow. The red line represents the divergence of the heat flux. The yellow line represents the pressure strain term. The purple line represents the expansion rate. This Figure is taken from Abraham et al. (2022b)

rate for $r > 0.3$ au.

In order to determine the polytropic index the logarithm of the scalar electron pressure as a function of the logarithm of the total electron density is shown in Figure 5.3. We fit a straight line of the form shown in Equation (5.20). From the best fitted line, we obtain $\gamma_e = 1.176$ and $C = -18.81$.

5.6 Discussion

To the best of our knowledge, this is the first work to present a description of the electron energetics in the solar wind based on comparison of data to the complete and exact second moment of the Boltzmann equation and application of the electron thermal energy budget to the inner heliosphere. The critical parameter that is evaluated in this Chapter is the irreversible electron thermal power density Ξ, which measures the spatial deposition of the thermal energy density which is needed to balance the thermal energy from thermal energy budget. If $\Xi = 0$, then the electron thermal budget can be fully governed by free-streaming effects, such as the advection of the thermal energy density by the bulk flow, divergence of the heat flux, pressure strain, or the expansion of the solar wind, without additional deposition/removal of

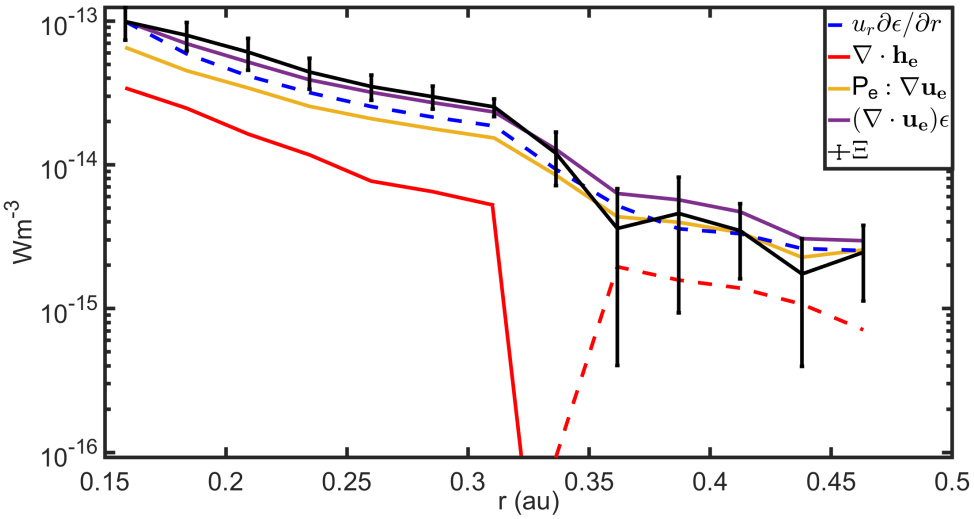

Figure 5.2: Thermal energy budget of solar wind electrons as a function of radial distance. The color scheme is the same as in Figure (5.1). The black line represents Ξ with cumulative error bars. We use solid lines when a quantity is positive and dashed lines when a quantity is negative. This Figure is taken from Abraham et al. (2022b)

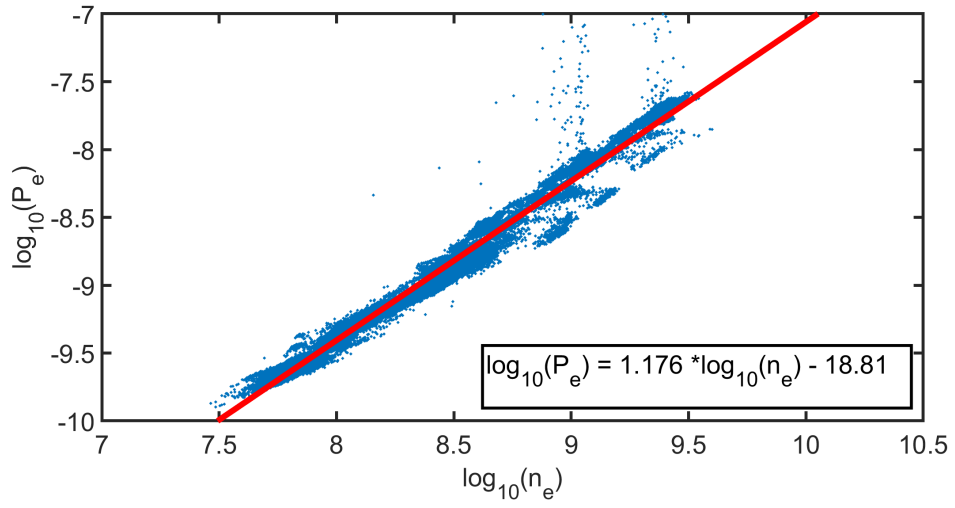

Figure 5.3: Determination of the polytropic relationship of solar wind electrons. We show total electron density as a function of thermal energy in double-logarithmic space. The red line represents the best fitted straight line given in the box in the bottom right-hand corner. This Figure is taken from Abraham et al. (2022b).

thermal energy. However, Figure 5.2 shows that Ξ is on average positive from 0.15 to 0.47 au. Therefore, the free streaming effect alone is not enough to balance the thermal energy budget of the electrons in the solar wind.

This finding suggests that additional processes act to provide thermal energy, on average, across all measured radial distances to balance the thermal budget. The magnitude of Ξ decreases with radial distance, suggesting that less such heating is required to maintain the energy balance at greater heliocentric distances. Previous energy budget studies of the electrons (Cranmer et al., 2009; Pilipp et al., 1990; Štverák et al., 2015) have concluded that there is external heating needed for the slow solar wind electrons, solely based on the divergence of the heat flux. We show that the divergence only contributes to 10% of the thermal energy budget. When we account for all the other terms in the energy budget, we find there is a source of irreversible thermal energy density for the electrons in the inner heliosphere for the slow solar wind.

We find the divergence of the heat flux is positive below 0.33 au and negative beyond 0.33 au. This degradation of the heat flux at radial distances greater than 0.33 au is in agreement with findings based on data from Helios (Štverák et al., 2015). The change in nature of the heat flux suggests the action of a mechanism that shapes the VDF so that the heat flux decreases more slowly than $\propto r^{-2}$ at distances below 0.33 au and faster than $\propto r^{-2}$ at distances beyond. PSP observations (Halekas et al., 2021; Abraham et al., 2022a) have shown that, at closest distances (< 0.2 au) from the Sun, there is little or no halo signature, but the halo signature becomes prominent with radial distances > 0.3 au. This is potentially related to the observed heat-flux behaviour.

We identify three potential mechanisms that may provide external thermal energy sources and sinks to the electron populations in the form of non-zero Ξ: turbulent heating; instabilities; and collisions. The turbulent cascade transfers energy from large scales to kinetic scales, where kinetic processes dissipate the energy in the form of heat (Breech et al., 2009; Goldstein et al., 2015; Livadiotis, 2019; Bruno and Carbone, 2013; Tu and Marsch, 1995; Schekochihin et al., 2009; Franci

et al., 2022). This form of turbulent dissipation leads to an irreversible deposition of energy from electromagnetic fields to electron thermal energy. Empirical studies suggest that a significant amount ($\sim 40\%$) of the turbulent energy is dissipated into the electron populations in the inner heliosphere (Cranmer et al., 2009; Shoda et al., 2021). Such a contribution, if dominant in the overall irreversible power density, would lead to a positive value of Ξ, as observed here. Recent observations of the turbulence spectrum have shown a substantial change in the spectral index of the inertial-range turbulence power spectral density with heliocentric distance from -3/2 for $r < 0.3$ au to -5/3 for $r > 0.3$ au (Chen et al., 2020). This change potentially influences the deposition of turbulent energy into the electron populations and may thus potentially explain the observed change in Ξ around 0.3 au. In this case, turbulent heating can be considered a potentially significant contributor to the electron thermal energy budget at the heliocentric distances explored in our study. The potential dissipation channels for turbulent heating arise from kinetic Alfvén waves (Bale et al., 2005; Schekochihin et al., 2009; Malara et al., 2019; Zhou et al., 2022) magnetic switchbacks (Bale et al., 2021; Shoda et al., 2021), shear that arises from stream-stream interaction (Coleman, 1968), or nonlinear dissipation in current sheets (Sundkvist et al., 2007; Bandyopadhyay et al., 2021). However, it is outside the scope of this study to distinguish between these kinetic channels of dissipation for turbulent heating.

Deviations from thermodynamic equilibrium can also create and drive fluctuations in the electric and magnetic fields in the form of plasma instabilities. As these instabilities grow, they interact with the electrons, leading to a change in the electron VDF, such that the drivers of the instability are reduced and the VDF returns to a stable state (Feldman et al., 1976; Schwartz, 1980; Štverák et al., 2015; Verscharen et al., 2019; Jeong et al., 2020; Verscharen et al., 2022; Jeong et al., 2022a). For example, instabilities drive by temperature anisotropy act on the electron VDF and drive the VDF towards isotropy (Verscharen et al., 2022). Likewise, instabilities driven by heat flux reduce the heat flux in the VDF (Gary et al., 1975; López et al., 2020). Instabilities generally transfer energy from the particles into

the growing electromagnetic fluctuations. Therefore, we might expect a reduction in thermal energy during the time of the growth of instabilities. In our energetics framework, this would correspond to a negative contribution to Ξ. As we do not observe $\Xi < 0$ on average, our results suggest that electron-driven instabilities are not a dominant contributor to the average electron thermal energy budget in terms of the irreversible electron thermal power density. We note, however, that this finding does not rule out the existence and relevance of electron-driven instabilities altogether. It is merely a statement regarding their relative importance in the energy budget according to Equation (5.2). Since the magnitude of Ξ decreases with radial distance, instabilities may be a key driver of the thermal energy budget at greater heliocentric distances (see also Jeong et al., 2022a).

Collisions can also act to heat/cool the electrons, leading to a non-zero Ξ term. For example collisions between hot protons and cold electrons heat the electrons and vice versa (Salem et al., 2003). However, the consistent difference in temperature between the protons and the electrons in the solar wind show that they are not in thermal equilibrium, which indicates that the collisional coupling between electrons and protons is weak (Feldman et al., 1975). Recent work on the heat flux in the inner heliosphere (Bale et al., 2013; Halekas et al., 2021) shows that collisions are not the dominant heat-flux regulation mechanism near the Sun.

For our data set, we find an effective polytropic index of $\gamma_e = 1.176$. This effective polytropic index is representative of the combined action of all terms accounted for in Equation (5.2). Its observed value is slightly greater than for an isothermal plasma ($\gamma_e = 1$). Our measured effective polytropic index agrees well with the predicted polytropic index of 1.17 obtained by Scudder and Olbert (1979) model for a weakly collisional plasma eVDF under compression. Some observations indicate that the solar wind electron polytropic index tends towards an isothermal profile as we go further away from the Sun (Sittler and Scudder, 1980; Arridge et al., 2009; Nicolaou et al., 2021). Note that any investigation into the polytropic behaviour must be carefully applied to the identified streamlines.

5.7 Conclusions

In this Chapter, we present a framework in which we apply fit results from spacecraft measurements to evaluate individual terms in the complete and exact electron thermal energy budget, based on the Boltzmann equation. We evaluate the average radial evolution of the thermal energy density budget in the inner heliosphere by separating the thermal energy balance between reversible and irreversible processes.

Under the assumption of steady-state, free-streaming effects of the electrons alone cannot account for the overall electron thermal energy budget across all measured distances. We find that the irreversible thermal power density Ξ remains positive from 0.155 au to 0.47 au. We show that that there is an irreversible an energy source mechanism/s that supplies the electrons with thermal energy across all radial distances explored in this study. We discuss three potential mechanisms that could be responsible for a non-zero Ξ: turbulence, instabilities, and collisions. We conclude that turbulent heating is most likely the main driver responsible for the $\Xi > 0$ on average.

We find the pressure strain term is of the same magnitude as the advection term in our energy balance. The most dominant term in the inner heliosphere ($<$ 0.33 au), however, is the expansion rate. The divergence of the heat flux only makes a $\sim 10\%$ contribution to the energy balance at distances between 0.15 and 0.33 au. The divergence of the heat flux is also positive in this distance range. Beyond 0.33 au, however, the divergence of the heat flux becomes negative, which agrees with previous observations from Helios beyond 0.3 au (Štverák et al., 2015). This indicates that there is fundamental change in processes that define the shape of the electron VDF at around 0.33 au. We also find that the effective electron polytropic index is 1.176 as a result of all contributions to Equation (5.2), which indicates that heating is present at all distances.

After quantifying the thermal energy budget of the electrons, the next natural step is the examination of the irreversible kinetic processes that lead to the observed deposition of electron thermal energy. In the future, it would be worthwhile to

identify and quantify the processes that provide the thermal energy across different distances. Likewise, it would be interesting to identify and quantify the processes that define the sign of the divergence of heat flux within and beyond 0.33 au by examining the interplay of heat-flux generating processes (e.g., double-adiabatic focusing) and heat-flux destroying processes (e.g., instabilities) is likely responsible for this behaviour.

In the future, alignments between Parker Solar Probe, Solar Orbiter, and potentially other spacecraft will help by providing measurements of solar wind plasma from the same source at different distances. Analysis of such events will help us quantify a scale of the influence of the temporal variability of the thermal energy budget without having to rely on the statistical consistency of multiple wind streams.

Chapter 6

Modelling the Sunward Electron Deficit in the Solar Wind: An insight into the Sun's global electric interplanetary potential

6.1 Introduction

As discussed in Chapter 2, exospheric models describe how the acceleration of the solar wind is driven by the strong electron thermal pressure gradient which arises from the mass difference between the electrons and protons. To maintain quasi-neutrality in the plasma and the zero current condition, it gives rise to an interplanetary ambipolar electric field (Lemaire and Scherer, 1971; Jockers, 1970; Maksimovic et al., 1997, 2001; Zouganelis et al., 2004). Assuming no particles arrive from infinity, the exospheric model predicts this ambipolar electric field will modify the electron distribution function, such that a sharp truncation should appear in the sunward direction called an electron deficit, as shown in Figure 2.7 (Maksimovic et al., 2001).

Recent observations from PSP, introduced in Chapter 4, confirm the existence of an electron deficit signature (Halekas et al., 2020, 2021; Berčič et al., 2020, 2021; Abraham et al., 2022a). Observations also show that, below 0.15 au, 60 – 80 % of

the eVDFs have a strong deficit signature (Halekas et al., 2021). However, this reduces to only a few percent above 0.3 au (Owen et al., 2022). Thus, the deficit is a more prevalent signature in the eVDF closer to the Sun. Accurately modelling the eVDF would better reveal any implications on thresholds for instabilities (see Verscharen et al. (2022) and references therein) and for the thermal energy budget, such as that presented in Chapter 5 (Abraham et al., 2022b). Understanding the structure of the deficit would reveal the strength and nature of the global interplanetary electric potential field (Berčič et al., 2020, 2021), which it turns has implications for acceleration of the solar wind.

The deficit is a feature which affects the overall shape of the eVDF and introduces an additional field aligned reflection asymmetry to the typical eVDF shape. If such modifications are strong, then they can drive the eVDF out of local thermodynamic equilibrium and give rise to a deficit-driven instability (Berčič et al., 2021; Verscharen et al., 2022). The nature of such an instability is currently being actively studied. Berčič et al. (2021) hypothesise that the deficit creates conditions that are able to create waves with frequencies between the ion and electron gyrofrequency through resonant interactions and erase the deficit signature. Waves in this frequency band is called the whistler waves (Berčič et al., 2021; Stix, 1992; Verscharen et al., 2022)

To date, the presence of the deficit feature has been observed but is poorly modelled, we are motivated in this Chapter to fit the electron deficit using a sigmoid function as discussed in Section 6.2. In Section 6.3 we test the hypothesis that the deficit signature can instigate resonant wave particle interactions with whistler waves by deriving contour of marginally stability. In Section 6.5, we discuss our results and conclude with a summary of our findings, with ideas for future work presented in Section 6.6.

6.2 Electron deficit

We perform a case study of the deficit, in which we examine the eVDF measured by PSP on 7^{th} June 2020 at 14:44 UT which exhibits a representative signature of

the local electron deficit at 0.13 au. The deficit is a feature predominately observed below 0.15 au (Halekas et al., 2021) and our findings in Chapter 4 show that eVDFs below 0.15 au can be fully described with a core and strahl population. Generally the strahl population points in the anti-sunward direction (Graham et al., 2017) and according to the exospheric model, the deficit is a signature only seen in the sunward direction. In this description, the deficit is a signature that is prevalent in the core population. Panel A of Figure 6.1, shows a 1D cut of the observed eVDF along the sunward direction.

The black curve represents the measured PSP eVDF and the green curve represents the bi-Maxwellian fit for the core from the work presented in Chapter 4. The purple arrow points at the deficit signature in the observed eVDF of a cut along the sunward direction. It can be noted that the deficit in the observations shows a more gradual departure from the Maxwellian distribution than exospheric model predictions, shown in Figure 2.7. Panel B of Figure 6.1 shows the fitted distribution divided by the measured distribution. The deficit signature is such that f rapidly decreases below the fitted description. Thus, it would appear as yellow (values > 1) in Panel B of Figure 6.1. Sections of the plot in Panel B appearing as blue (values $= 1$) indicate the parts of the measured eVDF that fit well with the overall fitted model. Unlike the prediction of the deficit in exospheric model where the deficit only appears in the sunward direction, we note from panel B that the deficit takes a crescent shape which indicates this signature is not purely along the sunward direction. In addition, we note the ratio decreases to 1 with increasing pitch angle, up to 52.5° from the sunward direction. Thus, this deficit signature becomes less prominent with increasing pitch angle.

6.2.1 Deficit model

To better capture the crescent shape of the deficit, we model the deficit as a function of velocity in each pitch angle with a sigmoid function, f_D, of the form:

$$f_D = \frac{1}{1 + e^{\frac{\pm}{-}\frac{V - V_\phi}{V_{\phi\omega}}}} \tag{6.1}$$

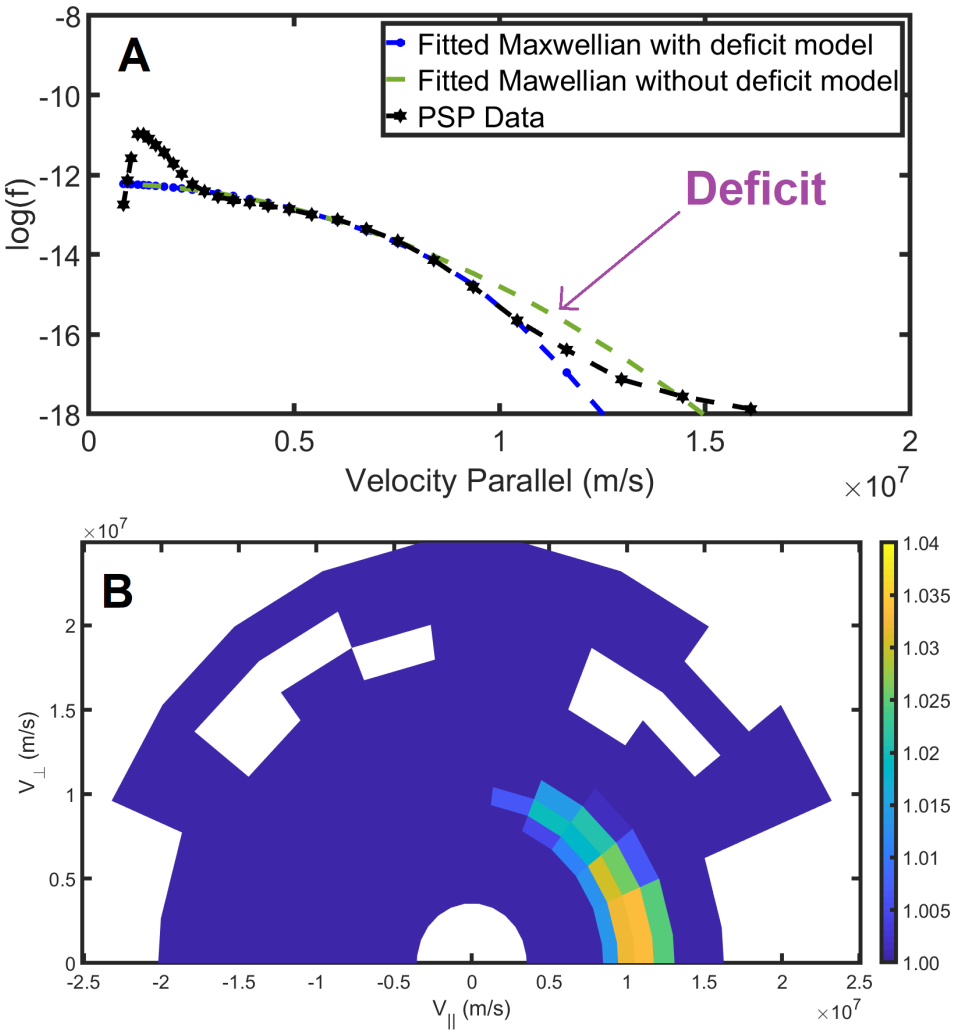

Figure 6.1: Panel A shows a cut off the eVDF along the sunward direction. The black dashed curve with stars represents the measured PSP distribution. The green curve represents the fitted Maxwellian core from Chapter 4. The purple arrow represents deficit signature. The dashed blue curve represents the core Maxwellian model with the deficit model. The x-axis is velocity and the y-axis is log(f). Panel B shows the fitted core model normalised to measured eVDF. The colorbar represents the ratio of the fitted model with to the PSP observed VDF, such that any truncation from the fitted model will have values greater than 1 and tends towards yellow and the rest of the eVDF have values 1 and appear as blue.

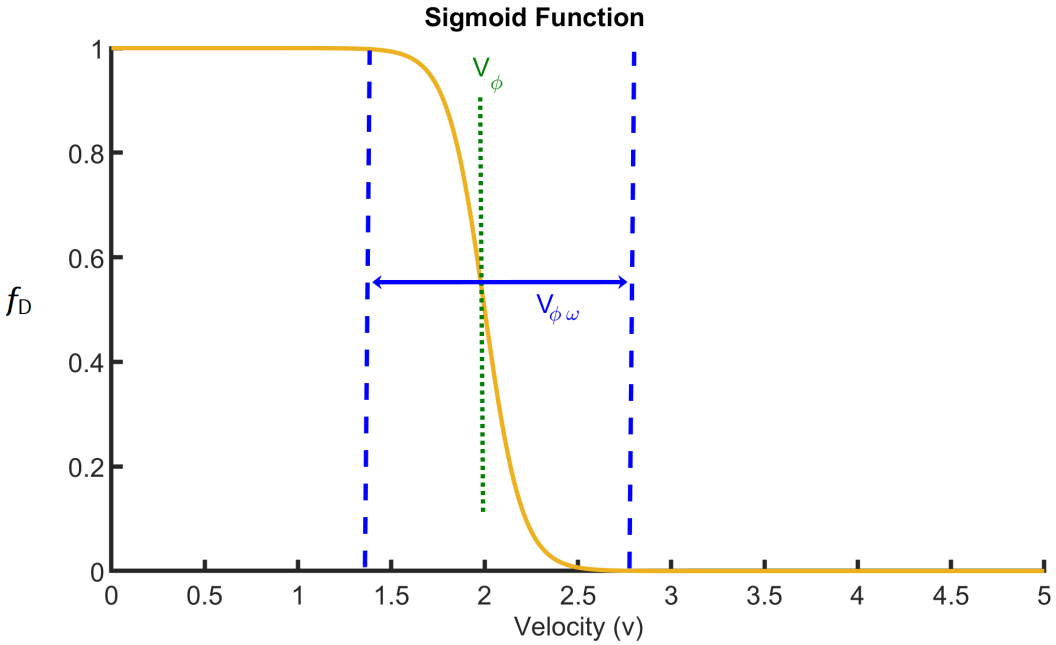

Figure 6.2: A representation of a sigmoid function. The x-axis velocity and the y-axis is the output of the sigmoid function. The green line represents the location of the cut-off velocity of the deficit, V_ϕ the blue arrow represents the width of the deficit, $V_{\phi\omega}$.

where V_ϕ is the cut-off velocity of the deficit and $V_{\phi\omega}$ is the width of the deficit in velocity space. The sigmoid function is a smooth analytical approximation of a step function and maps any value of the velocity domain to a number between 0 and 1, as shown by Figure 6.2. The Figure shows that the sigmoid function tends to zero for velocity greater than V_ϕ, tends to 1 when velocities are less than V_ϕ and the value is 0.5 at V_ϕ. If $V_{\phi\omega}$ tends to zero, the shape of the sigmoid approaches a step function. In this model, the fit parameters are $V_{\phi\omega}$ and V_ϕ.

To apply the deficit model proposed above to our fitting routine, we multiply our deficit model with the fitted core electron distribution obtained in Chapter 4 to describe the total measured eVDF envelope at each pitch angle:

$$f_e = f_c f_D \tag{6.2}$$

6.3 Resonant Interactions

To test the hypothesis proposed by Berčič et al. (2021) we derive the curve that correspond to a marginally stable state between the deficit and whistler waves (Berčič et al., 2021; Verscharen et al., 2022). We postulate that if the deficit signature resonantly interacts to drive the whistler instability, then the location of the deficit cut-off velocity, V_ϕ, will not follow the curve of marginal stability. An interaction of this nature would allow for energy exchange between waves and electrons, or vice versa, only if the resonant condition is satisfied (Stix, 1992):

$$V_{phase} = V_{||} + \frac{|\Omega|}{k_{||}} \tag{6.3}$$

where $V_{||}$ parallel velocity of the particle, Ω is the electron gyrofrequency and $k_{||}$ is the wave number. The phase speed of a whistler wave can be approximated as (Verscharen et al., 2022):

$$V_{phase} = k_{||} d_e^2 |\Omega| \tag{6.4}$$

where d_e is the electron inertial length. Equating Equation (6.3) with (6.4), we obtain the following quadratic equation:

$$k_{||}^2 - \frac{V_{||} k_{||}}{d_e^2 |\Omega|} - \frac{1}{d_e^2} = 0 \tag{6.5}$$

Solving for, $k_{||}$ we obtain :

$$k_{||} = \frac{V_{||}}{2 d_e^2 |\Omega|} + \sqrt{\left(\frac{V_{||}}{2 d_e^2 |\Omega|}\right)^2 + \frac{1}{d_e^2}} \tag{6.6}$$

Substituting Equation (6.6) into (6.4) we obtain the phase speed in terms of the $V_{||}$:

$$V_{phase} = \frac{V_{||}}{2} + \sqrt{\left(\frac{V_{||}}{2}\right)^2 + d_e^2 |\Omega|^2} \tag{6.7}$$

We express $V_\perp$ in terms of $V_{||}$ for the instability as:

$$V_\perp = \sqrt{D - (V_{||} - V_{phase})^2} \tag{6.8}$$

where D is a constant. Equation (6.8) describes the contours that are locally circular around V_{phase}. However, they are not circular overall since V_{phase} depends on $V_{||}$ according to Equation (6.7). The contour represent the marginally stable state of the resonant interaction between the deficit and whistler waves.

6.4 Results

Panel A of Figure 6.1 shows an example of the revised fitting routine along the sunward direction. The black dashed curve with stars represents the measured PSP eVDF and the green dashed curve represents the fitted VDF. The core Maxwellian fits well with the measured distribution at lower energies, but with increasing energies the measured eVDF rapidly declines in f compared with the bi-Maxwellian core. Our model for the deficit, shown in blue, describes the deficit feature well and this is reflected in the reduced χ^2 value improving from 1.77 to 1.03 when including the deficit signature in the fit function.

We apply this method to each pitch angle and plot the variation the V_ϕ, $V_{\phi\omega}$ and energy in pitch angle space in Figure 6.3. Panel A shows the variation of V_ϕ and $V_{\phi\omega}$ for each pitch angle where the deficit is present. The deficit signature for this example is only present up to $\sim 52.5^\circ$ from the sunward direction. We note that V_ϕ increases and $V_{\phi\omega}$ decreases with increasing pitch angle. Panel B shows that the energy of the cut-off increases with increasing pitch angle, from 107 eV at 7.5° to 250 eV at 52.5°.

In Figure 6.4, we test the hypothesis that the deficit signature can drive whistler instability through resonant interaction. We plot the contours of marginal stability described in Equation 6.8 as pink dotted lines overlaid with the black dots represents V_ϕ in each pitch angle obtained from our model. Qualitatively, the V_ϕ location follows the marginally stable contour, indicating that the deficit feature we examined has achieved marginal stability with whistler waves.

6.5 Discussion

To the best of our knowledge, this is the first work to present an analytical description of the shape of the electron deficit using the deficit cut off location, V_ϕ, and

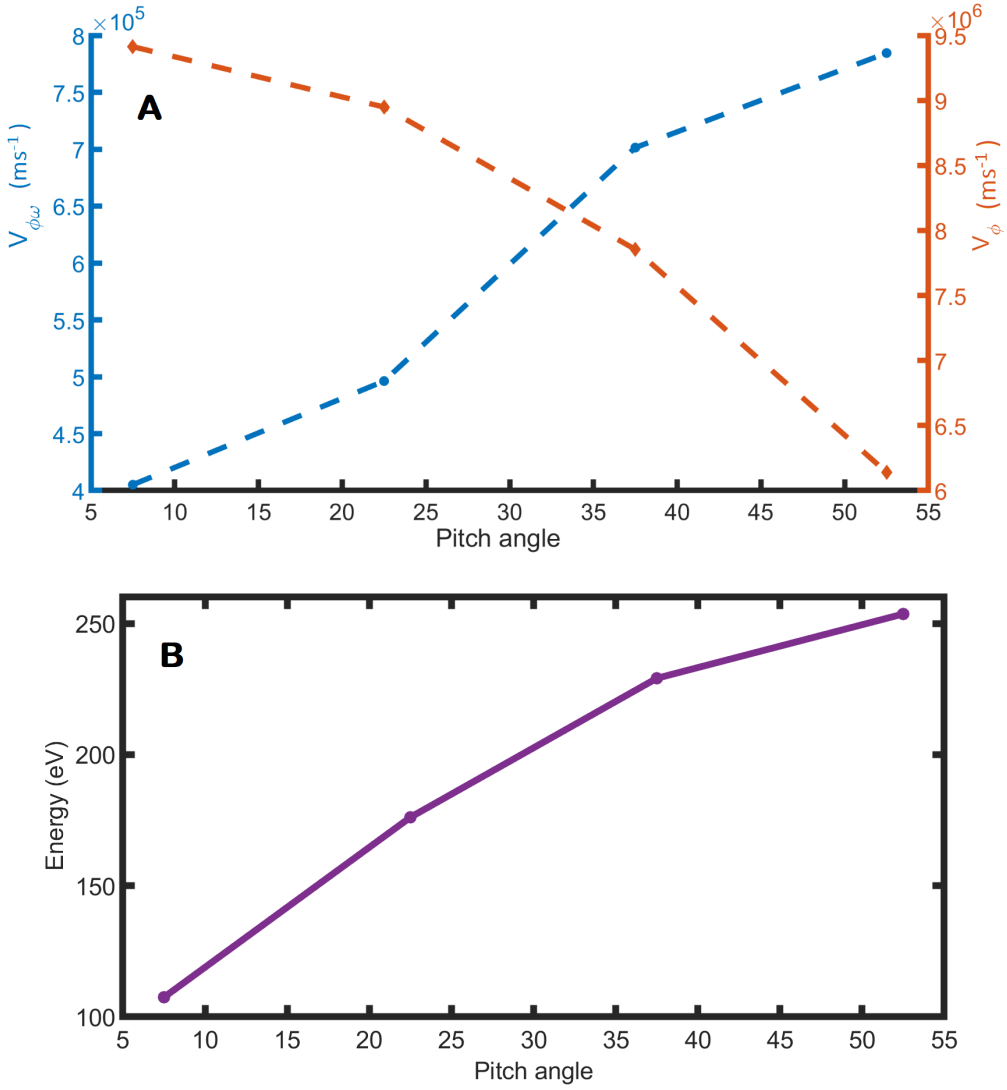

Figure 6.3: The dashed orange line on Panel A shows the variation of V_ϕ (right side y-axis) with pitch angle. The dashed blue line on Panel A shows the variation of $V_{\phi\omega}$ (left hand y- axis) with pitch angle.Panel B shows the variation of energy (eV) associated with V_ϕ respect to the pitch angle.

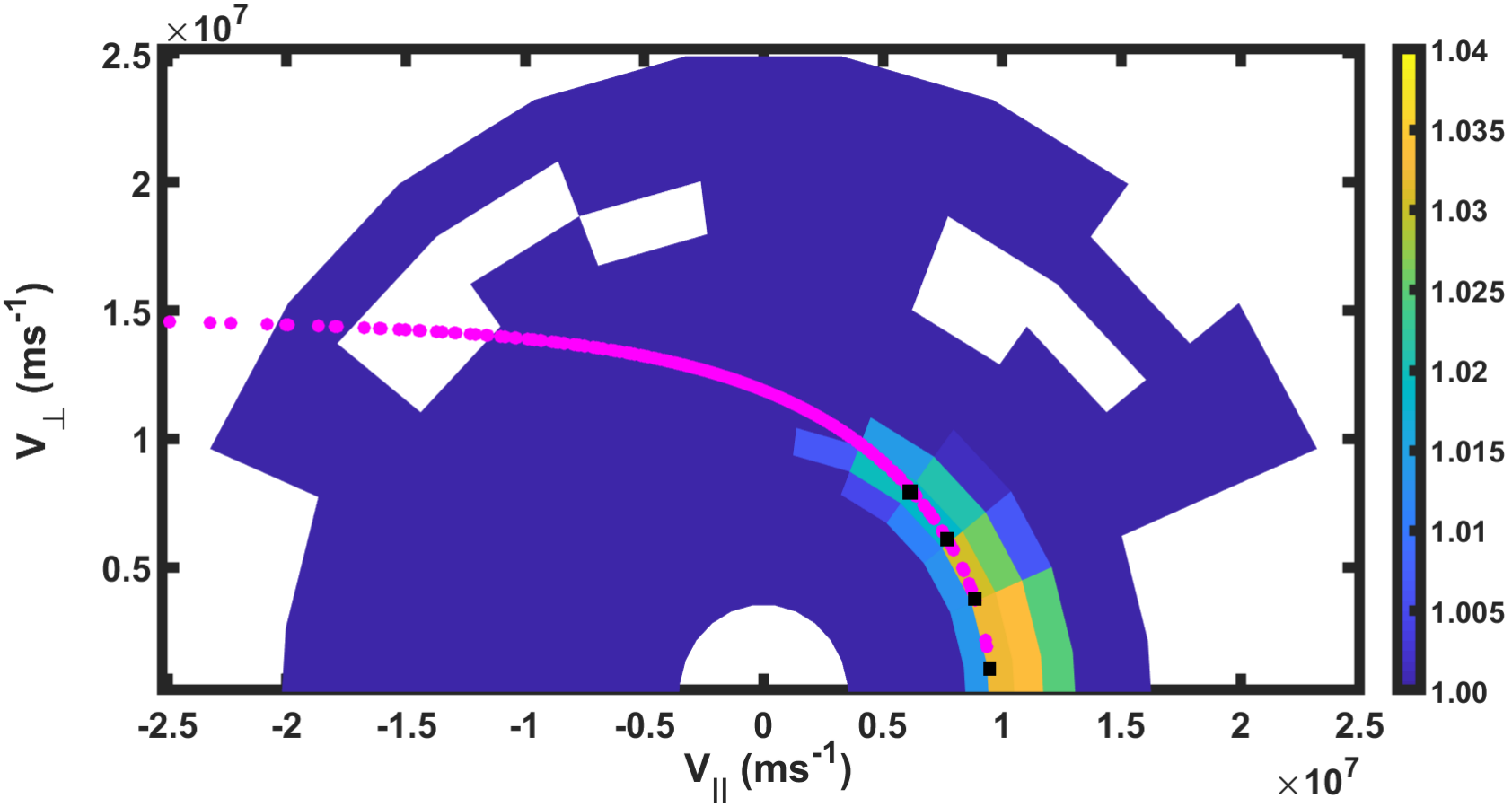

Figure 6.4: The background of the Figure is the same as Panel B of Figure 6.1. The black dots represent the location of local electron deficit cut off point in each pitch angle obtained from our model. The pink dashed contour represents the contour of marginal stability for whistler instability.

deficit width, $V_{\phi\omega}$, in each pitch angle. As discussed in 2.4, for a purely collisionless scenario, the deficit appears as a sharp truncation of the eVDF, i.e. $V_{\phi\omega} = 0$, and only in the sunward direction. Our results show that the observed nature of the deficit is different from the exospheric model predictions. We show that the sunward deficit takes a crescent shape in velocity space, which shows that the deficit is not only a vertical cut at a fixed speed in the sunward direction but undergoes non-adiabatic pitch angle diffusion. For our model, the deficit has a pitch angle width of $\sim 52.5^{\circ}$ around the sunward direction.

Furthermore, Panel A in Figure 6.3 shows that the width of the deficit, $V_{\phi\omega}$, in each pitch angle is non-zero and that $V_{\phi\omega}$ increases with pitch angle from $4.1\times 10^5\ m\ s^{-1}$ at 7.5° to $7.91 \times 10^5\ m\ s^{-1}$ at 52.5°. This indicates that truncation of the deficit signature is less abrupt with increasing pitch angle from the sunward direction. Kinetic simulations have shown that Coulomb collisions can be attributed to a non-zero $V_{\phi\omega}$ (Berčič et al., 2020; Landi et al., 2012).

In addition, Panel A of Figure 6.3 shows that the cut-off velocity, V_{ϕ}, decreases with increasing pitch angle along the sunward direction from $6.2 \times 10^6\ m\ s^{-1}$ at 52.5° to $9.46 \times 10^6\ m\ s^{-1}$ at 7.5°. As mentioned in Chapter 2 the V_{ϕ} location can be used to determine the interplanetary electric potential between the corona and the heliosphere. The variation in V_{ϕ} makes the determination of the electric potential complicated, as it raises an important question as to which value of V_{ϕ} should be used to calculate the electric potential. As the variation in the V_{ϕ} corresponds to a range in the electric potential from 110 - 250 V. Identifying the correct value is critical to determining the electric field, which in turn is needed to explain the acceleration of the solar wind (Berčič et al., 2021). The variations of V_{ϕ} and $V_{\phi\omega}$ of the deficit indicate that the observed signature has most likely undergone a complex interplay of wave-particle interactions, Coulomb collisions, magnetic mirror force and electrostatic reflection. In addition, we also note in panel B of Figure 6.3, that the associated energy of the deficit location decreases with pitch angle, from 250 eV at 52.5° to 110 eV at 7.5°, further complicating the determination of the electric potential.

The deficit signature represents a deviation of the eVDF from thermodynamic equilibrium and can thus create conditions for instabilities to arise (Dum et al., 1980; Marsch, 2006; Verscharen et al., 2022). Berčič et al. (2021) theorise that the sunward deficit can create conditions in which electrons near V_ϕ can resonate with whistler waves, such that the electrons lose their kinetic energy and the waves grow whilst erasing the deficit signature. To test this hypothesis, we derive the contours that correspond to marginal stability for whistler waves, as shown by Equation (6.8). In Figure 6.4, the pink curve represents the contour of marginal stability and the black dots represent the position of the electron deficit at each pitch angle we obtained from our model. Our observations show that the V_ϕ positions in each pitch angle follow the derived contour of marginal stability, which indicates that the deficit feature we have examined has been relaxed by the whistler instability. It is unlikely that we would observe any whistler instability in action in this dataset, predominately because the whistler instability occurs on time scales of a second or less, (Stix, 1992), while the PSP eVDF is integrated just under 14 seconds. Generally, electron instabilities act on the eVDF in such a way the eVDF achieves marginal stability with the instability (Stix, 1992; Verscharen et al., 2022). This depicts a scenario where the observed deficit of the eVDF may have driven whistler instability and have achieved a marginally stable state before the time a eVDF has been observed by PSP. Nevertheless, the presence of the deficit even in this stable configuration with whistler instability indicates that the whistler instability alone is not sufficient to erase the deficit signature completely.

6.6 Conclusions

In this Chapter, we describe the first model of the electron deficit in each pitch angle direction, using V_ϕ and $V_{\phi\omega}$ as fit parameters. Our results show that the shape of the deficit is different from the expectations of a purely collisionless exospheric case such as that predicted in Figure 2.7. We also show that the variations in V_ϕ and $V_{\phi\omega}$ indicate that the electron deficit has been processed by a combination of Coulomb collisions, mirror force, instabilities, and reflection due to the electric potential. We

also argue that the processed nature of the electron deficit is reflected in the variation of V_ϕ and makes the determination of the electrostatic potential more complicated, as the selection of the V_ϕ can give an electric potential value from 110 to 250 V. We raise the need for a more detailed study into the nature of the electric potential under the influence of Coulomb collisions, mirror force, instabilities, and reflection due to the electric potential.

In this study, we also tested the hypothesis proposed by Berčič et al. (2021), that the deficit signature drives whistler instability and in the process erases the deficit signature. The case study we examined of the deficit signature is shown to be in marginal stable configuration with whistler waves. This means for our case, the deficit does not presently drive the whistler instability. We also note that it is unlikely that we would observe any whistler instability in action in this PSP dataset predominately because the whistler instability occurs on timescales that are a second or less, (Stix, 1992) meanwhile the eVDF is integrated under 14 seconds. We also note, that an eVDF that has been processed by whistler instability should follow the contour of marginal stability. To test this hypothesis, it may be beneficial to undertake this analysis with the burst mode eVDF dataset provided by the Solar Orbiter's ESAs, which has a measurement cadence of 0.125 seconds (Owen et al., 2020). The next natural step to follow this study is to run a statistical study of V_ϕ and $V_{\phi\omega}$ across different radial distances to gain insight into the evolution of the electron deficit and to better understand the structural evolution of the electrostatic potential. As mentioned above, the deficit is a signature more prevalent below 0.15 au and becomes less significant past 0.3 au (Halekas et al., 2021) which coincides with the radial distance in which the halo grows, as demonstrated in Chapter 4. This might indicate that the processes that form the halo may also reshape the deficit signature. Finally, the presence of the deficit in the eVDF implies the typical eVDF model description we have given in Chapter 4 needs to be generalised to account for the possible presence of a deficit, especially below 0.15 au (Halekas et al., 2021). In a follow-up study, we would like to examine the impact the deficit has on the macroscopic properties of the electron populations and associated ramifications to

the thermal energy budget that we derived in Chapter 5.

Chapter 7

General Conclusions and Future Work

7.1 Preface

In this thesis, we present three chapters containing original research that each investigate aspects of the nature of solar wind electron populations in the inner heliosphere using in-situ observations. In the first study, detailed in Chapter 4, we present a statistical insight into the evolution of the electron thermal and suprathermal populations in the inner heliosphere. In the second study, detailed in Chapter 5, we develop the first framework to evaluate the exact and complete thermal energy budget of the solar wind electrons based on the second moment of the Boltzmann equation. In the third study, detailed in Chapter 6, we examine a feature in the eVDF known as the electron deficit. In this Chapter, we first summarise our key conclusions from these three studies in Section 7.2. We then conclude this Chapter with section 7.3, where we describe ideas for potential future work to build on the results presented in this thesis.

7.1.1 Key Outcomes

Below, we highlight the key outcomes of this thesis:

- Coronal electron temperature can be inferred from the strahl parallel temperature

- Discovery of the *halo strahl cross over* point
- Evidence for the growth of the suprathermal population from 0.13 to 0.2 au due to the rise in halo population
- Scattering of the strahl cannot solely form the halo below 0.2 au.
- At 0.13 au teh eVDF can be well described with a core and a strahl model
- Development of the first framework that presented the complete and exact electron energetics based on PSP observations.
- Electrons have an external source of irreversible heating from 0.13 au to 0.5 au.
- The electron deficit is processed by a combination of Coulomb collisions, mirror force, instabilities and reflection due to the ambipolar electric field.
- Whistler instability is not sufficient to erase the electron deficit signature.

7.2 General Conclusions

In the first study described in Chapter 4, we examine the radial evolution of the thermal and non-thermal electron populations in the inner heliosphere. One of our new findings is that there is an increase in the relative densities of the non-thermal particles from 0.13 to 0.3 au. This growth in the total non-thermal population is predominately due to the growth of the halo population with distance. This result provides new insight into the evolution of the non-thermal population and origins of the halo, which were previously unknown. Furthermore, this also provides evidence for the first time that the halo electron population cannot be formed purely from scattering of the strahl, as previously thought, but rather another multistage process appears to be involved in its formation. Another new finding in this study is that at the closest radial distance sampled, the eVDF can be completely described by a core and strahl model (i.e. without accounting for a halo model). This new finding gives support to the idea that the eVDF at the source region for the slow wind is likely

to be composed only of the core and the strahl population, which has significant implications for solar wind acceleration models, as discussed in Chapter 2.

In addition, we identify for the first time the *halo strahl cross over* point. This point is defined as the radial distance where the halo and strahl densities are equal. Our results show that below the *halo strahl cross over* point, most of the suprathermal population moves in a beam along the magnetic field, while above this point most of the suprathermal population is present at all pitch angles. This point may be important for understanding the evolution and structuring of the non-thermal population in velocity space, adding a new element to the framework for of examining the suprathermal populations. Finally, in this first original study, we discover that the average strahl parallel temperature stays approximately constant with radial distance. This indicates that the strahl parallel component retains information on the source region temperature and is less affected by transport processes.

In the second study described in Chapter 5, we develop, for the first time, a novel framework that allows us to assess the complete and exact description of the solar wind electron thermal energy budget using in situ observations. Our observations suggest that there must be an irreversible source of thermal energy for the electrons across all the radial distances sampled. However, the impact of this source on the thermal energy balance decreases with radial distance. Previous studies have failed to capture the complete thermal energy balance because they focused solely on certain aspects individually, like for example the divergence of heat flux (Pilipp et al., 1990; Štverák et al., 2009). Our study reveals that the divergence of the heat flux accounts for only 10 % of the total thermal energy budget. We also argue that the changes in thermal energy gradients at a heliocentric distance of ~ 0.33 au could indicate that there is a fundamental change in the processes that define the shape of the eVDF at this distance. The heating profiles for slow solar wind that we have presented yield an effective polytropic index of 1.17. This indicates that the slow solar wind is closer to an isothermal state than to an adiabatic state.

In the final study described in Chapter 6, we examine a feature that is prevalent in eVDFs at small heliocentric distances, called the electron deficit. Ours is the first

study to model the shape of the electron deficit with an analytical expression. We show that the deficit exhibits a crescent shape in velocity space, having a pitch angle and energy dependence. In an exospheric model the deficit is an abrupt truncation in the eVDF which corresponds to a zero deficit width,$V_{\phi\omega}$, but we show that the observed deficit width is non-zero which indicates that it is a gradual departure from the typical eVDF core model. We believe this is because the deficit signature has been processed by Coulomb collisions or other smoothing processes. The cut-off velocity, V_ϕ, is used to estimate the electric potential. We show that the associated electric potential varies with pitch angle, from 110-250 V with increasing pitch angle along the sunward direction. We conjecture that these variations in velocity space shape of the deficit indicate a combination of processes is in action, such as mirror force, electrostatic reflection, wave-particle interactions and Coulomb collisions. We also test whether our observations are consistent with the hypothesis as proposed by Berčič et al. (2021). That the deficit can drive whistler waves and in the process erase the deficit signature. We show that the electron deficit eVDF achieves marginal stability with whistler waves. We argue that this deficit driven instability of this nature alone cannot erase the deficit signature.

These three studies show that for the slow solar wind the eVDF in the near Sun region is primarily composed of core and strahl with the signature of ambipolar electric field represented as the electron deficit. We show that the deficit is not a purely collisionless signature and has been processed by a combination of Coulomb collision, mirror force, electrostatic reflection and wave-particle interactions. Our study also highlights that to maintain electron thermal energy balance there is a source of irreversible thermal energy density, but this impact decreases with radial distance. In addition, we also provide the first evidence that suggests that the origin of the halo electron population in the slow solar wind.

7.3 Future Work

7.3.1 Formation of the non-thermal halo electron population

The origin and formation of the non-thermal halo electron population is still poorly understood. In Chapter 4, we showed that at the closest observed distances the relative density of the suprathermal population is $\sim 1\%$ which then rises to approximately $\sim 10\%$ at distance > 0.25 au. This rise in the non-thermal population is predominately due to the growth of the halo population. This strongly suggests that the evolution, and potentially the origins, of the non-thermal halo population happen during solar wind expansion. The prime candidate for the halo electron population could be from the core thermal population through some complex and unknown multistage process. To evaluate if there is any coupling between the core and the halo populations, we would need to first to examine if there is any correlation between core and halo parameters across these distances. In addition, a careful examination of time series variations of these parameters, supported by magnetic field and solar wind speed measurements, can also give an insight into the nature of the process, such as turbulence or wave-particle interactions. In addition, further studying the variations in the location of the newly discovered *halo strahl cross over* point can give insight into the structuring of the non-thermal population.

7.3.2 Strahl electron population as a tracer for source region

In Chapter 4, we corroborate the idea that the strahl population can provide information about the coronal electron temperature in the parallel temperature component. One way to test this would be to use Oxygen charge state data, which provides a proxy for the electron temperature at the source region (Hefti et al., 1999; Berčič et al., 2020) and correlating it with strahl parallel temperature. PSP does not provide Oxygen charge-state ratios to validate this hypothesis, but Solar Orbiter measures Oxygen charge-state ratios from 0.3 au outwards. We suggest undertaking the analysis shown in Chapter 4 on Solar Orbiter electron data would allow us to determine the strahl parallel temperature and correlate it with the Oxygen charge state measurements on board (Owen et al., 2020) to confirm if the strahl population

can indeed be used as a tracer of the electron temperature in the source region.

7.3.3 Thermal energy density budget through the heliosphere from 0.1 - 5 au

One of the key outcomes of Chapter 5 is that there is a source of irreversible thermal energy that heats the electrons. The impact of this source decreases with radial distance up to 0.5 au. Extrapolating, these results indicate that by approximately 0.7 au, the electrons will be cooling much faster than expected for radial expansion. We could apply this framework to the electron data on board Solar Orbiter, Helios, and Ulysses to examine whether the irreversible source of thermal energy is maintained beyond Earth orbit. This would allow us for the first time to see the complete evolution of the thermal energy budget in the heliosphere out to 5 au. Future missions like IMAP (McComas et al., 2018) will allow for the evaluation of the thermal energy budget up to the outermost regions of the solar system. This can give insight into how the thermal energy is balanced in the heliosphere. Furthermore, in Chapter 5, we argue that this source is most likely related to turbulent heating at distances from 0.13 - 0.45 au. A detailed study needs to be undertaken to determine the energy transfer rate from the turbulence spectrum into the electrons. This will involve analysing the characteristics of the turbulence and correlating them with the different terms in the thermal energy budget.

7.3.4 Electrostatic potential

In Chapter 6, we discover that the deficit takes a more complex shape than the exospheric prediction described in Chapter 2. Above we show that the deficit signature is the result of processing by a combination of mirror force, Coulomb collisions, instabilities, and reflection from the electric potential well. This study shows that the typical model for the inner heliosphere eVDF needs to be reconsidered. In Chapter 6, we provide a case study to examine the nature and structure of the deficit but, to understand the evolution of the deficit, we need to undertake a detailed time series analysis in different solar wind streams. This will provide insight into how the deficit signature evolves with radial distance and how it impacts calculations of the

solar wind acceleration.

Statistical observations have shown that more than 80% of the data below 0.15 au exhibit a deficit signature (Halekas et al., 2021), but this drops to a few percent at distances greater than 0.3 au (Owen et al., 2022). This indicates that the deficit signature is most likely created (against the limiting action of Coulomb collisions and instabilities) at smaller distances. To better understand why signatures of the deficit still prevail at distances greater than 0.3 au, we propose to undertake a time series analysis using the model described in Chapter 6 for the deficit signature close to the Sun, using PSP data, and signatures of the deficit observed at distances greater than 0.3 au, using Solar Orbiter data, supported by data of the background plasma and magnetic field conditions. This will provide insight into why the signature of the electrostatic potential appears at larger distances for some solar wind streams. In the exospheric model, the location of cut-off velocity, V_ϕ, is used to determine the strength of the global electric potential.

To better understand the shape and nature of the electric potential well around the Sun, we propose undertaking a detailed statistical study of the deficit cut-off velocity, V_ϕ, and deficit width, $V_{\phi\omega}$, from 0.1 au to 1 au using PSP and Solar Orbiter. From the location of V_ϕ in velocity space, as discussed in Chapter 2, we can determine the electric potential. From the electric potential measurement, we can calculate the electrostatic contribution to the acceleration of the solar wind using the same framework described by Berčič et al. (2021).

Bibliography

Abraham, J. B., Owen, C. J., Verscharen, D., Bakrania, M., Stansby, D., Wicks, R. T., Nicolaou, G., Whittlesey, P. L., Rueda, J. A. A., Jeong, S.-Y., and Berčič, L. (2022a). Radial evolution of thermal and suprathermal electron populations in the slow solar wind from 0.13 to 0.5 au: Parker solar probe observations. *The Astrophysical Journal*, 931(2):118.

Abraham, J. B., Verscharen, D., Wicks, R. T., Rueda, J. A. A., Owen, C. J., Nicolaou, G., and Jeong, S.-Y. (2022b). Thermal energy budget of electrons in the inner heliosphere: Parker solar probe observations. *The Astrophysical Journal*, 941(2):145.

Agudelo Rueda, J. A. (2022). *Characterising 3D Small-scale Reconnection in Kinetic Simulations of Space Plasma Turbulence*. PhD thesis, UCL (University College London).

Agudelo Rueda, J. A., Verscharen, D., Wicks, R. T., Owen, C. J., Nicolaou, G., Germaschewski, K., Walsh, A. P., Zouganelis, I., and Domínguez, S. V. (2022). Energy transport during 3d small-scale reconnection driven by anisotropic plasma turbulence. *arXiv preprint arXiv:2208.02350*.

Anderson, B. R., Skoug, R. M., Steinberg, J. T., and McComas, D. J. (2012). Variability of the solar wind suprathermal electron strahl. *Journal of Geophysical Research: Space Physics*, 117(A4).

Arridge, C. S., McAndrews, H. J., Jackman, C. M., Forsyth, C., Walsh, A. P., Sittler, E. C., Gilbert, L. K., Lewis, G. R., Russell, C. T., Coates, A. J., Dougherty, M. K.,

Collinson, G. A., Wellbrock, A., and Young, D. T. (2009). Plasma electrons in Saturn's magnetotail: Structure, distribution and energisation. , 57(14-15):2032–2047.

Arthur, D. (2007). k-means++ : The advantages of careful seeding. *Proceedings of the eighteenth annual ACM-SIAM symposium on Discrete algorithms*, pages 1027–1035.

Aschenbrenner, H. (1936). Eine anordnung zur regisrierung rauscher magnetischer storungen. *Hochfrequenztechnik und Elektoakustik*, 47(6):177–181.

Bakrania, M. R., Rae, I. J., Walsh, A. P., Verscharen, D., Smith, A. W., Bloch, T., and Watt, C. E. J. (2020). Statistics of solar wind electron breakpoint energies using machine learning techniques. *A&A*, 639:A46.

Bale, S. D., Goetz, K., Harvey, P. R., Turin, P., Bonnell, J. W., Dudok de Wit, T., Ergun, R. E., MacDowall, R. J., Pulupa, M., Andre, M., Bolton, M., Bougeret, J. L., Bowen, T. A., Burgess, D., Cattell, C. A., Chandran, B. D. G., Chaston, C. C., Chen, C. H. K., Choi, M. K., Connerney, J. E., Cranmer, S., Diaz-Aguado, M., Donakowski, W., Drake, J. F., Farrell, W. M., Fergeau, P., Fermin, J., Fischer, J., Fox, N., Glaser, D., Goldstein, M., Gordon, D., Hanson, E., Harris, S. E., Hayes, L. M., Hinze, J. J., Hollweg, J. V., Horbury, T. S., Howard, R. A., Hoxie, V., Jannet, G., Karlsson, M., Kasper, J. C., Kellogg, P. J., Kien, M., Klimchuk, J. A., Krasnoselskikh, V. V., Krucker, S., Lynch, J. J., Maksimovic, M., Malaspina, D. M., Marker, S., Martin, P., Martinez-Oliveros, J., McCauley, J., McComas, D. J., McDonald, T., Meyer-Vernet, N., Moncuquet, M., Monson, S. J., Mozer, F. S., Murphy, S. D., Odom, J., Oliverson, R., Olson, J., Parker, E. N., Pankow, D., Phan, T., Quataert, E., Quinn, T., Ruplin, S. W., Salem, C., Seitz, D., Sheppard, D. A., Siy, A., Stevens, K., Summers, D., Szabo, A., Timofeeva, M., Vaivads, A., Velli, M., Yehle, A., Werthimer, D., and Wygant, J. R. (2016). The FIELDS Instrument Suite for Solar Probe Plus. Measuring the Coronal Plasma and Magnetic Field, Plasma Waves and Turbulence, and Radio Signatures of Solar Transients. *Space Sci. Rev.*, 204(1-4):49–82.

Bale, S. D., Horbury, T. S., Velli, M., Desai, M. I., Halekas, J. S., McManus, M. D., Panasenco, O., Badman, S. T., Bowen, T. A., Chandran, B. D. G., Drake, J. F., Kasper, J. C., Laker, R., Mallet, A., Matteini, L., Phan, T. D., Raouafi, N. E., Squire, J., Woodham, L. D., and Woolley, T. (2021). A solar source of alfvé nic magnetic field switchbacks: In situ remnants of magnetic funnels on supergranulation scales. *The Astrophysical Journal*, 923(2):174.

Bale, S. D., Kellogg, P. J., Mozer, F. S., Horbury, T. S., and Reme, H. (2005). Measurement of the Electric Fluctuation Spectrum of Magnetohydrodynamic Turbulence. *Phys. Rev. Lett.*, 94(21):215002.

Bale, S. D., Pulupa, M., Salem, C., Chen, C. H. K., and Quataert, E. (2013). Electron Heat Conduction in the Solar Wind: Transition from Spitzer-Härm to the Collisionless Limit. *Astrophys. J. Lett.*, 769(2):L22.

Bandyopadhyay, R., Chasapis, A., Matthaeus, W. H., Parashar, T. N., Haggerty, C. C., Shay, M. A., Gershman, D. J., Giles, B. L., and Burch, J. L. (2021). Energy dissipation in turbulent reconnection. *Physics of Plasmas*, 28(11):112305.

Baumjohann, W. and Treumann, R. (2012). *Basic Space Plasma Physics - Revised Edition*.

Berčič, L., Larson, D., Whittlesey, P., Maksimović, M., Badman, S. T., Landi, S., Matteini, L., Bale, S. D., Bonnell, J. W., Case, A. W., de Wit, T. D., Goetz, K., Harvey, P. R., Kasper, J. C., Korreck, K. E., Livi, R., MacDowall, R. J., Malaspina, D. M., Pulupa, M., and Stevens, M. L. (2020). Coronal electron temperature inferred from the strahl electrons in the inner heliosphere: Parker solar probe and helios observations. *The Astrophysical Journal*, 892(2):88.

Berčič, L., Verscharen, D., Owen, C. J., Colomban, L., Kretzschmar, M., Chust, T., Maksimovic, M., Kataria, D. O., Anekallu, C., Behar, E., Berthomier, M., Bruno, R., Fortunato, V., Kelly, C. W., Khotyaintsev, Y. V., Lewis, G. R., Livi, S., Louarn, P., Mele, G., Nicolaou, G., Watson, G., and Wicks, R. T. (2021). Whistler

instability driven by the sunward electron deficit in the solar wind - high-cadence solar orbiter observations. *A&A*, 656:A31.

Bertschinger, E. and Meiksin, A. (1986). The Role of Heat Conduction in the Cooling Flows of Galaxy Clusters. *Astrophys. J. Lett.*, 306:L1.

Berčič, L., Maksimović, M., Halekas, J. S., Landi, S., Owen, C. J., Verscharen, D., Larson, D., Whittlesey, P., Badman, S. T., Bale, S. D., Case, A. W., Goetz, K., Harvey, P. R., Kasper, J. C., Korreck, K. E., Livi, R., MacDowall, R. J., Malaspina, D. M., Pulupa, M., and Stevens, M. L. (2021). Ambipolar electric field and potential in the solar wind estimated from electron velocity distribution functions. *The Astrophysical Journal*, 921(1):83.

Bittencourt, J. A. (2004). *Fundamentals of Plasma Physics*. Fundamentals of Plasma Physics, Third Edition by J.A. Bittencourt. Published by Springer-Verlag, New York, Inc.; 2004. ISBN 0-387-20975-1., third edition.

Breech, B., Matthaeus, W. H., Cranmer, S. R., Kasper, J. C., and Oughton, S. (2009). Electron and proton heating by solar wind turbulence. *Journal of Geophysical Research: Space Physics*, 114(A9).

Bruno, R. and Carbone, V. (2013). The Solar Wind as a Turbulence Laboratory. *Living Reviews in Solar Physics*, 10(1):2.

Carlson, C., Curtis, D., Paschmann, G., and Michel, W. (1982). An instrument for rapidly measuring plasma distribution functions with high resolution. *Advances in Space Research*, 2(7):67–70.

Chamberlain, J. W. (1960). Interplanetary Gas.II. Expansion of a Model Solar Corona. *Astrophys. J.*, 131:47.

Chandrasekhar, S. (1967). *An introduction to the study of stellar structure*. Dover Publications.

Chapman, S. and Ferraro, V. C. A. (1940). The theory of the first phase of a geomagnetic storm. *Terrestrial Magnetism and Atmospheric Electricity (Journal of Geophysical Research)*, 45(3):245.

Chen, C. H. K., Bale, S. D., Bonnell, J. W., Borovikov, D., Bowen, T. A., Burgess, D., Case, A. W., Chandran, B. D. G., de Wit, T. D., Goetz, K., Harvey, P. R., Kasper, J. C., Klein, K. G., Korreck, K. E., Larson, D., Livi, R., MacDowall, R. J., Malaspina, D. M., Mallet, A., McManus, M. D., Moncuquet, M., Pulupa, M., Stevens, M. L., and Whittlesey, P. (2020). The evolution and role of solar wind turbulence in the inner heliosphere. *The Astrophysical Journal Supplement Series*, 246(2):53.

Coleman, Paul J., J. (1968). Turbulence, Viscosity, and Dissipation in the Solar-Wind Plasma. *Astrophys. J.*, 153:371.

Cowie, L. L. and McKee, C. F. (1977). The evaporation of spherical clouds in a hot gas. I. Classical and saturated mass loss rates. *Astrophys. J.*, 211:135–146.

Cranmer, S. R., Matthaeus, W. H., Breech, B. A., and Kasper, J. C. (2009). EMPIRICAL CONSTRAINTS ON PROTON AND ELECTRON HEATING IN THE FAST SOLAR WIND. *The Astrophysical Journal*, 702(2):1604–1614.

Dum, C., Marsch, E., and Pilipp, W. (1980). Determination of wave growth from measured distribution functions and transport theory. *Journal of Plasma Physics*, 23(1):91–113.

Feldman, W., Asbridge, J., Bame, S., Montgomery, M., and Gary, S. (1975). Solar wind electrons. *Journal of Geophysical Research*, 80.

Feldman, W. C., Asbridge, J. R., Bame, S. J., Gary, S. P., and Montgomery, M. D. (1976). Electron parameter correlations in high-speed streams and heat flux instabilities. *Journal of Geophysical Research (1896-1977)*, 81(13):2377–2382.

Feldman, W. C., Asbridge, J. R., Bame, S. J., and Gosling, J. T. (1979). Long-term

solar wind electron variations between 1971 and 1978. *Journal of Geophysical Research: Space Physics*, 84(A12):7371–7377.

Fitzenreiter, R. J., Ogilvie, K. W., Chornay, D. J., and Keller, J. (1998). Observations of electron velocity distribution functions in the solar wind by the WIND Spacecraft: High angular resolution Strahl measurements. *Geophys. Res. Lett.*, 25(3):249–252.

Fox, N. J., Velli, M. C., Bale, S. D., Decker, R., Driesman, A., Howard, R. A., Kasper, J. C., Kinnison, J., Kusterer, M., Lario, D., Lockwood, M. K., McComas, D. J., Raouafi, N. E., and Szabo, A. (2016). The Solar Probe Plus Mission: Humanity's First Visit to Our Star. *Space Sci. Rev.*, 204(1-4):7–48.

Franci, L., Papini, E., Micera, A., Lapenta, G., Hellinger, P., Del Sarto, D., Burgess, D., and Landi, S. (2022). Anisotropic electron heating in turbulence-driven magnetic reconnection in the near-Sun solar wind. *arXiv e-prints*, page arXiv:2205.08670.

Gary, S. P., Feldman, W. C., Forslund, D. W., and Montgomery, M. D. (1975). Heat flux instabilities in the solar wind. *J. Geophys. Res.*, 80(31):4197.

Goldstein, M. L., Wicks, R. T., Perri, S., and Sahraoui, F. (2015). Kinetic scale turbulence and dissipation in the solar wind: key observational results and future outlook. *Philosophical Transactions of the Royal Society A: Mathematical, Physical and Engineering Sciences*, 373(2041):20140147.

Gosling, J. T., Baker, D. N., Bame, S. J., Feldman, W. C., Zwickl, R. D., and Smith, E. J. (1987). Bidirectional solar wind electron heat flux events. *Journal of Geophysical Research: Space Physics*, 92(A8):8519–8535.

Graham, G. A., Rae, I. J., Owen, C. J., Walsh, A. P., Arridge, C. S., Gilbert, L., Lewis, G. R., Jones, G. H., Forsyth, C., Coates, A. J., and Waite, J. H. (2017). The evolution of solar wind strahl with heliospheric distance. *Journal of Geophysical Research: Space Physics*, 122(4):3858–3874.

Gringauz, K. and Rytov, S. (1961). *Relationship Between the Results of Measurements by Charged-Particle Traps on the Soviet Cosmic Rockets and Magnetic Field Measurements on the American Satellite" Explore VI" and Rocket" Pioneer V"*, volume 5.

Halekas, J. S., Berčič, L., Whittlesey, P., Larson, D. E., Livi, R., Berthomier, M., Kasper, J. C., Case, A. W., Stevens, M. L., Bale, S. D., MacDowall, R. J., and Pulupa, M. P. (2021). The Sunward Electron Deficit: A Telltale Sign of the Sun's Electric Potential. *Astrophys. J.*, 916(1):16.

Halekas, J. S., Taylor, E. R., Dalton, G., Johnson, G., Curtis, D. W., McFadden, J. P., Mitchell, D. L., Lin, R. P., and Jakosky, B. M. (2015). The Solar Wind Ion Analyzer for MAVEN. *Space Sci. Rev.*, 195(1-4):125–151.

Halekas, J. S., Whittlesey, P., Larson, D. E., McGinnis, D., Maksimovic, M., Berthomier, M., Kasper, J. C., Case, A. W., Korreck, K. E., Stevens, M. L., Klein, K. G., Bale, S. D., MacDowall, R. J., Pulupa, M. P., Malaspina, D. M., Goetz, K., and Harvey, P. R. (2020). Electrons in the young solar wind: First results from the parker solar probe. *The Astrophysical Journal Supplement Series*, 246(2):22.

Halekas, J. S., Whittlesey, P. L., Larson, D. E., McGinnis, D., Bale, S. D., Berthomier, M., Case, A. W., Chandran, B. D. G., Kasper, J. C., Klein, K. G., Korreck, K. E., Livi, R., MacDowall, R. J., Maksimovic, M., Malaspina, D. M., Matteini, L., Pulupa, M. P., and Stevens, M. L. (2021). Electron heat flux in the near-sun environment. *A&A*, 650:A15.

Hammond, C. M., Feldman, W. C., McComas, D. J., Phillips, J. L., and Forsyth, R. J. (1996). Variation of electron-strahl width in the high-speed solar wind: ULYSSES observations. *Astron. Astrophys.*, 316:350–354.

Hefti, S., Zurbuchen, T. H., Fisk, L. A., Gloeckler, G., Larson, D., and Lin, R. P. (1999). The transition from slow to fast solar wind: Charge state composition and electron observations. In Habbal, S. R., Esser, R., Hollweg, J. V., and Isenberg,

P. A., editors, *Solar Wind Nine*, volume 471 of *American Institute of Physics Conference Series*, pages 495–497.

Horaites, K., Boldyrev, S., Wilson, Lynn B., I., Viñas, A. F., and Merka, J. (2017). Kinetic theory and fast wind observations of the electron strahl. *Monthly Notices of the Royal Astronomical Society*, 474(1):115–127.

Jeong, S.-Y., Abraham, J., Verscharen, D., Bercic, L., Stansby, D., Nicolaou, G., Owen, C., Wicks, R., Fazakerley, A., Agudelo, J., and Bakrania, M. (2022a). The stability of the electron strahl against the oblique fast-magnetosonic/whistler instability in the inner heliosphere. *Astrophysical Journal Letters*, 926.

Jeong, S.-Y., Verscharen, D., Vocks, C., Abraham, J. B., Owen, C. J., Wicks, R. T., Fazakerley, A. N., Stansby, D., Berčič, L., Nicolaou, G., Rueda, J. A. A., and Bakrania, M. (2022b). The kinetic expansion of solar-wind electrons: Transport theory and predictions for the very inner heliosphere. *The Astrophysical Journal*, 927(2):162.

Jeong, S.-Y., Verscharen, D., Wicks, R. T., and Fazakerley, A. N. (2020). A quasi-linear diffusion model for resonant wave–particle instability in homogeneous plasma. *The Astrophysical Journal*, 902(2):128.

Jockers, K. (1970). Solar wind models based on exospheric theory. *Astron. Astrophys.*, 6:219.

Johnstone, A. D., Coates, A. J., Hall, D. S., Maehlum, B. N., Schwartz, S. J., Thomsen, M., and Winningham, J. D. (1988). PEACE: A Plasma Electron And Current Experiment. In ESA, The Cluster Mission: Scientific and Technical Aspects of the Instruments p 77-84 (SEE N89-20156 13-12).

Kallenrode, M.-B. (2001). *Space Physics*.

Kasper, J. C., Abiad, R., Austin, G., Balat-Pichelin, M., Bale, S. D., Belcher, J. W., Berg, P., Bergner, H., Berthomier, M., Bookbinder, J., Brodu, E., Caldwell, D., Case, A. W., Chandran, B. D. G., Cheimets, P., Cirtain, J. W., Cranmer, S. R.,

Curtis, D. W., Daigneau, P., Dalton, G., Dasgupta, B., DeTomaso, D., Diaz-Aguado, M., Djordjevic, B., Donaskowski, B., Effinger, M., Florinski, V., Fox, N., Freeman, M., Gallagher, D., Gary, S. P., Gauron, T., Gates, R., Goldstein, M., Golub, L., Gordon, D. A., Gurnee, R., Guth, G., Halekas, J., Hatch, K., Heerikuisen, J., Ho, G., Hu, Q., Johnson, G., Jordan, S. P., Korreck, K. E., Larson, D., Lazarus, A. J., Li, G., Livi, R., Ludlam, M., Maksimovic, M., McFadden, J. P., Marchant, W., Maruca, B. A., McComas, D. J., Messina, L., Mercer, T., Park, S., Peddie, A. M., Pogorelov, N., Reinhart, M. J., Richardson, J. D., Robinson, M., Rosen, I., Skoug, R. M., Slagle, A., Steinberg, J. T., Stevens, M. L., Szabo, A., Taylor, E. R., Tiu, C., Turin, P., Velli, M., Webb, G., Whittlesey, P., Wright, K., Wu, S. T., and Zank, G. (2016). Solar Wind Electrons Alphas and Protons (SWEAP) Investigation: Design of the Solar Wind and Coronal Plasma Instrument Suite for Solar Probe Plus. *Space Sci. Rev.*, 204(1-4):131–186.

Kivelson, M. G. and Russell, C. T. (1995). *Introduction to Space Physics*.

Kohlhase, C. E. and Penzo, P. A. (1977). Voyager Mission Description. *Space Sci. Rev.*, 21(2):77–101.

Kuhn, S., Kamran, M., Jelić, N., Kos, L., Tskhakaya, D., and Tskhakaya, D. D. (2010). Closure of the hierarchy of fluid equations by means of the polytropic-coefficient function (PCF). In Eliasson, B. and Shukla, P. K., editors, *New Frontiers in Advanced Plasma Physics*, volume 1306 of *American Institute of Physics Conference Series*, pages 216–231.

Lamy, H., Maksimovic, M., Pierrard, V., and Lemaire, J. (2003). Solar wind kinetic exospheric models with typical coronal holes exobase conditions. In Velli, M., Bruno, R., Malara, F., and Bucci, B., editors, *Solar Wind Ten*, volume 679 of *American Institute of Physics Conference Series*, pages 367–370.

Landi, S., Matteini, L., and Pantellini, F. (2012). On the Competition Between Radial Expansion and Coulomb Collisions in Shaping the Electron Velocity Distribution Function: Kinetic Simulations. *Astrophys. J.*, 760(2):143.

Landi, S., Matteini, L., and Pantellini, F. (2014). ELECTRON HEAT FLUX IN THE SOLAR WIND: ARE WE OBSERVING THE COLLISIONAL LIMIT IN THE 1 AU DATA? *The Astrophysical Journal*, 790(1):L12.

Lemaire, J. and Scherer, M. (1971). Kinetic models of the solar wind. *J. Geophys. Res.*, 76(31):7479.

Levenberg, K. (1944). A method for the solution of certain non-linear problems in least squares. *Quarterly of Applied Mathematics*, 2(2):164–168.

Lie-Svendsen, Ø., Hansteen, V. H., and Leer, E. (1997). Kinetic electrons in high-speed solar wind streams: Formation of high-energy tails. *J. Geophys. Res.*, 102(A3):4701–4718.

Lin, R. P., Anderson, K. A., Ashford, S., Carlson, C., Curtis, D., Ergun, R., Larson, D., McFadden, J., McCarthy, M., Parks, G. K., Rème, H., Bosqued, J. M., Coutelier, J., Cotin, F., D'Uston, C., Wenzel, K. P., Sanderson, T. R., Henrion, J., Ronnet, J. C., and Paschmann, G. (1995). A Three-Dimensional Plasma and Energetic Particle Investigation for the Wind Spacecraft. *Space Sci. Rev.*, 71(1-4):125–153.

Livadiotis, G. (2019). Turbulent heating in solar wind thermodynamics. *The Astrophysical Journal*, 887(2):117.

Livadiotis, G. and McComas, D. J. (2013). Understanding Kappa Distributions: A Toolbox for Space Science and Astrophysics. *Space Sci. Rev.*, 175(1-4):183–214.

López, R. A., Lazar, M., Shaaban, S. M., Poedts, S., and Moya, P. S. (2020). Alternative high-plasma beta regimes of electron heat-flux instabilities in the solar wind. *The Astrophysical Journal*, 900(2):L25.

Maksimovic, M., Gary, S. P., and Skoug, R. M. (2000). Solar wind electron suprathermal strength and temperature gradients: Ulysses observations. *Journal of Geophysical Research: Space Physics*, 105(A8):18337–18350.

Maksimovic, M., Pierrard, V., and Lemaire, J. (2001). On the Exospheric Approach for the Solar Wind Acceleration. *Astron. Astrophys. Suppl. Series*, 277:181–187.

Maksimovic, M., Pierrard, V., and Lemaire, J. F. (1997). A kinetic model of the solar wind with Kappa distribution functions in the corona. *Astron. Astrophys.*, 324:725–734.

Maksimovic, M., Zouganelis, I., Chaufray, J.-Y., Issautier, K., Scime, E., Littleton, J., Marsch, E., Mccomas, D., Salem, C., Lin, R., and Elliott, H. (2005). Radial evolution of the electron distribution functions in the fast solar wind between 0.3 and 1.5 au. *Journal of Geophysical Research, v.110 (2005)*, 110.

Malara, F., Nigro, G., Valentini, F., and Sorriso-Valvo, L. (2019). Electron heating by kinetic alfvén waves in coronal loop turbulence. *The Astrophysical Journal*, 871(1):66.

Malaspina, D. M., Ergun, R. E., Bolton, M., Kien, M., Summers, D., Stevens, K., Yehle, A., Karlsson, M., Hoxie, V. C., Bale, S. D., and Goetz, K. (2016). The digital fields board for the fields instrument suite on the solar probe plus mission: Analog and digital signal processing. *Journal of Geophysical Research: Space Physics*, 121(6):5088–5096.

Marsch, E. (2006). Kinetic Physics of the Solar Corona and Solar Wind. *Living Reviews in Solar Physics*, 3(1):1.

McComas, D. J., Christian, E. R., Schwadron, N. A., Fox, N., Westlake, J., Allegrini, F., Baker, D. N., Biesecker, D., Bzowski, M., Clark, G., Cohen, C. M. S., Cohen, I., Dayeh, M. A., Decker, R., de Nolfo, G. A., Desai, M. I., Ebert, R. W., Elliott, H. A., Fahr, H., Frisch, P. C., Funsten, H. O., Fuselier, S. A., Galli, A., Galvin, A. B., Giacalone, J., Gkioulidou, M., Guo, F., Horanyi, M., Isenberg, P., Janzen, P., Kistler, L. M., Korreck, K., Kubiak, M. A., Kucharek, H., Larsen, B. A., Leske, R. A., Lugaz, N., Luhmann, J., Matthaeus, W., Mitchell, D., Moebius, E., Ogasawara, K., Reisenfeld, D. B., Richardson, J. D., Russell, C. T., Sokół, J. M., Spence, H. E., Skoug, R., Sternovsky, Z., Swaczyna, P., Szalay,

J. R., Tokumaru, M., Wiedenbeck, M. E., Wurz, P., Zank, G. P., and Zirnstein, E. J. (2018). Interstellar Mapping and Acceleration Probe (IMAP): A New NASA Mission. *Space Sci. Rev.*, 214(8):116.

McComas, D. J., Elliott, H. A., Schwadron, N. A., Gosling, J. T., Skoug, R. M., and Goldstein, B. E. (2003). The three-dimensional solar wind around solar maximum. *Geophysical Research Letters*, 30(10).

Moncuquet, M., Meyer-Vernet, N., Issautier, K., Pulupa, M., Bonnell, J., Bale, S., Dudok de Wit, T., Goetz, K., Griton, L., Harvey, P., MacDowall, R., Maksimovic, M., and Malaspina, D. (2020). First in situ measurements of electron density and temperature from quasi-thermal noise spectroscopy with parker solar probe /fields. *The Astrophysical Journal Supplement Series*, 246:44.

Müller, D., St. Cyr, O. C., Zouganelis, I., Gilbert, H. R., Marsden, R., Nieves-Chinchilla, T., Antonucci, E., Auchère, F., Berghmans, D., Horbury, T. S., Howard, R. A., Krucker, S., Maksimovic, M., Owen, C. J., Rochus, P., Rodriguez-Pacheco, J., Romoli, M., Solanki, S. K., Bruno, R., Carlsson, M., Fludra, A., Harra, L., Hassler, D. M., Livi, S., Louarn, P., Peter, H., Schühle, U., Teriaca, L., del Toro Iniesta, J. C., Wimmer-Schweingruber, R. F., Marsch, E., Velli, M., De Groof, A., Walsh, A., and Williams, D. (2020). The Solar Orbiter mission. Science overview. *Astron. Astrophys.*, 642:A1.

Ness, N. F. (1970). Magnetometers for Space Research. *Space Sci. Rev.*, 11(4):459–554.

Neugebauer, M. and Snyder, C. W. (1966). Mariner 2 observations of the solar wind: 1. average properties. *Journal of Geophysical Research (1896-1977)*, 71(19):4469–4484.

Nicolaou, G., Wicks, R., Livadiotis, G., Verscharen, D., Owen, C., and Kataria, D. (2020). Determining the bulk parameters of plasma electrons from pitch-angle distribution measurements. *Entropy*, 22(1).

Nicolaou, G., Wicks, R. T., Owen, C. J., Kataria, D. O., Chandrasekhar, A., Lewis, G. R., Verscharen, D., Fortunato, V., Mele, G., DeMarco, R., and Bruno, R. (2021). Deriving the bulk properties of solar wind electrons observed by Solar Orbiter. A preliminary study of electron plasma thermodynamics. *Astron. Astrophys.*, 656:A10.

Ogilvie, K. W. and Scudder, J. D. (1978). The radial gradients and collisional properties of solar wind electrons. *Journal of Geophysical Research: Space Physics*, 83(A8):3776–3782.

Owen, C. J., Abraham, J. B., Nicolaou, G., Verscharen, D., Louarn, P., and Horbury, T. S. (2022). Solar orbiter swa observations of electron strahl properties inside 1 au. *Universe*, 8(10).

Owen, C. J., Bruno, R., Livi, S., Louarn, P., Al Janabi, K., Allegrini, F., Amoros, C., Baruah, R., Barthe, A., Berthomier, M., Bordon, S., Brockley-Blatt, C., Brysbaert, C., Capuano, G., Collier, M., DeMarco, R., Fedorov, A., Ford, J., Fortunato, V., Fratter, I., Galvin, A. B., Hancock, B., Heirtzler, D., Kataria, D., Kistler, L., Lepri, S. T., Lewis, G., Loeffler, C., Marty, W., Mathon, R., Mayall, A., Mele, G., Ogasawara, K., Orlandi, M., Pacros, A., Penou, E., Persyn, S., Petiot, M., Phillips, M., Přech, L., Raines, J. M., Reden, M., Rouillard, A. P., Rousseau, A., Rubiella, J., Seran, H., Spencer, A., Thomas, J. W., Trevino, J., Verscharen, D., Wurz, P., Alapide, A., Amoruso, L., André, N., Anekallu, C., Arciuli, V., Arnett, K. L., Ascolese, R., Bancroft, C., Bland, P., Brysch, M., Calvanese, R., Castronuovo, M., Čermák, I., Chornay, D., Clemens, S., Coker, J., Collinson, G., D'Amicis, R., Dandouras, I., Darnley, R., Davies, D., Davison, G., De Los Santos, A., Devoto, P., Dirks, G., Edlund, E., Fazakerley, A., Ferris, M., Frost, C., Fruit, G., Garat, C., Génot, V., Gibson, W., Gilbert, J. A., de Giosa, V., Gradone, S., Hailey, M., Horbury, T. S., Hunt, T., Jacquey, C., Johnson, M., Lavraud, B., Lawrenson, A., Leblanc, F., Lockhart, W., Maksimovic, M., Malpus, A., Marcucci, F., Mazelle, C., Monti, F., Myers, S., Nguyen, T., Rodriguez-Pacheco, J., Phillips, I., Popecki, M., Rees, K., Rogacki, S. A., Ruane, K., Rust, D., Salatti,

M., Sauvaud, J. A., Stakhiv, M. O., Stange, J., Stubbs, T., Taylor, T., Techer, J. D., Terrier, G., Thibodeaux, R., Urdiales, C., Varsani, A., Walsh, A. P., Watson, G., Wheeler, P., Willis, G., Wimmer-Schweingruber, R. F., Winter, B., Yardley, J., and Zouganelis, I. (2020). The Solar Orbiter Solar Wind Analyser (SWA) suite. *Astron. Astrophys.*, 642:A16.

Owens, M. J., Crooker, N. U., and Schwadron, N. A. (2008). Suprathermal electron evolution in a parker spiral magnetic field. *Journal of Geophysical Research: Space Physics*, 113(A11).

Pagel, C., Gary, S. P., de Koning, C. A., Skoug, R. M., and Steinberg, J. T. (2007). Scattering of suprathermal electrons in the solar wind: ACE observations. *Journal of Geophysical Research (Space Physics)*, 112(A4):A04103.

Parker, E. (2010). Kinetic and hydrodynamic representations of coronal expansion and the solar wind. *Twelfth International Solar Wind Conference*, 1216.

Parker, E. N. (1958). Dynamics of the Interplanetary Gas and Magnetic Fields. *Astrophys. J.*, 128:664.

Parker, E. N. (1963). *Interplanetary dynamical processes.*

Pedregosa, F., Varoquaux, G., Gramfort, A., Michel, V., Thirion, B., Grisel, O., Blondel, M., Prettenhofer, P., Weiss, R., Dubourg, V., Vanderplas, J., Passos, A., Cournapeau, D., Brucher, M., Perrot, M., and Duchesnay, E. . (2011). Scikit-learn: Machine learning in Python. *Journal of Machine Learning Research*, 12:2825–2830.

Pierrard, V., Lazar, M., and Štverák, S. (2020). Solar Wind Plasma Particles Organized by the Flow Speed. *Sol. Phys.*, 295(11):151.

Pilipp, W. G., Miggenrieder, H., Mühläuser, K.-H., Rosenbauer, H., and Schwenn, R. (1990). Large-scale variations of thermal electron parameters in the solar wind between 0.3 and 1 au. *Journal of Geophysical Research: Space Physics*, 95(A5):6305–6329.

Rosenbauer, H., Schwenn, R., Marsch, E., Meyer, B., Miggenrieder, H., Montgomery, M. D., Muehlhaeuser, K. H., Pilipp, W., Voges, W., and Zink, S. M. (1977). A survey on initial results of the HELIOS plasma experiment. *Journal of Geophysics Zeitschrift Geophysik*, 42(6):561–580.

Saito, S. and Gary, S. P. (2007). Whistler scattering of suprathermal electrons in the solar wind: Particle-in-cell simulations. *Journal of Geophysical Research: Space Physics*, 112(A6).

Salem, C., Hubert, D., Lacombe, C., Bale, S., Mangeney, A., Larson, D., and Lin, R. (2003). Electron properties and coulomb collisions in the solar wind at 1 au: Wind observations. *The Astrophysical Journal*, 585(2):1147.

Schekochihin, A. A., Cowley, S. C., Dorland, W., Hammett, G. W., Howes, G. G., Quataert, E., and Tatsuno, T. (2009). ASTROPHYSICAL GYROKINETICS: KINETIC AND FLUID TURBULENT CASCADES IN MAGNETIZED WEAKLY COLLISIONAL PLASMAS. *The Astrophysical Journal Supplement Series*, 182(1):310–377.

Schwartz, S. J. (1980). Plasma instabilities in the solar wind: A theoretical review. *Reviews of Geophysics*, 18(1):313–336.

Scime, E. E., Bame, S. J., Feldman, W. C., Gary, S. P., Phillips, J. L., and Balogh, A. (1994). Regulation of the solar wind electron heat flux from 1 to 5 AU: Ulysses observations. *J. Geophys. Res.*, 99(A12):23401–23410.

Scudder, J. D. (1992). On the Causes of Temperature Change in Inhomogeneous Low-Density Astrophysical Plasmas. *Astrophys. J.*, 398:299.

Scudder, J. D. and Olbert, S. (1979). A theory of local and global processes which affect solar wind electrons 2. Experimental support. *J. Geophys. Res.*, 84(A11):6603–6620.

Shoda, M., Chandran, B. D. G., and Cranmer, S. R. (2021). Turbulent generation

of magnetic switchbacks in the alfvénic solar wind. *The Astrophysical Journal*, 915(1):52.

Sittler, E. C., J. and Scudder, J. D. (1980). An empirical polytrope law for solar wind thermal electrons between 0.45 and 4.76 AU: Voyager 2 and Mariner 10. *J. Geophys. Res.*, 85(A10):5131–5137.

Smith, H. M., Marsch, E., and Helander, P. (2012). Electron Transport in the Fast Solar Wind. *Astrophys. J.*, 753(1):31.

Stansby, D., Salem, C., Matteini, L., and Horbury, T. (2018). A New Inner Heliosphere Proton Parameter Dataset from the Helios Mission. *Solar Physics*, 293(11):155.

Stix, T. H. (1992). *Waves in plasmas*.

Štverák, Š., Trávníček, P., Maksimovic, M., Marsch, E., Fazakerley, A. N., and Scime, E. E. (2008). Electron temperature anisotropy constraints in the solar wind. *Journal of Geophysical Research: Space Physics*, 113(A3).

Sundkvist, D., Retinò, A., Vaivads, A., and Bale, S. D. (2007). Dissipation in Turbulent Plasma due to Reconnection in Thin Current Sheets. *Phys. Rev. Lett.*, 99(2):025004.

Totten, T. L., Freeman, J. W., and Arya, S. (1995). An empirical determination of the polytropic index for the free-streaming solar wind using helios 1 data. *Journal of Geophysical Research: Space Physics*, 100(A1):13–17.

Tu, C.-Y. and Marsch, E. (1995). Mhd structures, waves and turbulence in the solar wind: Observations and theories. *Space Science Reviews*, 73:1–210.

Verscharen, D., Chandran, B. D. G., Boella, E., Halekas, J., Innocenti, M. E., Jagarlamudi, V. K., Micera, A., Pierrard, V., Štverák, Š., Vasko, I. Y., Velli, M., and Whittlesey, P. L. (2022). Electron-Driven Instabilities in the Solar Wind. *Frontiers in Astronomy and Space Sciences*, 9:951628.

Verscharen, D., Chandran, B. D. G., Jeong, S.-Y., Salem, C. S., Pulupa, M. P., and Bale, S. D. (2019). Self-induced scattering of strahl electrons in the solar wind. *The Astrophysical Journal*, 886(2):136.

Verscharen, D., Klein, K. G., and Maruca, B. A. (2019). The multi-scale nature of the solar wind. *Living Reviews in Solar Physics*, 16(1):5.

Viall, N. M. and Borovsky, J. E. (2020). Nine Outstanding Questions of Solar Wind Physics. *Journal of Geophysical Research (Space Physics)*, 125(7):e26005.

Vocks, C. and Mann, G. (2003). Generation of Suprathermal Electrons by Resonant Wave-Particle Interaction in the Solar Corona and Wind. *Astrophys. J.*, 593(2):1134–1145.

Vocks, C., Salem, C., Lin, R. P., and Mann, G. (2005). Electron Halo and Strahl Formation in the Solar Wind by Resonant Interaction with Whistler Waves. *Astrophys. J.*, 627(1):540–549.

Štverák, v., Trávníček, P. M., and Hellinger, P. (2015). Electron energetics in the expanding solar wind via helios observations. *Journal of Geophysical Research: Space Physics*, 120(10):8177–8193.

Wenzel, K. P., Marsden, R. G., Page, D. E., and Smith, E. J. (1992). The ULYSSES Mission. *Astrophys. Space. Sci*, 92:207.

Whittlesey, P. L., Larson, D. E., Kasper, J. C., Halekas, J., Abatcha, M., Abiad, R., Berthomier, M., Case, A. W., Chen, J., Curtis, D. W., Dalton, G., Klein, K. G., Korreck, K. E., Livi, R., Ludlam, M., Marckwordt, M., Rahmati, A., Robinson, M., Slagle, A., Stevens, M. L., Tiu, C., and Verniero, J. L. (2020). The solar probe ANalyzers—electrons on the parker solar probe. *The Astrophysical Journal Supplement Series*, 246(2):74.

Woodham, L. D., Horbury, T. S., Matteini, L., Woolley, T., Laker, R., Bale, S. D., Nicolaou, G., Stawarz, J. E., Stansby, D., Hietala, H., Larson, D. E., Livi, R.,

Verniero, J. L., McManus, M., Kasper, J. C., Korreck, K. E., Raouafi, N., Moncuquet, M., and Pulupa, M. P. (2020). Enhanced proton parallel temperature inside patches of switchbacks in the inner heliosphere. *Astronomy & Astrophysics*.

Yang, Y., Matthaeus, W. H., Roy, S., Roytershteyn, V., Parashar, T. N., Bandyopadhyay, R., and Wan, M. (2022). Pressure–strain interaction as the energy dissipation estimate in collisionless plasma. *The Astrophysical Journal*, 929(2):142.

Zhou, M., Liu, Z., and Loureiro, N. F. (2022). Intermittency and electron heating in kinetic-alfvén-wave turbulence.

Zouganelis, I., Maksimovic, M., Meyer-Vernet, N., Lamy, H., and Issautier, K. (2004). A Transonic Collisionless Model of the Solar Wind. *Astrophys. J.*, 606(1):542–554.

Štverák, Š., Maksimovic, M., Trávníček, P. M., Marsch, E., Fazakerley, A. N., and Scime, E. E. (2009). Radial evolution of nonthermal electron populations in the low-latitude solar wind: Helios, cluster, and ulysses observations. *Journal of Geophysical Research: Space Physics*, 114(A5).